

Electronic Thesis and Dissertation Repository

---

12-4-2020 10:00 AM

## Improving Hybrid PET/MRI Cardiovascular Imaging with Improved Hardware Design and Attenuation Correction Coefficient

Adam Helmy Farag, *The University of Western Ontario*

Supervisor: Jean Théberge, *The University of Western Ontario*

Co-Supervisor: R Terry Thompson, *The University of Western Ontario*

A thesis submitted in partial fulfillment of the requirements for the Doctor of Philosophy degree in Medical Biophysics

© Adam Helmy Farag 2020

Follow this and additional works at: <https://ir.lib.uwo.ca/etd>



Part of the [Engineering Physics Commons](#), and the [Medical Biophysics Commons](#)

---

### Recommended Citation

Farag, Adam Helmy, "Improving Hybrid PET/MRI Cardiovascular Imaging with Improved Hardware Design and Attenuation Correction Coefficient" (2020). *Electronic Thesis and Dissertation Repository*. 7503. <https://ir.lib.uwo.ca/etd/7503>

This Dissertation/Thesis is brought to you for free and open access by Scholarship@Western. It has been accepted for inclusion in Electronic Thesis and Dissertation Repository by an authorized administrator of Scholarship@Western. For more information, please contact [wlsadmin@uwo.ca](mailto:wlsadmin@uwo.ca).

## Abstract

According to the World Health Organization (WHO) report in 2019, cardiovascular diseases (CVD) cause 52% of all illness-related deaths globally and are considered to be the second most common cause of death in Canada. CVD is also estimated to cost the Canadian economy about \$21.2 billion in direct and indirect costs. With these figures, it is vital to develop the most effective and accurate methods and tools to diagnose accurately CVD and their causes. One of the promising tools for accurate diagnostic and therapeutic of CVD is the integrated Positron Emission Tomography (PET) and Magnetic Resonance Imaging (MRI) PET/MRI technology, which has successfully been used in cardiovascular imaging. The PET/MRI system provides low exposure of radioactive and ionized radiation which is advantageous over the standard technology of integrated PET/computed tomography (CT) PET/CT system. However, since the integrated PET/MRI technology was first introduced in 2010 for clinical use, its hardware attenuation correction (AC) still presents a challenge, which is crucial to achieving accurate PET quantification in cardiac imaging. Additionally, for cardiovascular PET/MRI the system still requires a higher temporal and spatial resolution radio frequency (RF) phased array for faster imaging sessions of cardiac patient, without loss of MRI image quality, while minimizing photon attenuation.

This thesis introduces a novel 32-channel RF phased array, prospectively-designed for simultaneous PET/MRI cardiovascular imaging. The phased array's MR imaging quality parameters, including, geometry factor (g-factor), noise correlation coefficient (NCC) and signal-to-noise ratio (SNR) were measured using a phantom and three healthy volunteers and the results were compared against currently used arrays.

Post-assessing the MR image quality, the array was evaluated for 511keV PET photon attenuation. The evaluation is carried out using a NEMA procedure and phantom, in which contrast recovery (CR), background variation (BV) and contrast-to-noise ratio (CNR) were measured and compared. Furthermore, the thesis presents a static radioactive source as a novel method for accurate attenuation correction (AC) of hardware (i.e. patient table) used during cardiovascular imaging.

In summary, assessing both MRI and PET performances of the novel array, resulted in MRI SNR improvements of >30% at different acceleration factors ( $R > 2$ ), compared to the standard array. In the meantime, the PET counts loss caused by the novel array was significantly lower ( $p=0.001$ ) than those caused by the standard arrays. The novel AC method produced a hardware AC map with global counts loss of -0.7% in comparison to -4.3% as produced by the CT-based method.

In conclusion, both the novel array and the hardware AC method presented here, enable the acquisition of high temporal (fast imaging session) and spatial (image quality) resolutions by the MRI system, together with accurately quantifying the PET standardized-uptake-value (SUV). The method and tools presented in this work have been evaluated for simultaneous PET/MRI cardiovascular imaging, and hence they can be effectively used to study CVD and their causes accurately in a shorter imaging time. Therefore, the improvements reported in this thesis contribute to better understand the CVD and potentially lowering the economic burden around them. The impact of these improvements is broad, since they may be applied to PET/MRI imaging of brain, prostate and other organs.

## Keywords

Cardiovascular imaging, PET/MRI system, attenuation correction coefficient,  
Radiofrequency phased arrays, acceleration factor, geometry-factor.

## Summary for Lay Audience

Treatment of diseases is only possible if their causes and developments are understood. In medical imaging, understanding the disease is the purpose behind developing methodologies and tools that can be used during this process. Two of the imaging tools used in understanding cardiac diseases are the positron emission tomography (PET) and magnetic resonance imaging (MRI). Both have been integrated into one scanner namely PET/MRI to complement each other, which provides excellent data to study heart functions, disease causes and disease development. In hybrid PET/MRI technology, the MRI is free of radiation and provides excellent image contrast, while the PET system is used for measuring tissue functions, both of which are necessary for diagnosis.

The PET/MRI technology is fairly new (only 10 years old), and is powerful, because it reduces the study time by half especially for patients requiring imaging with both PET and MRI. However, due to the integration of the PET and MRI into one, hybrid PET/MRI, several challenges become apparent which need to be addressed. One of these challenges is the inaccurate counts of radioactivity in the PET image. This happens when the radioactivity is blocked by hardware parts which are present in the scanner during imaging. Another challenge is to obtain high-resolution MRI images and reduce the scanning time, so a tool (named a RF phased array) is required to achieve these high-resolution images and shorten the time of the imaging session for the patient. This research work addresses both the accurate counting of the radioactivity and the RF phased array. My research work provided an RF array that does not block radioactivity, while also being capable of shortening the imaging time to a tolerable level for the cardiac patient. The research work also provided a new approach to correct for inaccurate counts caused by other parts in the

PET/MRI system. The author anticipates that these improvements and developments will enhance accurate diagnosis and the study of cardiac diseases using the PET/MRI platform.

## Co-Authorship Statement

This thesis includes two manuscripts conforming in chapters 2 and 3, which both have been published in European Journal of Hybrid Imaging (EJHI). It also includes, in chapter 4, a manuscript which has been submitted to a scientific journal and is currently under review. For each manuscript the author and coauthors have contributed to the work in different capacity and are listed below.

The content of chapter 2 incorporates the manuscript published in European Journal of Hybrid Imaging. 2019;3(1):13, August 2019 in Springers Open access, and permission to reuse its content for this thesis is not required. Experiments design and planning of the workflow were carried out by Adam Farag. Both conducting the experiments and acquiring the images on phantom were performed by Adam Farag, while John Butler prepared volunteers for MRI scans and acquired the images. All data processing and analysis, as well as writing the manuscript was completed by Adam Farag. Both data examination and editing of the manuscript were conducted by R.Terry Thompson, Jonathan D. Thiessen, Frank S. Prato and Jean Théberge.

Chapter 3, comprises the manuscript published in European Journal of Hybrid Imaging. 2020;4(1):7. June 2020, Springers Open access, where a permission to reuse the manuscript content for this thesis is not required. Experimental design and workflow planning were carried out by Adam Farag. Conducting the experiments and acquiring images on phantom were performed by Adam Farag. Heather Biernaski contributed to this manuscript by preparing the necessary radioactive tracer. All data processing and analysis, as well as manuscript writing were completed by Adam Farag. Both data examination and editing of

the manuscript were completed by Heather Biernaski, R.Terry Thompson, Jonathan D. Thiessen, Frank S. Prato and Jean Théberge.

Chapter 4 incorporates a manuscript for the research work conducted on attenuation correction, which has been submitted to a scientific journal and is under review. In this manuscript all theoretical development and experimental design, together with workflow were devised by Adam Farag. Volunteer preparation for PET/MRI imaging was performed with the help of Heather Biernaski and John Butler while volunteer recruiting was conducted by Chantelle Graf. All data processing and analysis, as well as writing the manuscript were completed by Adam Farag. Both data examination and editing of the manuscript were conducted by, R.Terry Thompson, Jonathan D. Thiessen, Frank S. Prato and Jean Théberge.



## Acknowledgments

For this successful work of research, I would like to acknowledge Jean Théberge and Terry Thompson, who supervised this doctoral study; thank you for allowing this to happen; your role will always be remembered and cherished.

Sincere thanks to Jonathan Thiessen and Frank S Prato, the advisory committee members, your discussions and attention to details are very much appreciated; thank you for the unforgettable experience.

I would like also to thank both Heather Biernaski and John Butler, for assisting with patients scanning on the PET/MRI scanner. I truly value and thank Jennifer Hadway for spending many of her own time assisting with CT scanning.

To everyone who I may have forgotten to include in this acknowledgement, thank you.

I dedicate this thesis to my daughter and my wife; you are my pillars who have given me the strength to stand against all odds. My words of gratitude to you can never be enough.

# Table of Contents

Abstract.....	i
Summary for Lay Audience.....	iv
Co-Authorship Statement.....	vi
Acknowledgments.....	viii
Table of Contents.....	ix
List of Tables.....	xiii
List of Figures.....	xiv
List of Appendices.....	xvii
List of Abbreviations and Symbols.....	xviii
<b>Chapter 1</b> .....	<b>1</b>
<b>1 Introduction</b> .....	<b>1</b>
1.1 Background.....	1
1.1.1 Motivation.....	1
1.1.2 Thesis outline.....	5
1.2 Principles of selected imaging modalities.....	7
1.2.1 CT imaging modality.....	7
1.2.2 MRI imaging modality.....	11
1.2.3 PET imaging modality.....	23
1.3 Hybrid PET/MRI imaging modalities.....	37
1.3.1 Cardiovascular clinical applications.....	37
1.3.2 Hybrid PET/MRI challenges.....	38
1.4 Thesis objectives.....	40
1.5 References.....	43

<b>Chapter 2</b> .....	62
2 Assessment of a Novel 32-Channel Phased Array for Cardiovascular Hybrid PET/MRI Imaging: MRI performance .....	62
2.1 Introduction.....	62
2.2 Methods and Materials.....	65
2.2.1 Description of the arrays .....	65
2.2.2 MRI Phantom imaging.....	66
2.2.3 In-Vivo Imaging.....	68
2.2.4 Data processing and analysis .....	68
2.2.5 PET activity test.....	71
2.3 Results.....	71
2.3.1 MRI phantom imaging.....	72
2.3.2 MRI in-vivo imaging .....	79
2.3.3 PET imaging .....	83
2.4 Discussion and Conclusion.....	84
2.5 Acknowledgements.....	87
2.6 References.....	88
<b>Chapter 3</b> .....	93
3 Evaluation of 511keV Photon Attenuation from a Novel 32-Channel Phased Array prospectively-designed for Cardiovascular Hybrid PET/MRI Imaging. ....	93
3.1 Introduction.....	93
3.2 Materials and Methods.....	97
3.2.1 The arrays under evaluation and phantom .....	97
3.2.2 AC maps.....	97
3.2.3 PET phantom preparation and measurements set-up.....	98
3.2.4 Image acquisition and attenuation correction .....	100

3.2.5	Data analysis .....	101
3.3	Results.....	103
3.3.1	AC maps.....	103
3.3.2	Global means .....	104
3.3.3	Image quality .....	109
3.3.4	Anterior analysis .....	111
3.3.5	Data analysis .....	112
3.4	Discussion.....	114
3.5	Conclusions.....	116
3.6	Acknowledgement .....	117
3.7	References.....	118
<b>Chapter 4</b>	.....	<b>122</b>
4	Improved PET/MRI accuracy by use of static transmission source in empirically-derived hardware attenuation correction.....	122
4.1	Introduction:.....	122
4.2	Materials and Methods:.....	125
4.2.1	Theory .....	125
4.2.2	Acrylic cylinder and TX-fixture .....	127
4.2.3	TX-based AC .....	128
4.2.4	Theoretical LAC of acrylic .....	130
4.2.5	CT-based AC .....	131
4.2.6	Validation of the technique.....	131
4.2.7	Posterior array.....	131
4.2.8	Patient table.....	132
4.2.9	In Vivo reconstruction .....	132
4.2.10	Data analysis .....	133

4.3 Results and discussion: .....	134
4.3.1 TX-based AC map and validation of LAC .....	134
4.3.2 TX-based AC, and CT-based AC for hardware.....	135
4.3.3 In-Vivo data .....	139
4.4 Discussion: .....	142
4.5 Conclusion: .....	145
4.6 Acknowledgments: .....	145
4.7 Reference .....	146
<b>Chapter 5</b> .....	151
5 Conclusion and future work.....	151
5.1 Summary .....	151
5.2 Conclusions.....	152
5.2.1 Chapter 2.....	152
5.2.2 Chapter 3.....	153
5.2.3 Chapter 4.....	153
5.3 Answering the research question .....	153
5.4 Impact of the work of the thesis.....	155
5.4.1 On cardiovascular imaging with PET/MRI .....	155
5.4.2 On hybrid PET/MRI imaging modalities.....	156
5.5 Future Work .....	156
Appendices.....	158
<b>Curriculum Vitae</b> .....	160

## List of Tables

Table 2-1: Estimated mean $\pm$ SD values of the parallel imaging quality parameters.....	73
Table 2-2: Percent difference of parallel imaging quality parameters comparing both 32-channel arrays. ....	78
Table 3-1: RPD of the global means for each case A, P, and A&P.....	105
Table 3-2: CR relative percentage difference between no-array and the anterior (A) part of each array for each sphere size. ....	112
Table 4-1: Relative percentage difference for non-corrected and corrected images of hardware for TX-based AC and CT-based AC methods. ....	139

## List of Figures

Figure 1-1: Illustration of beam hardening in CT image. ....	9
Figure 1-2 Illustration of two approaches of currently available Dual-energy CT scanners for dual acquisitions. ....	10
Figure 1-3 Illustration of the structure of the main components in a generic PET/MRI system. ....	13
Figure 1-4 Illustration of excitation process of nucleus by RF resonator. ....	14
Figure 1-5 Illustration of received signal from RF receiver corresponding to the FID. ....	14
Figure 1-6 Illustration of a pulse sequence of a balanced-SSFP (TrueFISP) that is commonly used in cardiac MR imaging. ....	16
Figure 1-7 Illustration of 2D Cartesian k-space matrix that produces a 2D image using 2D-FFT. ....	17
Figure 1-8 Illustration of the process of calculating the $SNR_g$ of a multi-channel phased array. ....	22
Figure 1-9 Illustration of annihilation coincidence event with two gamma-photons travelling in opposite directions. ....	24
Figure 1-10 Illustration of the type of coincidences occurs from photon emission in PET. ....	25
Figure 1-11 Illustration of axial PET image of a patient a) non-attenuation corrected (NAC) and b) attenuation corrected (AC). ....	30
Figure 1-12 Comparison between PET/MRI and PET/CT images using FDG radiotracer for a patient with cardiac sarcoid. ....	38
Figure 2-1 Phantom experiment setup for the three arrays during MRI measurements. ...	66

Figure 2-2: Noise correlation coefficients matrix for each of the three arrays. ....	74
Figure 2-3: Mean and SD of the noise correlation coefficients shown as a function of acceleration factor for the three arrays.....	75
Figure 2-4: 1/g factor maps for the three arrays with R=2 to R=6 in both LR and FH phase encoding direction.....	77
Figure 2-5: 1/g factor maps in the case of 2D acceleration with RR = 2x2 to RR=3x4. ..	78
Figure 2-6: Estimated SNR <sub>g</sub> as a function of acceleration rates from R=1 to R=6 with GRAPPA reconstruction. ....	80
Figure 2-7: Comparison of In-vivo SNR <sub>g</sub> maps generated using the three arrays at R=3 and R=4. ....	81
Figure 2-8: 4-chamber view images acquired with a 2D TrueFISP cine sequence on a male volunteer.....	82
Figure 2-9: A centre line profile of the SNR <sub>g</sub> map of the heart for the three arrays.....	83
Figure 2-10: PET counts per second (CPS) map of the middle slice of the Ge-68 phantom for each array separately and reference (“no-array, no-table”).....	84
Figure 3-1:NEMA body phantom (a) together with the novel PET/MRI 32ch, standard mMR12ch and MRI 32ch arrays.....	99
Figure 3-2: Non attenuation correction (NAC) and relative percentage difference (RPD) plots for each array for all cases A, P, A&P. ....	106
Figure 3-3: Reconstructed AC images of the NEMA-phantom and RPD maps for all cases (no-array, A, P, A&P).....	108
Figure 3-4: Contrast recovery vs. background variation (from six spheres) for each array. ....	110



Figure 3-5: CNR, BV and CR data for each anterior component of the three arrays are compared to no-array for all spheres. ....	113
Figure 4-1: Illustration of physical relation of hardware voxels position ( $p$ ) along a LOR and corresponds to voxel indices ( $j$ ) and detector indices ( $i$ ).....	126
Figure 4-2: The apparatus (TX-fixtured) and setting used in PET acquisitions. ....	128
Figure 4-3 Flow chart describing the process of generating hardware TX-based AC map. ....	130
Figure 4-4: Theoretical estimation of acrylic material from mapped LAC values from 0.1 to 1.0 MeV. ....	135
Figure 4-5: Line plot of a profile from pixels centred on the PET image for the three-hardware.....	137
Figure 4-6: RPD of NAC, TX-based AC and CT-based AC PET images for the hardware under examination.....	138
Figure 4-7: Fused images of $^1\text{H}/\text{FDG}$ for a volunteer, using TX-based and CT-based $\mu$ -maps of the patient table. ....	140
Figure 4-8: RPD map of in vivo PET data resulted from comparing TX-based AC to CT-based AC and RPD map of the hardware AC maps. ....	141
Figure 4-9: Polar plot of 17-segment for the LV short-axis of the heart, using TX-based AC and, CT-based AC. ....	142

## List of Appendices

Appendix 1: Research ethic approval letter for human studies carried in chapter 2. .... 158

Appendix 2: Research ethic approval letter for human studies carried in chapter 4. .... 159

## List of Abbreviations and Symbols

$\omega$	Frequency (rad/s)
$\mu$	Linear attenuation coefficient
$\gamma$	Gyromagnetic ratio
$^{18}\text{F}$	$^{18}\text{Fluorine}$
$^{68}\text{Ge}$	$^{68}\text{Germanium}$
$^{68}\text{Ga}$	$^{68}\text{Gallium}$
$^1\text{H}$	Hydrogen nuclei, proton
2 -3D	Two- or three-dimensions
AC	Attenuation Correction/ Corrected
ANOVA	Analysis of variance
$B_0$	External static magnetic field
$B_1$	Applied radiofrequency magnetic field
BH	Breath hold
BR	Breathing rate
Bq	Becquerel
BV	Background variation
CAD	Computer aided design
CNR	Contrast-to-Noise Ratio
Cps	Counts per second
CR	Contrast recovery
CT	Computed tomography
CTAC	Computed tomography-based attenuation correction

CVD	Cardiovascular disease
DECT	Dual-Energy Computed Tomography
FBP	Filtered Back-Projection
FID	Free-induction decay
FDG	<sup>18</sup> F-labeled fluorodeoxyglucose
FOV	Field of view
FWHM	Full-width-half-maximum
G <sub>x</sub>	X-gradient (Frequency-encoding gradient)
G <sub>y</sub>	Y-gradient (Phase-encoding gradient)
G <sub>z</sub>	Z-gradient (Slice-encoding gradient)
HU	Hounsfield Unit
LAC	Linear attenuation coefficient
LOR	Line of response
IR	Iterative Reconstruction
keV	Kilo electron volt
M <sub>0</sub>	Net equilibrium magnetization
MPRAGE	Magnetization Prepared Rapid Acquisition gradient-echo sequence
MRAC	MRI-based attenuation correction
MRI	Magnetic resonance imaging
NAC	Non-Attenuation Correction/Corrected
OP-OSEM	Ordinary Poisson-Ordered Subsets Expectation Maximization
PET	Positron emission tomography
RPD	Relative Percentage Difference

RF	Radiofrequency
ROI	Region of Interest
SNR	Signal to noise ratio
SNR <sub>g</sub>	g-factor-based signal-to-noise ratio
T	Tesla
TA	Total acquisition time
T1	Spin-lattice relaxation
T2	Spin-spin relaxation
TE	Echo time
TR	Repetition time
TrueFISP	True Fast Imaging with Steady-state Precession
VIBE	Volumetric Interpolated Breath-hold Examination
UTE	Ultra-short echo
Z	Atomic Number

# Chapter 1

## 1 Introduction

### 1.1 Background

#### 1.1.1 Motivation

Cardiovascular diseases (CVD) cause 31% of all illness-related deaths globally and are considered to be the second cause of death in Canada<sup>1,2</sup>. According to the 2018 Health Canada report<sup>2</sup>, CVD is estimated to directly cost the Canadian economy about \$2.8 billion per year<sup>3</sup>, while the American Heart Association (AHA) reported a direct cost of \$213.8 billion to the US economy<sup>4</sup>. The statistics data from 2012 and 2013, shows approximately 2.4 million adults Canadian (of age  $\geq 20$  years) suffer from ischemic heart disease, where 24.1% of them have history of an acute myocardial infarction, and 27.1% of them in the age 40 or more, were living with heart failure<sup>5</sup>.

Although remarkable advancements in the prevention and management of heart disease have been made in the last few decades, the burden remains high and sustained efforts are needed to ensure early diagnostic and treatment<sup>6</sup>. As per the Canadian Heart and Stroke Foundation (CHSF) report in 2016, while several diagnostic tests are well established to identify heart failure caused by cardiovascular diseases, access to specialized services, including advanced diagnostic methods, is very low. Therefore, CHSF recommendation to healthcare providers was improve and facilitate such services which are required to achieve early diagnosis for heart diseases including cardiovascular<sup>7</sup>. Given this current situation, it is vital to develop the most effective and efficient methods and tools to diagnose accurately cardiac diseases and their causes.

Cardiovascular diseases are a collection of disfunctions of the heart and blood vessels, that affect the heart and the brain<sup>1</sup>, and can be grouped into two categories. The first category belongs to coronary artery diseases caused by deposition of plaques of fatty material on inner arteries walls. This includes for example: a) coronary artery diseases of the blood vessels of the heart which can cause myocardial infarction; b) diseases of the blood vessels to the brain, known as cerebrovascular, which can cause ischemic stroke; and c) peripheral arterial diseases which targets blood vessels supplying the arms and legs, which can result in hypertension. The second category is the CVD caused by impairment or ailment of the heart. This includes for example: a) cardiac arrhythmias, which are described as abnormalities of rate or rhythm of the heart; b) abnormal heart muscle known as cardiomyopathy; c) congenital heart disease, due to abnormality and/or defects of the heart, from the time of birth<sup>8</sup>.

The diagnosis of heart diseases has come a long way since the invention of the Electrocardiography by Waller 130 years ago<sup>9</sup>. Since then, different imaging modalities are used for clinical diagnostics of cardiovascular diseases such as, nuclear cardiology<sup>10</sup>, echocardiography (ECG)<sup>11</sup>, magnetic resonance imaging (MRI)<sup>12</sup>, cardiac computed tomography (CT)<sup>13,14</sup>, single photon emission computed tomography (SPECT)<sup>15</sup>, positron emission tomography (PET)<sup>16</sup> and coronary angiography<sup>17</sup>. Each modality has greatly broadened the capability of understanding some of the CVD, however, each imaging modality is limited in only providing part of the needed information at the anatomical functional and molecular level. Understanding the dynamics of cell biology to the molecular level is a key to understanding and treating the conditions associated with CVD.

This has led to the integration of complementing-modalities into the hybrid diagnostic platform, like the PET/MRI.

For almost a decade, the integrated hybrid PET and MRI (PET/MRI) systems have been used successfully in cardiovascular studies<sup>18</sup>, with growing concerns that this platform will improve timely diagnosis of cardiac diseases<sup>19-21</sup>. However, hybrid PET/MRI still lacks a few critical components before reaching reliable and accurate measurements of cardiac anatomy, function, metabolism and cellular/molecular, which are still challenging<sup>22-26</sup>. Some of the challenging components are related to hardware and software of this hybrid platform. This includes: a) radio frequency phased array capable of fast acquisition of high resolution MRI images using 3D imaging and 2D acceleration; b) software including MR imaging pulse sequences capable of achieving fast acquisitions and high temporal resolutions; c) software algorithms for the reconstruction of PET images free of motions artifacts; and d) techniques and methodologies to correct for attenuated photons in PET images caused by the presence of both the patient body and, the hardware used for the PET/MRI simultaneous acquisitions.

It becomes therefore apparent, that addressing these technical challenges associated with the integration of PET/MRI modalities may significantly enhance the role of this hybrid platform in reliable and accurate cardiac diagnosis. The goal of the research reported in this thesis was to improve both, PET and MRI images of the heart, on hybrid PET/MRI systems. Three objectives supporting this overall goal were set, objective 1- provide a novel concept of RF phased array for the hybrid PET/MRI platform, capable of achieving high spatial (1mm) and temporal resolutions (improving upon current vendors array). Objective 2- Implement a novel concept of the RF phased array that provides no-to-



minimum photon attenuation (less than 5%). Objective 3- develop a novel hardware attenuation correction method for accurate PET quantification. The author anticipates that through these two novel approaches to address these three objectives, better and less expensive approaches to heart imaging will emerge increasing heart patient access to this hybrid technology.

### 1.1.2 Thesis outline

The thesis is structured so that, each topic is gradually reviewed from its basics to today's cutting-edge-research status, in order to provide the reader with a wider understanding of each topic and its relationship to the objectives. In chapter one, the introduction, the principles of each imaging modality related to this work are reviewed separately and a brief review of each modality temporal and spatial resolution is described. First, the principle of computed tomography, from theory to creating an image, is explained. This is followed by reviewing the principles of magnetic resonance imaging and the process of acquiring an image. The introduction also discusses the principles of RF phased arrays, and their use in parallel imaging to produce fast and high-resolution MR images. This also includes a review of the currently used RF phased arrays in cardiovascular MR imaging. Thereafter, the principles behind positron emission tomography are explained followed by a review of the challenges the PET modality faces, such as the attenuation effect, including their causes and approaches to resolve such effects. Integrated imaging modalities, or often referred to as hybrid systems, such as PET/MRI, is discussed with a focus on cardiovascular diseases. Afterwards, the photon attenuation challenge in an integrated PET/MRI system is visited, including a review of the current approaches and methods to address this issue. The introduction is then concluded by describing the relationship between hardware components of the hybrid PET/MRI system and the accuracy of diagnosis in cardiovascular diseases. By the end of chapter one, research questions with the thesis objectives and means of achieving them, are articulated.

Chapter two is a published work of objective one of the thesis, which addresses the imaging quality of a novel prospectively-designed 32 RF receivers phased array for cardiac

PET/MRI system. In this chapter, a comprehensive review of current devices and their pros and cons are considered. Measurements of quality parameters of images produced by the phased array are reported and compared to other available arrays.

Chapter three is the work published on the PET imaging performance for the same phased array which covers the second objective of the thesis. The novel phased array performance under PET environment is described in terms of the quality parameters for PET imaging, such as, contrast recovery, background variations and contrast-to-noise ratio. Comparison of these parameters of the novel array with two vendor arrays are reported demonstrating statistical significance improvements.

In chapter four a novel approach of hardware attenuation correction is described in detail, which covers the third objective of the thesis and is currently under peer review by a scientific journal. The theory behind attenuation correction using a static radioactive transmission source is explained, together with the validation technique of the theory. This chapter also demonstrates an application of the novel method in cardiovascular hybrid PET/MRI imaging.

Chapter five, summarizes the findings from the work reported in chapters two, three and four. An inclusive conclusion on the goal of the thesis is then presented, followed by elaboration on the significance of the research and its contribution to PET/MRI cardiovascular imaging. Finally, future work and potential applications of the novel work of the thesis, are suggested.

## 1.2 Principles of selected imaging modalities

### 1.2.1 CT imaging modality

#### 1.2.1.1 Principle, data acquisition and image reconstruction

The CT concept was first introduced by Godfrey Hounsfield in 1973<sup>27</sup>, while its mathematical principle was developed by Radon in 1917. A CT modality system simply consists of a rotating x-ray source(s) and its detector(s) at the opposite side, where the object to be imaged is positioned between the source and the detector. A CT acquisition measurement is made by the ray (from an x-ray) passing through the object, where each point produced in the image represents the attenuation property of that region of the object<sup>28</sup>. A 2-dimensional (2D) image can only be acquired through the simultaneous rotation of the x-ray source and detector, so both posteroanterior and lateral projections can be acquired. For 3D acquisition, the scanner adapts the technique of moving the patient bed in superior-inferior direction or vice versa, which results in a helical-shaped projection. Image reconstruction for CT modality has historically used a filtered back-projection algorithm<sup>29</sup>, but in recent years iterative methods are being used more, resulting in reduced radiation dose and improved signal to noise ratio. Then, another algorithm interpolates the data into a series of planar images to account for the helical effect. The reconstructed CT image is scaled, according to Hounsfield, so that air radiodensity is equivalent to -1000 Hounsfield units (HU), while water radiodensity is 0 HU and bone density is >100 HU. Therefore, each voxel raw data  $V(x,y)$  in a 2D matrix, is calculated from the relation in equation 1:

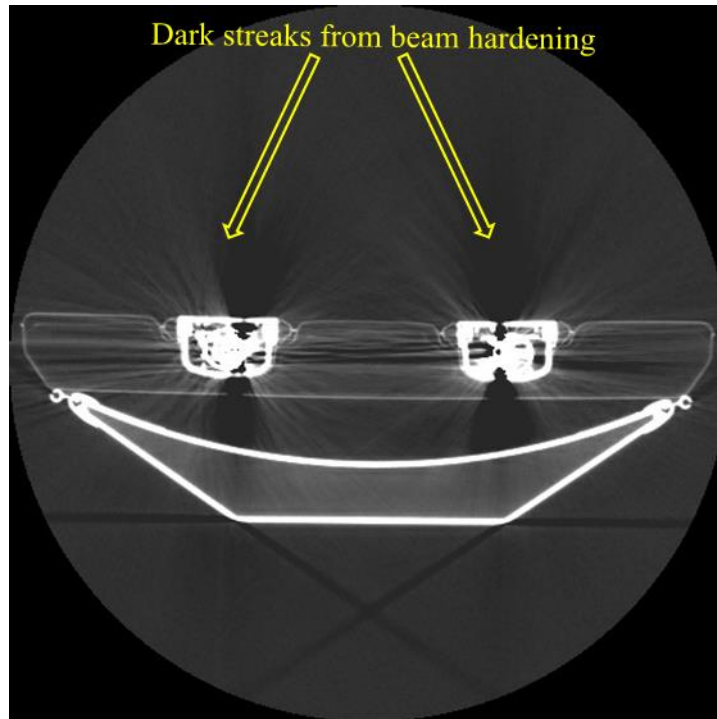
$$V(x, y) = 1000 \times \frac{\mu(x, y) - \mu_{\text{water}}}{\mu_{\text{water}}} \quad (1)$$

Where  $\mu_{\text{water}}$  is the attenuation coefficient of water and  $\mu(x, y)$  is the attenuation coefficient of material at voxel  $V(x, y)$ .

### 1.2.1.2 CT image artifacts

CT modality is the highest in temporal (83–135 ms) and spatial (0.5–0.625mm) resolutions in comparison to PET and MRI<sup>30</sup>. Nevertheless, artifacts in images produced from CT modalities exists, such as partial volume averaging, motion artifact<sup>31</sup>, and beam hardening<sup>32</sup>. The most related artifact to the work of this thesis is the beam hardening. When low energy x-ray is attenuated by a high-density and high atomic number (Z-number) material, the x-ray energy distribution is skewed towards high energies as lower energies are preferentially absorbed. This increase in the average energy of x-ray distribution is known as beam hardening. Beam hardening causes more photons to be detected (artificially) than would be detected if the x-ray energy distribution had not been changed. This results in dark streaks artifacts in the image data. In figure 1-1, dark streaks are visible in the CT image as a result of beam hardening, which in this example produced by the RF metal components in a RF receivers' array. Beam hardening can also cause poor quality and inaccurate attenuation coefficient maps, which will be discussed later in section 1.2.3.6. In a single energy CT scanner, beam hardening correction technique, such as Bow tie filters, is normally included and applied before reconstruction. However, these correction techniques are not adequate to correct for higher electron densities materials, as in metals found in RF arrays.

**Figure 1-1: Illustration of beam hardening in CT image.**



**CT image of a posterior part of RF array and patient table containing high density material**

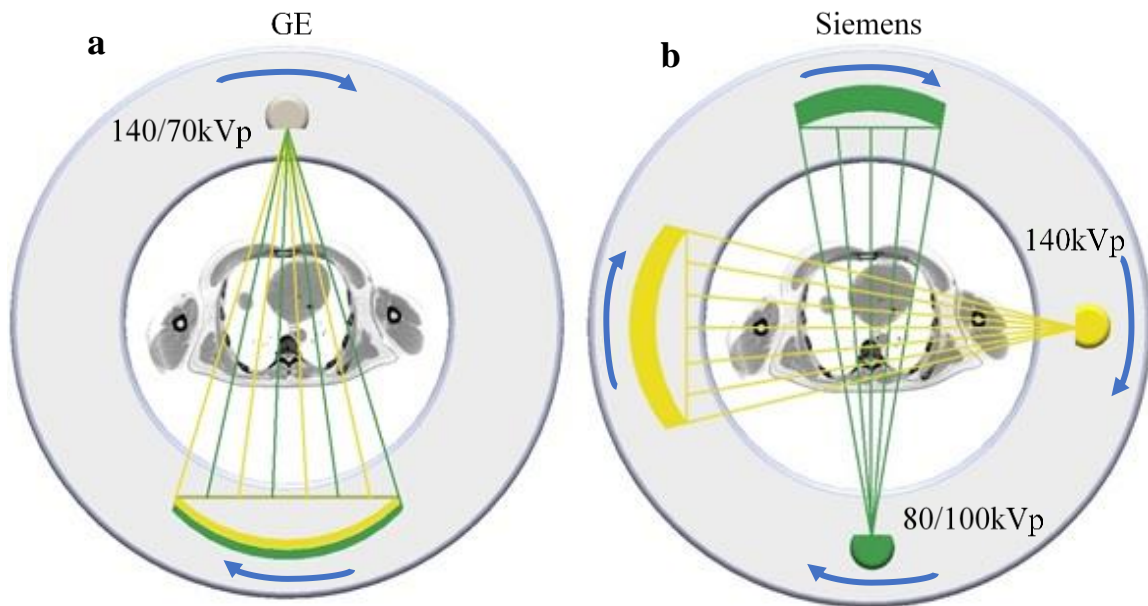
### 1.2.1.3 Dual-energy Computed Tomography

Dual-energy computed tomography (DECT) scanners can perform imaging at two different energy levels (figure 1-2), either by rapidly switching one x-ray tube voltage between low (i.e 70kVp) and high (i.e 140kVp) energies<sup>33,34</sup>; or by incorporating two x-ray tubes each for the two energies<sup>35</sup>. In attenuation correction, DECT reduces beam hardening effects by scanning at two different energies<sup>32,36</sup>, by generating virtual monochromatic images, however, they are known to be problematic because of the noise amplification produced<sup>36</sup>. DECT reduces beam-hardening artefacts caused by materials with higher electron densities

like iodinated contrast agents, however, it does not eliminate the beam hardening for higher Z material like metals <sup>37</sup>.

Although the CT technology has impressively evolved since it was first introduced in 1973, still ionizing radiation dose to the patient remains a drawback<sup>38</sup>.

**Figure 1-2 Illustration of two approaches of currently available Dual-energy CT scanners for dual acquisitions.**



**Dual Energy CT available for dual acquisitions; (a) single x-ray source alternating rapidly between 140 and 70kVp energy; (b) simultaneous dual x-ray sources at each energy level.**

## 1.2.2 MRI imaging modality

### 1.2.2.1 Principle of the MRI modality

The principle of signal detection and image creation in the MRI system is described as the process of excitation and relaxation of a given nucleus. Excitation is the change of the nucleus state from thermal equilibrium to a high energy state, while relaxation is simply the return of the nucleus back from its high energy to thermal equilibrium state. As the nucleus returns back to its thermal equilibrium (relaxation process), the signal is detected to create an image. When the tissues are present in the magnetic field, provided by the permanent magnet in the MRI system (fig 1-3), the nuclei have a net equilibrium magnetization ( $M_0$ ) and mostly are aligned with the static magnetic field  $B_0$  along the z plane, and the net magnetization vector will have two components longitudinal ( $M_z$ ) and transvers ( $M_{xy}$ ). At this state, the nuclei are precessing at their natural resonance frequency, known as Larmor frequency ( $\omega$ ). The excitation happens by means of changing the nuclei magnetization magnitude and direction from low energy state resulting in a net magnetization in the transvers plane x and y ( $M_{xy}$ ). The excitation requires applying a secondary electromagnetic field ( $B_1$ ) at the exact precessing frequency of the nuclei for a given magnetic field strength which is achieved using specially designed devices namely RF resonators (fig 1-3 b). The RF electromagnetic energy causes the nuclei to tip with a certain degree (flip angle), that is proportional to the RF strength and duration of echo time (TE), from longitudinal (z axis) to transvers planes (x, y axes) as in fig 1-4 -a. Therefore, when a maximum transverse magnetization is desired, one must achieve  $90^\circ$  flip angle by



the RF transmit (Tx) resonator tuned to the Larmor frequency of the targeted nuclei with a known gyromagnetic ratio ( $\gamma$ ), where the Larmor frequency is determined by the relation;

$$\omega = \gamma B_0 \quad (2)$$

After an RF pulse is applied, nuclei precession decay in the transverse plane in a short time which is known as spin-spin relaxation or  $T_2$  (fig 1-4 -b), while the nuclei also relax back to their lower energy state along the z-axis, where  $M_z$  grows in a longer time known as spin lattice relaxation or  $T_1$ .

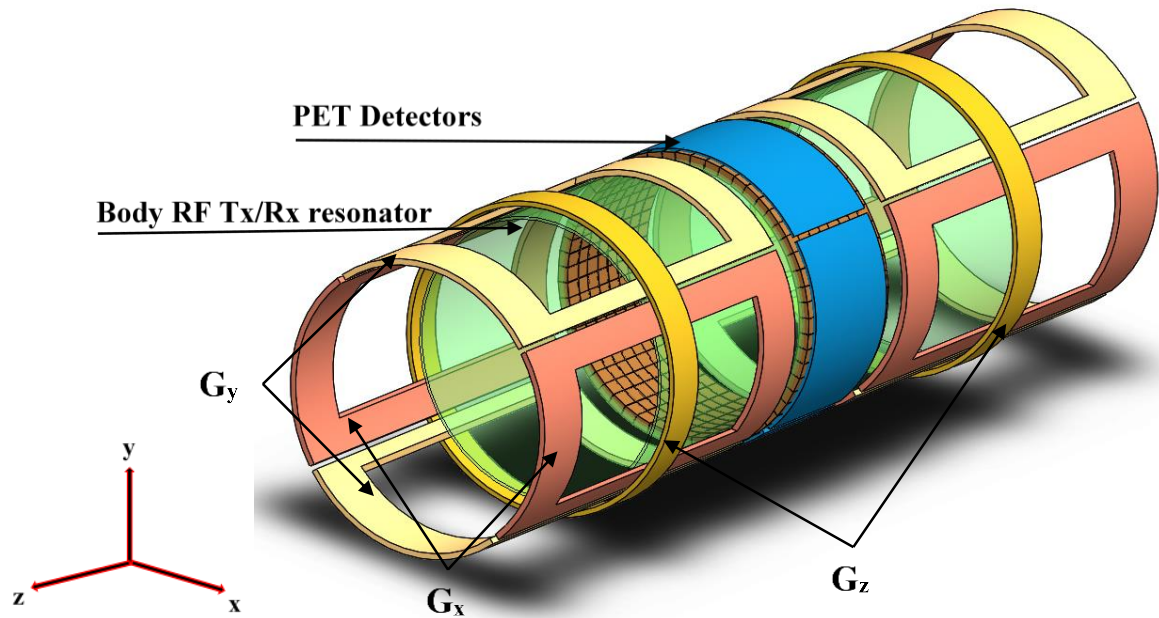
The mathematical relationship describing the two process of  $T_2$  and  $T_1$  relaxation over time ( $t$ ) with respect to transverse and longitudinal components of magnetizations, are described respectively in equations 3 and 4:

$$M_{xy}(t) = M_0 e^{-t/T_2} \quad (3)$$

$$M_z(t) = M_0 (1 - e^{-t/T_1}) \quad (4)$$

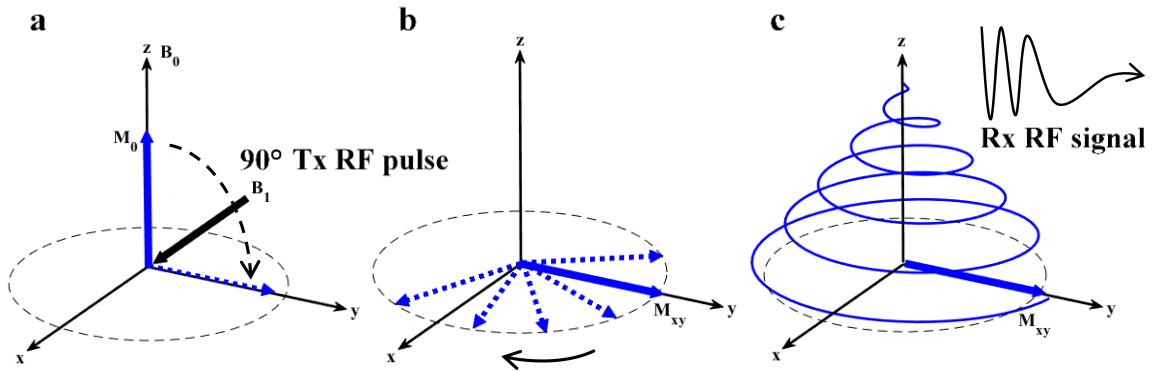
The RF Tx part of the resonator excites the nuclei, while the RF receiver part (Rx) picks up the induced voltage from the nuclei during the process of relaxation (fig 1-4 -c), and results in a signal in the form of free induction decay (FID) (fig 1-5 a). FID signal is therefore produced from a complete excitation and relaxation, and by repeating (repetition time TR) this process many times resulting in an image.

**Figure 1-3 Illustration of the structure of the main components in a generic PET/MRI system.**



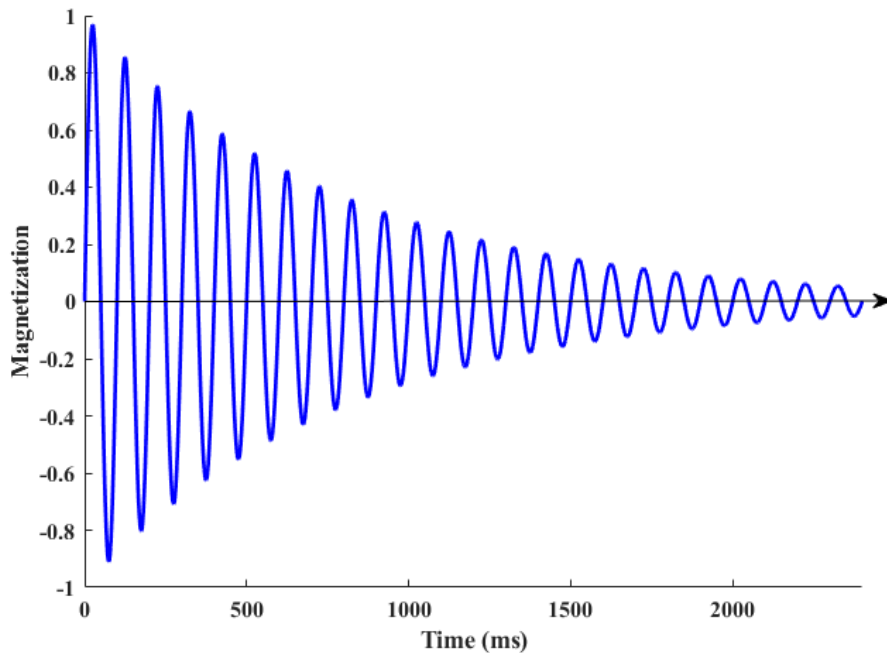
The illustration of the system showing; body RF resonator (green), the set of gradient coils ( $G_x$ ,  $G_y$  and  $G_z$ ) perpendicular to each other's plane, and a PET detector ring (blue) between two left and right sets of gradient coils. (This illustration does not represent the exact design)

**Figure 1-4 Illustration of excitation process of nucleus by RF resonator.**



The excitation for a nucleus from low energy (thermal net equilibrium) along z-axes to high energy state with a net transverse magnetization  $M_{xy}$ . b) transverse magnetization precessing in the x,y plane decreases over time ( $T_2$ ); c) Relaxation process from transverse to longitudinal magnetization with the spiral as a representation of the net magnetization vector with net precession ( $T_1$  and  $T_2$ ).

**Figure 1-5 Illustration of received signal from RF receiver corresponding to the FID.**



A set of controllable gradient coils produce electromagnetic fields with varied intensity along the x, y and z axes of the MRI scanner (fig 1-3). The gradient coils are capable of producing a magnetic field gradient along any single plane or combined planes, in order to achieve the desired orientation of the magnetic field gradient. They locally alter the strength of the main magnetic field  $B_0$ , which changes the precessing frequency between slices and hence they can be used for slice selection, phase-encoding and frequency encoding (read-out). Each gradient coil is named after its annotation i.e.  $G_x$  is the x-gradient along x axis, and enables sagittal imaging, while  $G_z$  is z-gradient along the z axis, and allows for axial imaging, and so on.

#### 1.2.2.2 Image acquisition and reconstruction

Acquisition of MR image follows the set of processes described above (excitation, relaxation, localization /selection and sampling/writing the data), which are organised in a precise sequential order, known as a pulse sequence. The most fundamental pulse sequence in MRI are the gradient echo (GRE) sequence and spin echo (SE) sequence, both from which many other sequences were developed, i.e. balanced steady-state free precession sequence (balanced-SSFP) shown in figure 1-6-a and is used in chapter 2.

For a 2D image, a single FID signal is acquired in the time domain and recorded as complex values, namely k-space, representing both magnitude and phase of the MRI signal, which is arranged in a 2D matrix. The 2D matrix containing data collected in k-space is filled during acquisition with the frequency encoded data from  $k_x$  to  $k_{+x}$  direction, while the phase encoding data are filled from  $k_y$  to  $k_{+y}$  direction, in a Cartesian fashion (figure 1-7 - b). However, there are other ways to fill the k-space, such as spiral acquisition, radial

acquisition etc. To create the 2D image in laboratory spatial co-ordinates one must transform the 2D k-space data using the 2D Fourier relation shown in (eq. 5).

$$G(k_x, k_y) = \iint_{-\infty}^{+\infty} g(x, y) e^{-2\pi i k_x x} e^{-2\pi i k_y y} dx dy \quad (5)$$

Where  $g(x, y)$  is function of real variables of  $x$  and  $y$  known as Fourier conjugates, and  $G(k_x, k_y)$  is the complex 2 D Fourier transform of  $g(x, y)$

**Figure 1-6 Illustration of a pulse sequence of a balanced-SSFP (TrueFISP) that is commonly used in cardiac MR imaging.**

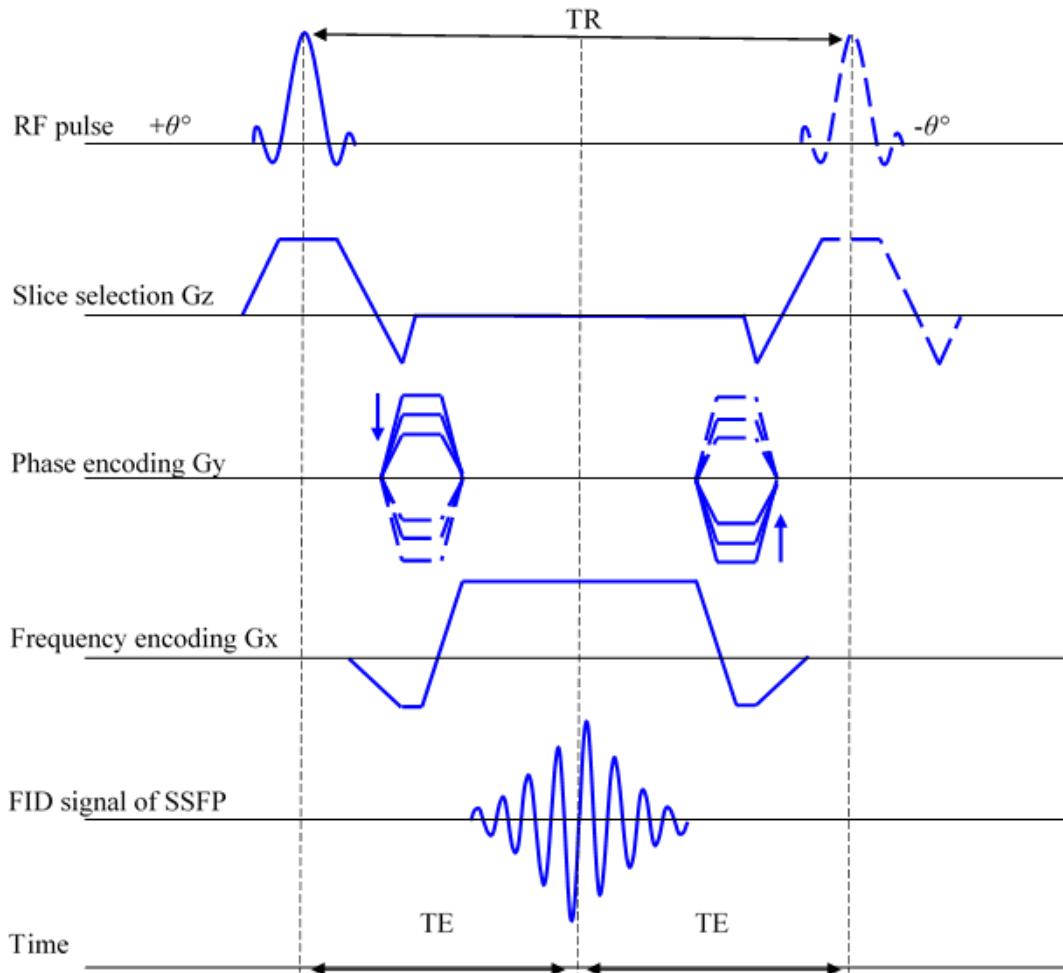
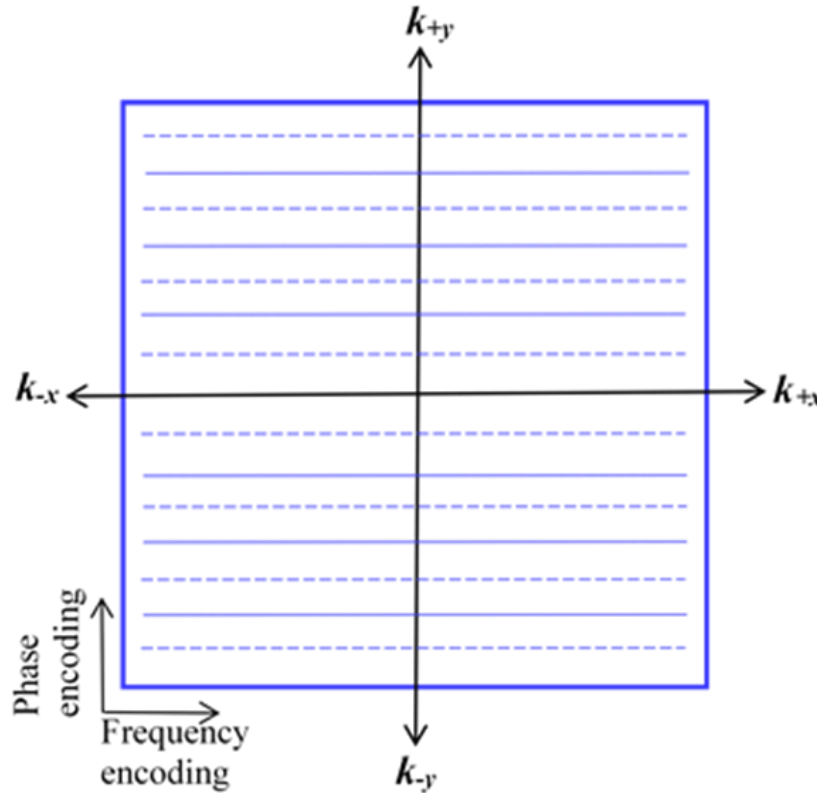


**Figure 1-7 Illustration of 2D Cartesian k-space matrix that produces a 2D image using 2D-FFT.**



Each line is filled during each TR along the frequency-encoding axis ( $G_x$ ), where the location of the lines with respect to y-axis depends on the phased encoding gradient pulse ( $G_y$ ). When all lines (solid and dashed) are filled, the k-space is fully sampled, while skipping dashed lines would result in under-sampled k-space, which accelerates the image acquisition and construction used in parallel imaging. If every other line is skipped in the  $k_y$  axis the acceleration factor  $R = 2$  and acceleration is in one dimension.

### 1.2.2.3 Temporal and spatial resolution for image quality

Although the temporal and spatial resolution achieved today by cardiac MRI, close to or exceeds those provided by CT and PET imaging modalities<sup>30</sup>, imaging with MRI system has continued to strive to achieve better spatial and temporal resolutions. Spatial resolution

relates to the size of the voxel in the image, where, the smaller the achieved voxel size, the higher spatial resolution, hence higher image detail. On the other hand, the temporal resolution relates to how fast the data is acquired and an image is reconstructed. Achieving both spatial temporal resolutions requires optimization of both the RF resonators and the pulse sequence together with its associated image reconstruction algorithm. Relying on the integrated body resonator in MRI system, the imaging is limited to one element that transmits and the same element receives, which limits the ability to resolve details spatially in the image. This also results in very long imaging times, due to the number of lines on k-space to be filled from only one element receiver. Therefore, to achieve spatial resolution, beside optimising the pulse sequence, the approach of using RF resonator with multiple elements, namely RF arrays, allows acquisition from large areas at the same time (improved coverage)<sup>39</sup>. Since small elements have intrinsically high sensitivity in comparison to a large element, when employing many small elements, a larger volume in the imaging field-of-view (FOV) is covered with high sensitivity<sup>40,41</sup>. Consequently, arrays with multiple small elements with high sensitivity allow the achievement of higher spatial resolution.

#### 1.2.2.4 Parallel imaging

Efficiently acquiring the signals from several channels simultaneously requires a special technique of imaging known as parallel imaging<sup>42,43</sup>. This is achieved using specially designed pulse sequences matched to specific reconstruction algorithms, such as; Sensitivity Encoding (SENSE)<sup>42</sup>, Simultaneous acquisition of spatial harmonics (SMASH)<sup>43,44</sup>, or Generalized auto-calibrating partially parallel acquisitions (GRAPPA)<sup>45</sup>. Parallel imaging has tremendously shortened the time of the acquisitions themselves and

the time between one acquisition and the other<sup>46</sup>. It is therefore, with the combination of pulse sequence modifications and, using multiple receiver element RF phased arrays<sup>39</sup>, that high temporal and spatial resolutions can be achieved<sup>43,47</sup>. Other solutions for temporal resolution in MRI are reported using rectangular small FOV, or using partial Fourier transform reconstruction<sup>48,49</sup>, both of which the number of lines of k-space are reduced, hence acquisition time and reconstruction time is shortened. This reduction of the acquisition time due to a reduction in the number of acquired lines of the k-space is called acceleration, and measured as the ratio of the unaccelerated acquisition time to the accelerated acquisition time<sup>50,51</sup>. The technique of parallel imaging enhances the time efficiency in filling k-space by utilizing the overlapping sensitivity profiles from multiple RF elements to mathematically reconstruct the missing lines<sup>52</sup>. The technique is useful in reducing the scan time in applications such as contrast enhanced cardiac MRI for shortening the breath-hold<sup>53</sup>. Employing parallel imaging with sequences such as gradient echo SSFP, known also as true fast imaging with steady-state precession (TrueFISP), can achieve short acquisition time and high signal-to-noise ratio (SNR)<sup>54,55</sup>. However, the SNR and image acceleration that can be achieved using parallel imaging is limited by the geometric factor of the elements which is known as the g-factor<sup>56-58</sup>. SNR for a single receiver element, is the ratio of induced signal to the root mean square of the thermal noise voltage. SNR of an image from a single element, can therefore be estimated from the mean signal divided by the standard deviation of the magnitude background noise of the same image. However, in a phased array with multiple elements, noise from each element may correlate causing a spatial variation (nonuniform noise) of the overall noise in the composite image. The noise correlation, and hence, noise variation (noise covariances



matrix) must therefore be considered to accurately estimating SNR for phased arrays. In addition, in parallel imaging with phased array, reducing number of k-space lines to accelerate the acquisition results in the reduction of the FOV, which consequently causes aliasing (superposition). To undo the signal superposition caused by combining elements-signals, each element sensitivity with its weight is used<sup>42</sup>. The sensitivity of each element together with noise correlation are then computed to estimate the g-factor which can then be used to determine the g-based SNR, namely,  $SNR_g$ . In chapter 2,  $SNR_g$  together with SNR with no acceleration technique are used to evaluate the phased array MRI performance at different acceleration factors.

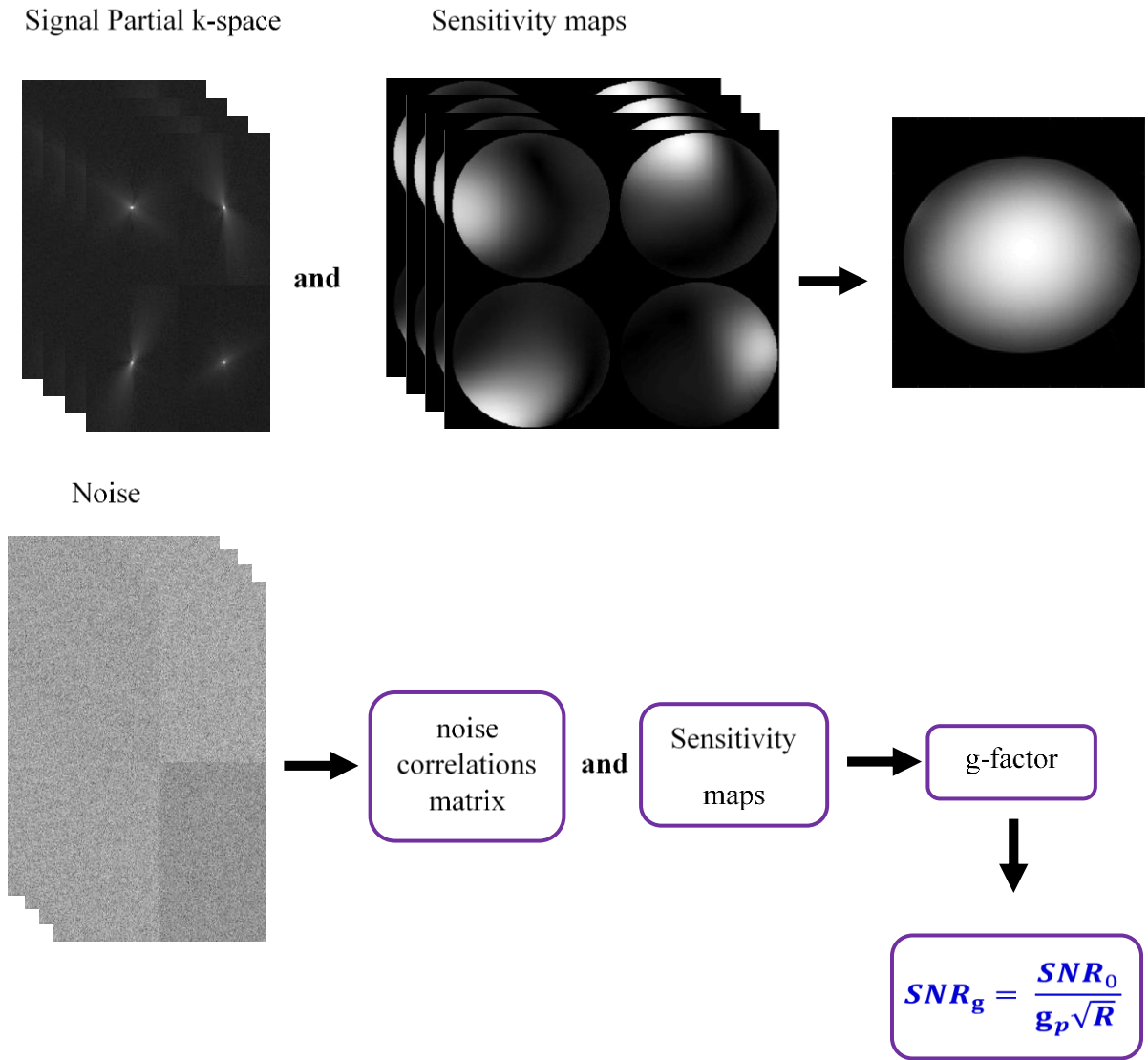
#### 1.2.2.5 Phased arrays

The concept of phased array in MRI refers to multiple receiver elements (sometimes also called as channels) with the property of correcting the polarization of the received signal simultaneously at each point, by the choice of phases and amplitudes when combining the signals<sup>39,59</sup>.

One of the early demonstrations of the advantage of the phased array in cardiac MR imaging has been reported at 1.5T with an overall enhancement of the SNR for the entire heart<sup>59</sup>. Since then, several phased array resonators with a different number of channel elements were developed<sup>50,51,60-62</sup>, with mainly two goals to achieve, these are: 1- highest acceleration factor through increase of number of channels<sup>61</sup>, and 2- best geometrical overlapping of the channels to reduce the g-factor<sup>51</sup>. Achieving these two goals allows for the acquisition of a fast (temporal resolution), high  $SNR_g$ , well spatially resolved image.

Both g-factor and  $\text{SNR}_g$  for an RF phased array must therefore be evaluated at each acceleration factor to determine its suitability for parallel imaging. Therefore, the most suitable RF phased array for parallel imaging is determined by the highest acceleration factor without substantial degradation of the SNR, which depends on the g-factor<sup>56,58,60,63,64</sup>. In such evaluation the noise from each channel is measured and a correlation between all channels is determined and arranged in a noise-correlation matrix with its dimension equal to the number of the elements in the array<sup>65</sup>. As depicted in figure 1-8, the noise correlation matrix is used with the sensitivity map for each channel to calculate the g-factor and hence the SNR at different acceleration factors<sup>42,63</sup>.

**Figure 1-8 Illustration of the process of calculating the  $SNR_g$  of a multi-channel phased array.**



The process of calculating the g-factor and  $SNR_g$  of a multi-channel phased array for any given acceleration is shown, where  $R$  is the acceleration factor, and  $SNR_0$  is the fully sampled image SNR. The method uses both k-space data of the signal (top) and the noise.

### 1.2.3 PET imaging modality

#### 1.2.3.1 Radiotracers used in PET

When radioactive isotopes are arranged in a compound, such as  $^{18}\text{F}$ -fluorodeoxyglucose (FDG) with ability to be administered to the body, the glucose adds a metabolic property to the compound. Therefore when administered it tends to attach itself to the glucose metabolism in cells, and for certain organs as well as tumors more radiotracer are attached, results in the FDG compound acting as a tracer and a label of the diseased cells<sup>66-68</sup>

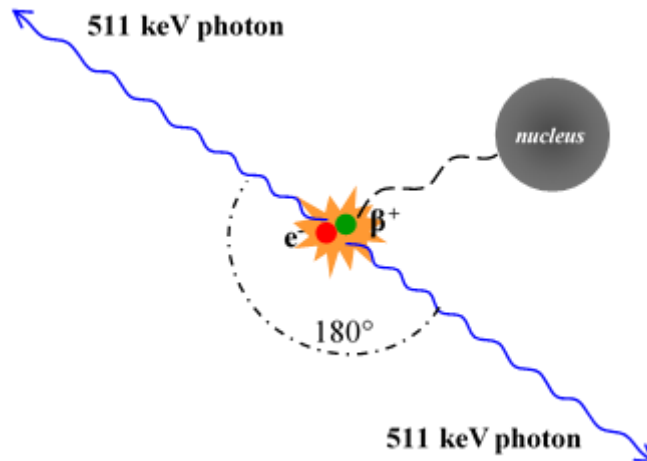
#### 1.2.3.2 Principle of PET modality

Radioactive isotopes such as  $^{11}\text{C}$ ,  $^{15}\text{O}$ ,  $^{13}\text{N}$ , and  $^{18}\text{F}$  decay by isotropically emitting positively-charged particles ( $\beta^+$ ) namely, positrons<sup>69</sup>. Each positron released has kinetic energy characteristic of the originating nucleus, which it loses during its interaction with electrons ( $e^-$ ) from the surrounding matter. Once the positron has slowed down sufficiently, final interaction between a positron (+) and an electron (-), annihilation of the electron occurs and yields two photons radiating with energy of 511keV which is known as gamma rays<sup>70</sup>. Emitted pair of photons from the annihilation process travel generally in opposite directions (nearly  $180^\circ$ ) of each other (figure 1-9), which gives the opportunity to detect and confirm the annihilation event (also known as coincidence) using a pair of appropriate detectors<sup>70</sup>.

The PET scanner contains a number of rings, where each ring includes a set of detectors arranged in a circle and covers  $360^\circ$ , around the target-body to be imaged. The signal acquired by the PET system is generated when an annihilation occurs and the two photons are detected by a pair of detectors at opposite sides, simultaneously, on the same line, which

is known as the line of response (LOR). PET detectors are array of scintillation crystals. In the past the scintillation produced in the crystals by the 511keV gamma rays were detected by a photo multiplier tube (PMT)<sup>70</sup>. However as PMT are sensitive to the magnetic field in the hybrid PET/MRI system, they have been replaced by Avalanche photodiodes and silicon photomultipliers<sup>71</sup>.

**Figure 1-9 Illustration of annihilation coincidence event with two gamma-photons travelling in opposite directions.**

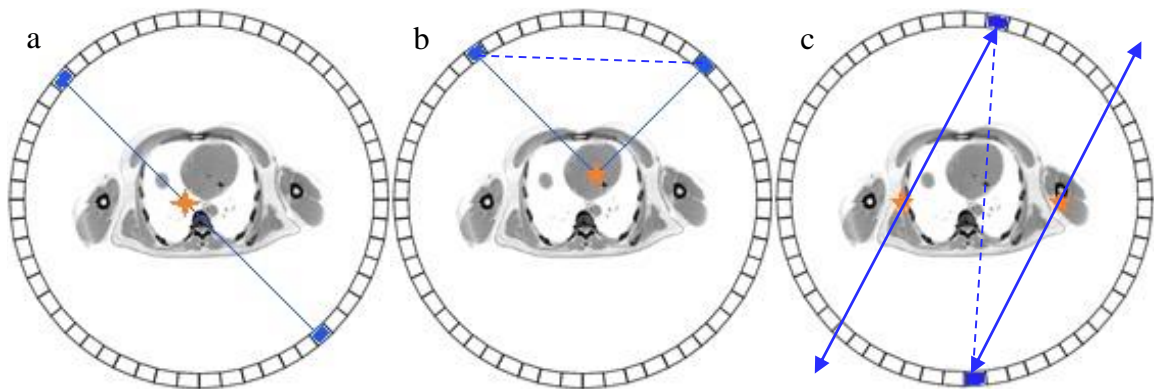


**Annihilation coincidence event occurred when positron emitted from a decayed nucleus of the radioactive tracer interacts with electron from the tissue. The positron annihilates with the electron resulting into two gamma-photons travelling in opposite directions.**

Recorded coincidences from annihilation are classified into three main categories as shown in figure 1-10; a) true coincidence, which occurs when one annihilation and two photons are detected at opposite detectors within a specific time window; b) scatter coincidence,

where one annihilation occurs, but one or two of the photons are scattered, and both are detected, and; c) random coincidence, where two true coincidences occur resulting in an artificial line of response (dashed blue line in figure 1-10-c), and only one coincidence (two photons) are detected simultaneously.

**Figure 1-10 Illustration of the type of coincidences occurs from photon emission in PET.**



**Three type of coincidences occurs from photon emission in PET; a) true coincidence, b) scatter coincidence, and; c) random coincidence. The solid blue line is the annihilation path and the dashed blue line represents the calculated LOR.**

### 1.2.3.3 PET Image reconstruction

The reconstruction of PET images from PET data involves two steps; first correcting for factors affecting the quantification of coincidences and second the transformation from digital signal to useful images. Only a brief description of each step will be described here, except for attenuation correction which has different root causes and techniques of correction, and therefore will be discussed separately.

#### 1.2.3.3.1 PET data correction

PET data from each LOR must be corrected for; 1- random and 2- scatter coincidences, 3- variation of detectors efficiencies, 4- count loss due to dead-time, and 5- attenuation of photons.

Correction of random coincidences may be reached by performing additional acquisition with a time delay to only one of the detected signals. The time delay violates the condition of detecting true coincidences and hence all detected coincidences in the additional acquisition are random, which can be determined, and then removed from the PET data.

Correction of scattering effect in PET systems has been addressed by different scatter correction models<sup>72-77</sup>, and found that quantitative accuracy of different type of scatter correction techniques did not have a significant impact on the quantitative results<sup>78</sup>. However, most used a model for scatter-correction that is based on an iterative reconstruction-based scatter compensation approach, which is suitable also for three-dimensional data<sup>76,79,80</sup>.

The variation of detector efficiencies causes variations in the image resolution and sensitivity. These can be corrected by means of normalization, which is described as, the number of detected coincidences by a pair of detectors in the data, divided by normalization factor of that pair of detectors<sup>81</sup>. The normalization factor is simply the ratio between the number of coincidences at each detector pair, from a uniform scan, and the average coincidences from all pairs.

Another type of correction that must be performed on when using PET detectors in pulse mode is the dead-time, which occurs due to loss of photon count. Since a finite time is

needed between two photon interactions to produce a signal, if the second photon interaction occur before the first photon interaction ends, the second photon is not counted.

The dead-time is normally addressed by applying either a paralyzable or non-paralyzable model. The paralyzable model assumes that a part of the data processing is performed on a fixed system clock, requiring a data buffering function (latch) to retain digital event information temporarily, and that input timing is random<sup>82</sup>. For the non-paralyzable the dead time is assumed to be non-extended and radiation events occurring during the detector dead times are not counted<sup>83</sup>.

#### 1.2.3.3.2 PET data transformation

The PET data provides the number of detected events along each LOR, which can be identified by both, its projection angle ( $\phi$ ), and the distance between the LOR and the center of the bore ( $r$ ). Therefore the projection lines are considered to be the integrals of events distribution over the entire LORs, and in 2D, all projections defined by the Radon transform  $p(r, \phi)$  and are known as sinogram<sup>84</sup>. For 3D PET data, reconstruction is usually completed by reconstructing an individual transaxial slice discretely using the same 2D reconstruction algorithms. There are two approaches of reconstruction algorithms; the analytical and the iterative approach. In the analytical approach, the algorithm inverse the Radon transform on the projection data, while in the iterative approach, the algorithm is adaptive to the imaging system performance, but requires impractical computing. Clinical scanners mostly use the iterative-based reconstruction, namely, Ordered Subsets Expectation Maximization (OSEM) model<sup>85</sup>, which is a modification of the Maximum Likelihood Expectation Maximization (MLEM)<sup>86</sup>. The OSEM algorithm reconstructs PET images rapidly with less noise.



#### 1.2.3.4 PET spatial resolution

Current PET systems can achieve spatial resolution in the range of 4-5mm full width half maximum (FWHM) across the line spread function in the center of the PET FOV<sup>87</sup>. The spatial resolution of the PET system depends on the spatial resolution of the detectors (detector width and depth), distance between the positron emission and the annihilation positions, and the imperfect collinearity of the two photons. If the detector is thick, the depth at which the gamma ray interacts with the crystal, cannot be estimated accurately, which results in an inaccurate estimation of the LOR angle. Consequently, the spatial resolution is at its highest at the center of the bore, and degrades closer to the bore walls. Additionally, in a PET system, a collimated pairs of detectors acts as electronic collimation, which makes PET a more sensitive modality, comparing to other nuclear medicine modalities<sup>69</sup>. However, this collimation also causes the PET to have low spatial resolution. The detection of the annihilation rather than the position of the positron emission also adds a limitation to spatial resolution for the PET system<sup>88</sup>. Even with the current spatial resolution of PET systems, its high sensitivity makes the spatial resolution acceptable.

#### 1.2.3.5 Photon attenuation

When annihilation occurs, each of the two photons must travel a certain distance through the material along LOR, known as the path length, before interacting with the detector. However, each photon travels a distance that is not necessarily equal, and therefore each photon has a unique distance to travel through the material, and is known as the partial path length. The partial path length depends on the positions of both the annihilation and the

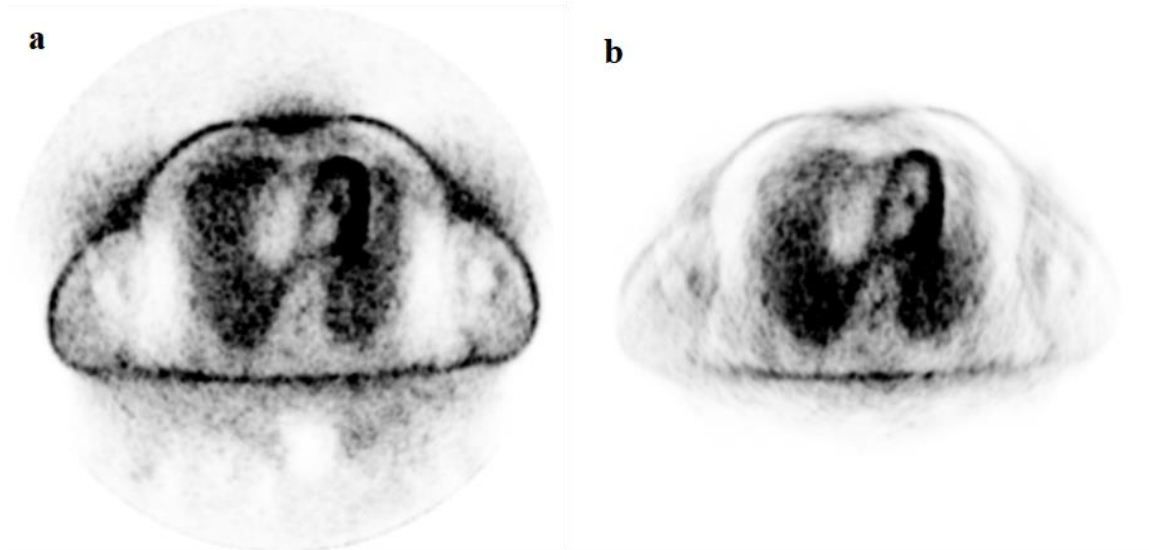
detector interacting with photon<sup>89</sup>. If one or two of the photons interacts with the material and loses its energy, no coincidence is registered and this is referred to as attenuation of photons<sup>90</sup>. Therefore, the probability of both photons being able to penetrate the material entirely, and reach two detectors in a straight line from each other, is the same as the probability of true coincidence. The vast majority of interaction between photons and material for human tissue at 511 keV are in the form of Compton scattering, which, if not corrected for in the image, will result in overestimation of activity distribution<sup>91</sup>. Compton scattering occurs when an emitted 511keV photon interacts with an electron resulting in a scattered photon with reduced energy and an electron with kinetic energy equal to the energy lost by the photon in the collision. The extent of energy loss by the photon depends on the scattering angle. The scattered photon from this interaction loses some of its kinetic energy and may travel through the medium and interact with another photon<sup>92</sup>. Compton scattering is dominant in the energy range 26 keV and 30 MeV for human tissues (low Z-number), and therefore for attenuation correction the Compton scattering must be accounted for<sup>93</sup>.

#### 1.2.3.6 Adverse-effect of attenuation on PET image.

Attenuation of photons means loss of energy information which varies along LORs, and causes higher background noise in the PET image which is called statistical noise. As seen in figure 1-11-a, attenuated image with no correction, namely, non-attenuation corrected (NAC) will have depression of activity concentration in the center and intensification of the image at the edges<sup>69,94</sup>, while figure 1-11-b is the same image but attenuation corrected

(AC) where homogeneity, localization of radioactivity and true counts improved in the overall image.

**Figure 1-11 Illustration of axial PET image of a patient a) non-attenuation corrected (NAC) and b) attenuation corrected (AC).**



Reconstruction of PET images without attenuation correction does not address the artifacts, and consequently prevents the qualitative interpretation of the image by a radiologist will result in inaccurate quantification of the radioactive concentration in the tissues<sup>95,96</sup>. In simple terms, the NAC image cannot be relied on for activity quantification and hence studying heart functions<sup>97</sup>.

### 1.2.3.7 Attenuation correction of 511 keV

#### 1.2.3.7.1 Attenuation coefficient

To overcome the photon attenuation effect, one must determine certain information in the image reconstruction process. Geometry, material atomic number and position are important information that can be used to provide a correction factor necessary for the

attenuation correction process. The attenuation of each material with an atomic number  $Z$  can be estimated from the emitted photons ( $I_0$ ) and detected photons ( $I$ ) through the material with thickness ( $d$ ). This is expressed in a general exponential relation as in eq. (6);

$$I = I_0 e^{-\mu d} \quad (6)$$

where  $\mu$  is the linear attenuation coefficient (LAC) of uniform material ( $Z$ ), measured in units of  $\text{cm}^{-1}$  unit, and is the sum of linear coefficients of each scatter type Compton, Rayleigh and photoelectric interaction. For 2D correction, the linear attenuation coefficients are arranged in a map of attenuation coefficients for a complex geometry and materials/tissues, known as a  $\mu$ -map. Thereafter, the  $\mu$ -map is used for correcting the NAC PET image from photon attenuation effects, during reconstruction. The information required to estimate a  $\mu$ -map is obtained through an independent process/technique from the process of diagnostic acquisition, and it is either conducted simultaneously or sequentially with the imaging acquisition.

#### 1.2.3.7.2 Attenuation correction $\mu$ -map

Common techniques used to generate the  $\mu$ -map for attenuation correction are; transmission scan-based attenuation map, CT-based attenuation map and the MRI-based attenuation map. The preferred technique depends on whether the PET system is part of a hybrid system, or is stand-alone.

##### 1.2.3.7.2.1 Transmission scan-based attenuation map

For stand-alone PET system, the source of information to generate the map is the PET system itself, and therefore a transmission scan approach is used, where a radioactive

source (usually  $^{68}\text{Ga}$ / $^{68}\text{Ge}$  or  $^{127}\text{Cs}$ ) acts as a positrons emitter. The transmission source is typically fitted between the patient and the detectors of the PET and rotates a complete circle ( $360^\circ$ ) around the patient to estimate the attenuation correction map for both human and hardware present in the PET FOV<sup>98-101</sup>.

#### 1.2.3.7.2.2 CT-based attenuation map

In the hybrid modalities PET/CT, the CT is used as the source of information to generate the  $\mu$ -map for both human and high density materials of the hardware, because the CT modality possesses a higher spatial and temporal resolution over the PET system, results in a more spatially accurate attenuation coefficient map<sup>30</sup>. The  $\mu$ -map is estimated by converting the Hounsfield units of the CT measurement into the attenuation coefficient of the material at 511keV<sup>102-105</sup>.

It is important to note that, both PET and PET/CT systems can provide the information needed for  $\mu$ -map creation, because both human tissues and hardware are visible to the x-ray and gamma-ray, which are provided by the transmission source or the x-ray tube (CT). However, in hybrid PET/MRI system, hardware is often invisible, for two reasons: 1- the MRI system typically provides information only for materials containing  $^1\text{H}$  nuclei with relaxation times in the range of those found in the human body; 2- the PET/MRI has no radioactive source built-in the system to provide information about objects in the FOV. Therefore, for PET/MRI hardware attenuation correction, CT-based attenuation correction maps have been primarily used to-date, and they are normally provided by the vendor of the system. The CT-based  $\mu$ -map can be achieved by several methods such as; Dual-energy decomposition<sup>82,106-109</sup>; scaling<sup>110</sup>; Segmentation<sup>111</sup>, or a hybrid between segmentation and scaling<sup>112</sup>.

#### 1.2.3.7.2.3 MRI-based attenuation correction

In PET/MRI, an attenuation coefficient maps are constructed for the human body through MRI acquisitions with specific pulse sequences<sup>113</sup>. However, the MRI image provides information on the tissue proton density rather than electron density. Therefore, the tissues' attenuation coefficient cannot be directly computed from MRI signal intensity. An example of this is where the air and compacta bone would show similar intensities on MRI, while their LAC differ widely. Therefore, the attenuation map of the human body obtained using MRI provides reliable information on the tissues well distinguished by MRI, such as fat and water. MRI-based separation of bone and air is still unreliable, which makes it a current topic of research<sup>114-118</sup>. The common/basic pulse sequences used for attenuation correction of the tissue are; 2-point Dixon volume interpolated breath-hold exam (Dixon-VIBE), homogenization using gradient enhancement (HUGE)<sup>119,120</sup>, and liver-accelerated volume acquisition (LAVA)-Flex sequence<sup>121</sup>. The most advanced pulse sequence recently developed to address bone is the ultra-short echo time (UTE) imaging sequence<sup>122,123</sup>, where the MRI FID signal is sampled less than 200 $\mu$ s after the radiofrequency excitation, to minimize the signal loss from the bone compartment (air remains MRI-invisible). Several sequences and techniques for MR-based estimates of human tissue attenuation are currently under study, but they will not be discussed here, as it is out of the scope of this thesis. The attenuation correction of the hardware in the PET/MRI system is discussed separately in section 1.2.3.7.3.

#### 1.2.3.7.2.4 Atlas attenuation correction

This AC techniques depends on pre-established anatomical information with their coefficients arranged into an atlas map, which can be spatially aligned to MRI data sets.

Atlas maps depends on selecting atlas that can be applied to wider patient population. Although the technique does not require generation of the  $\mu$ -map of the patient during PET imaging, the atlas approach assumes that attenuation coefficients are adequate in for the anatomy of all patient population<sup>124,125</sup>.

#### 1.2.3.7.3 PET/MRI Hardware attenuation correction

Any object present in the PET/MRI FOV during scanning is considered hardware, this includes; body Tx resonator of the MRI system (figure 1-3), inside the cover of the bore, headphones, eye tracking system, patient table, all RF receiver arrays (fixed/rigid and flexible) etc. Attenuation correction for both the inside cover of the bore and Tx body resonator are addressed by the vendor during reconstruction and few details are reported on them. On the other hand, mobile hardware such as headphones, can create up to a 13.2% decrease in activity concentration as determined in phantom studies modeling head imaging and hence, attenuation correction with CT-based  $\mu$ -map was proposed<sup>126,127</sup>. However, the issue with such mobile hardware (i.e. headphones and flexible arrays) AC, is that registration of their  $\mu$ -map to the PET image is often inaccurate. Although the effect of patient table attenuation is not covered in the literature, it is worth mentioning it here in this work, since it is the densest hardware in the PET/MRI system. For the patient table, a CT-based  $\mu$ -map for attenuation correction is also usually provided by the vendor, for which, to our knowledge, attempts to improve its attenuation map are rarely reported<sup>128</sup>. Beside the patient table, the RF receiver arrays used in cardiac imaging are of concern since they are considered to be one of the main causes of hardware attenuation, and they are the subject of ongoing research and development. The effect of receiver arrays on PET quantification is well covered in the literature, where it was reported to cause subtle

artifacts and produce quantification errors reaching 28%<sup>129-131</sup>. The RF receiver arrays can be grouped into two main groups, “rigid”, which are usually fixed arrays, and “flexible” which are usually mobile and deformable arrays.

#### 1.2.3.7.3.1 Fixed RF receiver array

Attenuation correction for fixed hardware including RF receiver arrays used in currently available commercial clinical PET/MRI systems are all performed using CT-based  $\mu$ -maps. The registration of the  $\mu$ -map of fixed and rigid hardware is straight-forward once the coordinates of the hardware are defined with respect to the PET/MRI coordinate system. The literature contains some examples of this such as, a fixed breast coil<sup>132</sup>, a fixed 31 channel head array<sup>133,134</sup> and a dual-tuned head resonator<sup>135</sup>. Although the registration is not an issue with fixed arrays, the CT-based  $\mu$ -map used for attenuation correction is systematically inaccurate. CT-based hardware attenuation maps tend to suffer from a beam hardening effect as described earlier (section 1.2.1.2), due to the presence of high-density and/or high Z-number materials found in housing materials and electronics components<sup>91,136</sup>.

#### 1.2.3.7.3.2 Flexible RF receiver array

Flexible arrays might seem light and harmless to PET quantification, yet even the least number of elements/channels (4 or 6 channels) can cause attenuation of up to 5.1%<sup>129,137,138</sup>. In a recent clinical cardiac study on 10 patients, using a flexible six channels surface RF array, it was reported an error of ~3%, when no attenuation correction was performed for the array<sup>139</sup>. In addition to the issue of inaccurate CT-based  $\mu$ -map, in general for PET/MRI hardware, accurate registration of the  $\mu$ -map in the case of flexible arrays is a great challenge. Several proposed solutions, to correct the photon attenuation



caused by flexible RF arrays used in cardiovascular PET/MRI imaging, has met with limited success. The first MR-based attenuation correction approach for flexible RF array used Cod liver oil capsules as fiducial markers and the UTE sequence for imaging<sup>137</sup>. This method addressed the registration rather than the high Z-number of the components included in the RF receiver array. Another study addressing the registration of  $\mu$ -map of flexible RF receiver arrays, incorporated an automatic algorithm to non-rigidly register a pre-acquired CT-based three-dimensional attenuation template of RF surface arrays to hardware attenuation maps used for PET AC<sup>140</sup>. Yet, this algorithm approach required a considerable amount of computing and resulted in quantification error of counts ranging from  $-3.9\%$  to  $4.3\%$ . Thereafter, a method to localize and register a CT-based attenuation  $\mu$ -map was reported, to correct for the attenuation and scatter of MRI-only, Flexible, 32-channel RF arrays used with \*MRI<sup>141</sup>. Although the registration accuracy was sufficient in that method, quantitative errors were observed when shifting the array attenuation  $\mu$ -map. The most recent study to address flexible RF receiver arrays, proposed to use a Microsoft Kinect V2 depth camera, where the camera determines the array geometry and creates a dense point cloud. The resulting array geometry is then registered to a pre-acquired CT-based  $\mu$ -map of the array during the AC process<sup>142</sup>. This proposed method claimed to achieve 1% errors in PET quantification, however, the method is limited to: availability of MR-compatible camera, extra space in the bore, complex and intense computation, all of which are currently impractical in clinical usage.

\* It is of note that 32-ch MRI-only coils are not used routinely by all clinical or research groups based on availability. Body matrix coils with lower number of channels are often used in lieu of 32-channel cardiac coils.

## 1.3 Hybrid PET/MRI imaging modalities

The obvious advantage of hybrid PET/MRI over hybrid PET/CT, is the lower radiation dose received by the patient. Additionally, while PET/CT suffers from limited contrast soft tissues, PET/MRI offers a multitude of contrasts amenable to soft tissue imaging such as diffusion-weighted imaging, dynamic contrast-enhanced imaging, fMRI as well as MR spectroscopy capabilities, to only name a few<sup>143</sup>. PET/MRI is also compatible with dual modality probes (multinuclear imaging)<sup>144</sup>. A whole-body PET/MRI system is a powerful hybrid of the PET and MRI modalities because it provides PET and MRI data sets with intrinsically perfect temporal and spatial registration. The enhanced soft tissues contrast of MRI is coupled to the sensitivity and quantitative abilities of PET.

### 1.3.1 Cardiovascular clinical applications

One of the major advantages of PET/MRI over PET/CT in cardiovascular studies, beside lowering the exposure to radiation dose, is the possibility of absolute quantification of myocardial blood flow using N-13 ammonia<sup>145</sup>, which potentially allows balanced ischemia in patients with three-vessel-disease to be unmasked. In the mean-time, early studies also demonstrated the high potential and success of PET/MRI as a diagnostic tool for myocarditis, and sarcoidosis<sup>18,20,146</sup>. Most recently, additional studies demonstrated that PET/MRI provides the soft tissue contrast that the gold-standard PET/CT cannot, which is useful in the diagnosis of a number of cardiac diseases<sup>21,23,147,148</sup>. The use of high-density phased array in cardiovascular PET/MRI studies can potentially improve the correction of respiratory and cardiac motion during the scan, where element sensitivity

profiles are used to collect information about the cardiac cycle faster than a 12-channels array<sup>149</sup>.

**Figure 1-12 Comparison between PET/MRI and PET/CT images using FDG radiotracer for a patient with cardiac sarcoid.**

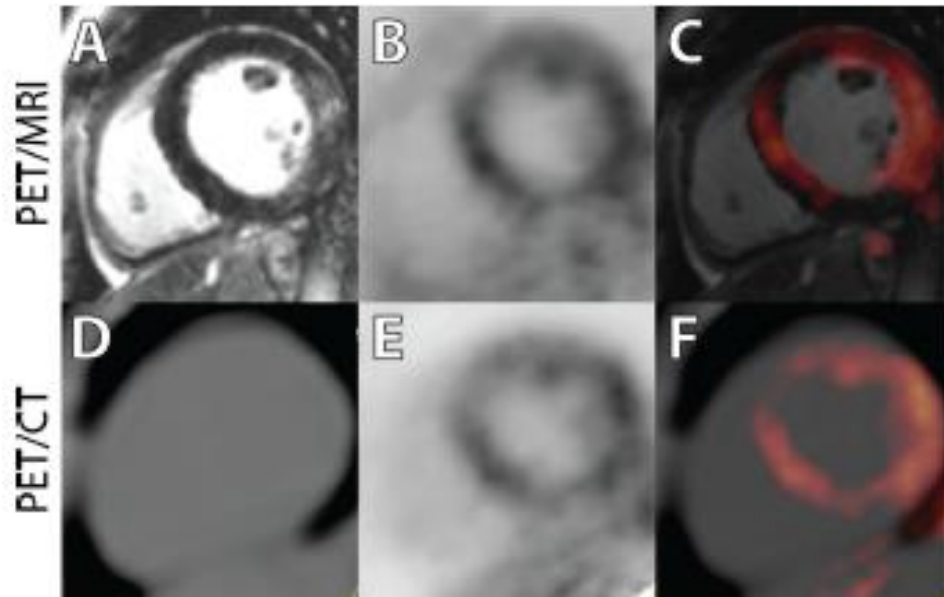


**Image is adapted with permission from reference<sup>21</sup>.**

### 1.3.2 Hybrid PET/MRI challenges

This section focuses only on PET quantification challenges resulting from operating the PET system hybridized with MRI, rather than as stand-alone PET quantification challenges.

#### 1.3.2.1 Accurate quantification of PET

Besides motion correction, PET quantification in the MRI environment depends mainly on how accurate the attenuation correction is, which also depends on the accuracy of both the attenuation coefficient and the AC-map registration. To achieve this, every source of

photon attenuation must be defined and its impact must be quantified and hence, solutions need to be provided to either minimize or eliminate the effect. Sources of attenuation such as hardware, bone-air segmentation, misregistration between the AC  $\mu$ -map and PET image and  $\mu$ -map truncation (i.e. arms) are all the subject of ongoing research. Both hardware AC and registration of the AC  $\mu$ -map to the PET image were described in section 1.2.3.7.3, and therefore, in the next section a brief description of other sources of attenuation is presented.

#### 1.3.2.1.1 Other sources of attenuation

In addition to the RF receiver arrays' attenuation as a source of inaccurate quantification, the presence of foreign objects<sup>150</sup> as well as a contrast agent used for image enhancement can result in quantification errors<sup>151</sup>.

#### 1.3.2.1.2 Motion

Random motion by the subject, respiratory motion, cardiac motion and blood flow, all are a source of inaccurate quantification of PET. Motion causes voxels in an image to have photon counts that do not belong to the same location in the imaged region over time, which directly affects PET quantification even before AC and AC to PET registration are performed. There is ongoing research where MRI information (from self navigated sequences), can address PET motion and correct for their effects<sup>152</sup>.

#### 1.3.2.1.3 Truncation

This is an issue, since the source of attenuation map of the human, must be derived from the MRI signal where MRI has limited FOV compared to PET. A recently developed algorithm that accounts for the truncated arms in the MRI-based  $\mu$ -map was developed and

is reasonably acceptable. It is based on a modified maximum likelihood reconstruction of attenuation and activity (MLAA)<sup>153,154</sup>. If a non-MRI-based AC  $\mu$ -map can be developed for object in the PET FOV, this source of artifact would be eliminated.

## 1.4 Thesis objectives

This chapter highlighted the need for improving the early diagnostic of cardiovascular diseases with reliable and fast tools, so that its associated mortality and cost, are reduced. The methods and tools including imaging modalities of cardiac diseases were briefly described, with emphasis on hybrid imaging modalities, specifically PET/MRI. Early use of the hybrid PET/MRI modalities in diagnosing cardiovascular diseases were discussed where promising results were shown. The advantages of using the hybrid PET/MRI modality, over other hybrid modalities, was presented in terms of soft tissue contrast and temporal and spatial resolution. Hardware needed to achieve temporal and spatial resolution known as RF phased receiver's array was explained, with their current statuses of being incapable of achieving desired resolutions, nor allowing accurate PET quantification. Recent research also has confirmed, that hybrid PET/MRI modality is urgently needed to attain accurate photon attenuation correction. Consequently, it is clear that to harness the full potential of the PET/MRI for diagnostics cardiovascular diseases, two fundamental goals must be reached hence, shaping the objectives of the thesis, and these are:

- 1- Achieving high temporal and spatial resolutions by enhancing the MRI modality part, and

- 2- Achieving accurate quantifications of PET activities enhancing the PET modality part.

While research on motion corrections, truncation and attenuation correction of human body are on-going, to minimize errors in PET quantification, this thesis is focused on the hardware contribution to the quantification error in PET.

Although there are arrays capable of providing excellent resolutions for the MRI-only modality, yet, they are unfit for the PET environment due to the unacceptable errors they cause in quantification of PET activity. Therefore, new prospectively-designed RF arrays for the hybrid PET/MRI are needed. Additionally, new approaches to produce accurate attenuation correction are also required, through accurate  $\mu$ -maps and registration. With this in mind, the following research questions have been identified:

- 1- Can high-density 32 channels RF array prospectively-designed for cardiovascular PET/MRI provide adequate MRI and PET performance?
- 2- Can the prospectively-designed multi receivers' RF array achieve acceleration factor of  $R > 2$  (temporal resolution) with better SNR (spatial resolution) than currently used in the PET/MRI array?
- 3- Can the prospectively-designed 32 channels RF array provide patient comfort and swift workflow?
- 4- Can the anterior part of the 32 channels RF phased array attenuate photons less than the current PET/MRI phased array (3%)?
- 5- Can the receivers' RF phased array, fully or partially, operate without attenuation correction  $\mu$ -map and hence be free of errors caused by misregistration?

- 6- If the prospectively-designed phased array still requires  $\mu$ -map to correct the attenuation, can a new approach of attenuation correction be developed and avoid the beam hardening artifacts, currently existing when using the CT modality?
- 7- Does the newly developed approach improve the PET quantification?
- 8- Can the novel approach to generate attenuation correction  $\mu$ -map be applied to other hardware such as patient table used in the PET/MRI system for better PET quantification?

Questions 1 and 2 are addressed in chapter 2, while questions 3 to 5 are addressed in chapter 3, and questions 6, 7 and 8 are addressed in chapter 4.

The research questions have been addressed in this thesis by focussing them down to three objectives:

- 1- To assess MRI performance of a novel prospectively-designed 32 channels RF phased array for hybrid PET/MRI cardiovascular imaging, and to compare this to currently used phased arrays.
- 2- To evaluate the photon attenuation at 511keV caused in the novel prospectively-designed 32 channels RF phased array for hybrid PET/MRI cardiovascular imaging and to compare currently used phased arrays with and without  $\mu$ -maps.
- 3- To develop a novel method to generate attenuation correction maps of hardware, used in hybrid PET/MRI modalities, without the need of CT and to assess its accuracy.

## 1.5 References

1. World Health Organization. Cardiovascular diseases report. 2018.
2. Statistics Canada. The ten leading causes of death, 2012. CANSIM (death database) [Internet]. Ottawa (ON): . In: Canada S, ed: Statistics Canada; 2015:Table 102-0561
3. Tarride J-E, Lim M, DesMeules M, et al. A review of the cost of cardiovascular disease. *Can J Cardiol.* 2009;25(6):e195-e202.
4. Benjamin EJ, Muntner P, Alonso A, et al. Heart Disease and Stroke Statistics&#x2014;2019 Update: A Report From the American Heart Association. *Circulation.* 2019;139(10):e56-e528.
5. Canadian Institute for Health Information. Inpatient Hospitalizations, Surgeries and Childbirth indicators in 2013–2014. In: Information CIH, ed. Canada: Canadian Institute for Health Information; 2015.
6. Go AS, Mozaffarian D, Roger VL, et al. Heart Disease and Stroke Statistics&#x2014;2013 Update. *Circulation.* 2013;127(1):e6-e245.
7. Heart and Stroke Foundation. Report on the health of Canadians; The burden of heart failure.: Heart and Stroke Foundation;2016.
8. Organization WH. Global atlas on cardiovascular disease prevention and control: published by the World Health Organization in collaboration with the World Heart Federation and the World Stroke Organization. 2011.
9. Waller AD. A Demonstration on Man of Electromotive Changes accompanying the Heart's Beat. *The Journal of Physiology.* 1887;8(5):229-234.



10. Beller GA, Zaret BL. Contributions of nuclear cardiology to diagnosis and prognosis of patients with coronary artery disease. *Circulation*. 2000;101(12):1465-1478.
11. Marwick T. Application of stress echocardiography to the evaluation of non-coronary heart disease. *European Journal of Echocardiography*. 2000;1(3):171-179.
12. Petersen SE, Khanji MY, Plein S, Lancellotti P, Bucciarelli-Ducci C. European Association of Cardiovascular Imaging expert consensus paper: a comprehensive review of cardiovascular magnetic resonance normal values of cardiac chamber size and aortic root in adults and recommendations for grading severity. *European Heart Journal-Cardiovascular Imaging*. 2019;20(12):1321-1331.
13. Group CCTW, Taylor AJ, Cerqueira M, et al. ACCF/SCCT/ACR/AHA/ASE/ASNC/NASCI/SCAI/SCMR 2010 appropriate use criteria for cardiac computed tomography: a report of the American college of cardiology foundation appropriate use criteria task force, the society of cardiovascular computed tomography, the American college of radiology, the American heart association, the American society of echocardiography, the American society of nuclear cardiology, the north American society for cardiovascular imaging, the society for cardiovascular angiography and interventions, and the society for cardiovascular magnetic resonance. *Circulation*. 2010;122(21):e525-e555.
14. Beyer T, Townsend DW, Brun T, et al. A combined PET/CT scanner for clinical oncology. *Journal of nuclear medicine*. 2000;41(8):1369-1379.
15. Kuhl DE, Edwards RQ. Reorganizing data from transverse section scans of the brain using digital processing. *Radiology*. 1968;91(5):975-983.

16. Heller GV, Calnon D, Dorbala S. Recent advances in cardiac PET and PET/CT myocardial perfusion imaging. *Journal of nuclear cardiology*. 2009;16(6):962.
17. Larsen JM, Ravkilde J. Acute coronary angiography in patients resuscitated from out-of-hospital cardiac arrest—a systematic review and meta-analysis. *Resuscitation*. 2012;83(12):1427-1433.
18. White JA, Rajchl M, Butler J, Thompson RT, Prato FS, Wisenberg G. Active Cardiac Sarcoidosis First Clinical Experience of Simultaneous Positron Emission Tomography–Magnetic Resonance Imaging for the Diagnosis of Cardiac Disease. *Circulation*. 2013;127(22):e639-e641.
19. Otton J, Morton G, Schuster A, et al. A direct comparison of the sensitivity of CT and MR cardiac perfusion using a myocardial perfusion phantom. *Journal of Cardiovascular Computed Tomography*. 2013;7(2):117-124.
20. Nensa F, Beiderwellen K, Heusch P, Wetter A. Clinical applications of PET/MRI: current status and future perspectives. *Diagnostic and Interventional Radiology*. 2014;20(5):438-447.
21. Wisenberg G, Thiessen J, Pavlovsky W, Butler J, Wilk B, Prato F. Same day comparison of PET/CT and PET/MR in patients with cardiac sarcoidosis. *Journal of Nuclear Cardiology*. 2019:1-12.
22. Ziegler S, Braun H, Ritt P, Hocke C, Kuwert T, Quick HH. Systematic Evaluation of Phantom Fluids for Simultaneous PET/MR Hybrid Imaging. *Journal of Nuclear Medicine*. 2013;54(8):1464-1471.
23. Lindemann ME, Nensa F, Quick HH. Impact of improved attenuation correction on 18F-FDG PET/MR hybrid imaging of the heart. *PLoS One*. 2019;14(3):e0214095.

24. Nensa F, Bamberg F, Rischpler C, et al. Hybrid cardiac imaging using PET/MRI: a joint position statement by the European Society of Cardiovascular Radiology (ESCR) and the European Association of Nuclear Medicine (EANM). *European Journal of Hybrid Imaging*. 2018;2(1):14.
25. Hope TA, Fayad ZA, Fowler KJ, et al. Summary of the First ISMRM–SNMMI Workshop on PET/MRI: Applications and Limitations. *Journal of Nuclear Medicine*. 2019;60(10):1340-1346.
26. van der Graaf AWM, Bhagirath P, Ghoerbien S, Götte MJW. Cardiac magnetic resonance imaging: artefacts for clinicians. *Neth Heart J*. 2014;22(12):542-549.
27. Hounsfield GN. Computerized transverse axial scanning (tomography): Part 1. Description of system. *The British journal of radiology*. 1973;46(552):1016-1022.
28. Bushberg JT, Boone JM. *The essential physics of medical imaging*. Lippincott Williams & Wilkins; 2011.
29. Li J, Jaszczak R, Greer K, Coleman R. A filtered backprojection algorithm for pinhole SPECT with a displaced centre of rotation. *Physics in Medicine & Biology*. 1994;39(1):165.
30. Lin E, Alessio A. What are the basic concepts of temporal, contrast, and spatial resolution in cardiac CT? *Journal of cardiovascular computed tomography*. 2009;3(6):403-408.
31. Barrett JF, Keat N. Artifacts in CT: recognition and avoidance. *Radiographics*. 2004;24(6):1679-1691.

32. Boas FE, Fleischmann D. CT artifacts: causes and reduction techniques. *Imaging in medicine*. 2012;4(2):229-240.
33. Kalender WA, Perman W, Vetter J, Klotz E. Evaluation of a prototype dual-energy computed tomographic apparatus. I. Phantom studies. *Medical physics*. 1986;13(3):334-339.
34. Vetter J, Perman W, Kalender WA, Mazess R, Holden J. Evaluation of a prototype dual-energy computed tomographic apparatus. II. Determination of vertebral bone mineral content. *Medical physics*. 1986;13(3):340-343.
35. Flohr TG, McCollough CH, Bruder H, et al. First performance evaluation of a dual-source CT (DSCT) system. *Eur Radiol*. 2006;16(2):256-268.
36. Xia T, Alessio AM, Kinahan PE. Dual energy CT for attenuation correction with PET/CT. *Medical physics*. 2014;41(1):012501.
37. Bamberg F, Dierks A, Nikolaou K, Reiser MF, Becker CR, Johnson TR. Metal artifact reduction by dual energy computed tomography using monoenergetic extrapolation. *Eur Radiol*. 2011;21(7):1424-1429.
38. Brenner DJ, Hall EJ. Computed tomography—an increasing source of radiation exposure. *New Engl J Med*. 2007;357(22):2277-2284.
39. Roemer P, Edelstein W, Hayes C, Souza S, Mueller O. The NMR phased array. *Magn Reson Med*. 1990;16(2):192-225.
40. Carlson JW. An algorithm for nmr imaging reconstruction based on multiple receivers coils. *J Magn Reson*. 1987;74:376-380.

41. Hutchinson M, Raff U. Fast MRI data acquisition using multiple detectors. *Magn Reson Med.* 1988;6(1):87-91.
42. Pruessmann KP, Weiger M, Scheidegger MB, Boesiger P. SENSE: Sensitivity encoding for fast MRI. *Magn Reson Med.* 1999;42(5):952-962.
43. Jakob PM, Grisowld MA, Edelman RR, Sodickson DK. AUTO-SMASH: a self-calibrating technique for SMASH imaging. *Magnetic Resonance Materials in Physics, Biology and Medicine.* 1998;7(1):42-54.
44. Sodickson DK, Manning WJ. Simultaneous acquisition of spatial harmonics (SMASH): fast imaging with radiofrequency coil arrays. *Magn Reson Med.* 1997;38(4):591-603.
45. Griswold MA, Jakob PM, Heidemann RM, et al. Generalized autocalibrating partially parallel acquisitions (GRAPPA). *Magn Reson Med.* 2002;47(6):1202-1210.
46. Lindemann ME, Guberina N, Wetter A, Fendler W, Jakoby B, Quick HH. Improving 68-Ga-PSMA PET/MR hybrid imaging of the prostate with unrenormalized absolute scatter correction. *Journal of Nuclear Medicine.* 2019.
47. Wang Y. Description of parallel imaging in MRI using multiple coils. *Magnetic Resonance in Medicine: An Official Journal of the International Society for Magnetic Resonance in Medicine.* 2000;44(3):495-499.
48. McGibney G, Smith M, Nichols S, Crawley A. Quantitative evaluation of several partial Fourier reconstruction algorithms used in MRI. *Magn Reson Med.* 1993;30(1):51-59.

49. Stenger VA, Noll DC, Boada FE. Partial Fourier reconstruction for three-dimensional gradient echo functional MRI: comparison of phase correction methods. *Magn Reson Med.* 1998;40(3):481-490.
50. Zhu Y, Hardy CJ, Sodickson DK, et al. Highly parallel volumetric imaging with a 32-element RF coil array. *Magn Reson Med.* 2004;52(4):869-877.
51. Hardy CJ, Dumoulin CL. Method and system for accelerated imaging using parallel MRI. In: Google Patents; 2005.
52. Hamilton J, Franson D, Seiberlich N. Recent advances in parallel imaging for MRI. *Progress in nuclear magnetic resonance spectroscopy.* 2017;101:71-95.
53. Weiger M, Pruessmann KP, Kassner A, et al. Contrast-enhanced 3D MRA using SENSE. *J Magn Reson Imaging.* 2000;12(5):671-677.
54. Kellman P, Zhang Q, Larson A, Simonetti O, McVeigh E, Arai A. Cardiac first-pass perfusion MRI using 3D trueFISP parallel imaging using TSENSE. 2004.
55. Griswold MA, Blaimer M, Heidemann RM, et al. Rapid evaluation of cardiac function using undersampled radial TrueFISP with GRAPPA. Paper presented at: Proceedings of the 12th Annual Meeting of the ISMRM2004.
56. Larkman DJ, Batchelor PG, Atkinson D, Rueckert D, Hajnal JV. Beyond the g-factor limit in sensitivity encoding using joint histogram entropy. *Magn Reson Med.* 2006;55(1):153-160.
57. Sodickson DK, Griswold MA, Jakob PM, Edelman RR, Manning WJ. Signal-to-noise ratio and signal-to-noise efficiency in SMASH imaging. *Magn Reson Med.* 1999;41(5):1009-1022.

58. Jianmin W, Reykowski A, Dickas J. Calculation of the signal-to-noise ratio for simple surface coils and arrays of coils [magnetic resonance imaging]. *IEEE Trans Biomed Eng.* 1995;42(9):908-917.
59. Constantinides CD, Westgate CR, O'Dell WG, Zerhouni EA, McVeigh ER. A phased array coil for human cardiac imaging. *Magn Reson Med.* 1995;34(1):92-98.
60. Reeder SB, Wintersperger BJ, Dietrich O, et al. Practical approaches to the evaluation of signal-to-noise ratio performance with parallel imaging: Application with cardiac imaging and a 32-channel cardiac coil. *Magn Reson Med.* 2005;54(3):748-754.
61. Schmitt M, Potthast A, Sosnovik DE, et al. A 128-channel receive-only cardiac coil for highly accelerated cardiac MRI at 3 Tesla. *Magn Reson Med.* 2008;59(6):1431-1439.
62. Hardy CJ, Giaquinto RO, Piel JE, et al. 128-channel body MRI with a flexible high-density receiver-coil array. *Journal of Magnetic Resonance Imaging: An Official Journal of the International Society for Magnetic Resonance in Medicine.* 2008;28(5):1219-1225.
63. Robson PM, Grant Ak Fau - Madhuranthakam AJ, Madhuranthakam Aj Fau - Lattanzi R, Lattanzi R Fau - Sodickson DK, Sodickson Dk Fau - McKenzie CA, McKenzie CA. Comprehensive quantification of signal-to-noise ratio and g-factor for image-based and k-space-based parallel imaging reconstructions. *Magn Reson Med.* 2008;60:895–907.
64. Constantinides CD, Atalar E, McVeigh ER. Signal-to-noise measurements in magnitude images from NMR phased arrays. *Magn Reson Med.* 1997;38(5):852-857.

65. Kellman P, McVeigh ER. Image reconstruction in SNR units: A general method for SNR measurement†. *Magn Reson Med*. 2005;54(6):1439-1447.
66. Glantz MJ, Hoffman JM, Coleman RE, et al. Identification of early recurrence of primary central nervous system tumors by [18F] fluorodeoxyglucose positron emission tomography. *Ann Neurol*. 1991;29(4):347-355.
67. Weber WA, Ziegler SI, Thodtmann R, Hanauske A-R, Schwaiger M. Reproducibility of metabolic measurements in malignant tumors using FDG PET. *The Journal of Nuclear Medicine*. 1999;40(11):1771.
68. Rigo P, Paulus P, Kaschten B, et al. Oncological applications of positron emission tomography with fluorine-18 fluorodeoxyglucose. *European journal of nuclear medicine*. 1996;23(12):1641-1674.
69. Ziegler SI. Positron emission tomography: principles, technology, and recent developments. *Nuclear Physics A*. 2005;752:679-687.
70. Breskin A. Photon detectors for the 21st century. *Nuclear Instruments and Methods in Physics Research Section A: Accelerators, Spectrometers, Detectors and Associated Equipment*. 1997;387(1-2):1-18.
71. Carrano J, Lambert D, Eiting C, et al. GaN avalanche photodiodes. *Applied Physics Letters*. 2000;76(7):924-926.
72. Links JM. Scattered Photons as “Good Counts Gone Bad:” Are They Reformable or Should They Be Permanently Removed from Society? In: *Soc Nuclear Med*; 1995.
73. Msaki P, Bentourkin M, Lecomte R. Scatter degradation and correction models for high-resolution PET. In: *Soc Nuclear Med*; 1996.



74. Grootenk S, Spinks T, Sashin D, Spyrou N, Jones T. Correction for scatter in 3D brain PET using a dual energy window method. *Physics in Medicine & Biology*. 1996;41(12):2757.
75. Levin CS, Dahlbom M, Hoffman EJ. A Monte Carlo correction for the effect of Compton scattering in 3-D PET brain imaging. *IEEE transactions on nuclear science*. 1995;42(4):1181-1185.
76. Watson CC, Newport D, Casey M, DeKemp R, Beanlands R, Schmand M. Evaluation of simulation-based scatter correction for 3-D PET cardiac imaging. *IEEE Transactions on Nuclear Science*. 1997;44(1):90-97.
77. Munley MT, Marks LB, Scarfone C, et al. Multimodality nuclear medicine imaging in three-dimensional radiation treatment planning for lung cancer: challenges and prospects. *Lung cancer*. 1999;23(2):105-114.
78. Zaidi H. Comparative evaluation of scatter correction techniques in 3D positron emission tomography. *European journal of nuclear medicine*. 2000;27(12):1813-1826.
79. Zaidi H. Scatter modelling and correction strategies in fully 3-D PET. *Nuclear medicine communications*. 2001;22(11):1181-1184.
80. Ollinger JM. Model-based scatter correction for fully 3D PET. *Physics in Medicine & Biology*. 1996;41(1):153.
81. Badawi RD, Marsden P. Developments in component-based normalization for 3D PET. *Physics in Medicine & Biology*. 1999;44(2):571.

82. Hasegawa T, Yoshida E, Yamaya T, Maruyama K, Murayama H. On-clock non-paralyzable count-loss model. *Physics in Medicine & Biology*. 2004;49(4):547.
83. Lee SH, Gardner RP, Jae M. Determination of dead times in the recently introduced hybrid GM counter dead time model. *Journal of Nuclear Science and Technology*. 2004;41(sup4):156-159.
84. Alessio A, Kinahan P. PET image reconstruction. *Nuclear medicine*. 2006;1:1-22.
85. Hudson HM, Larkin RS. Accelerated image reconstruction using ordered subsets of projection data. *IEEE Trans Med Imaging*. 1994;13(4):601-609.
86. Shepp LA, Vardi Y. Maximum likelihood reconstruction for emission tomography. *IEEE Trans Med Imaging*. 1982;1(2):113-122.
87. Delso G, Fürst S, Jakoby B, et al. Performance measurements of the Siemens mMR integrated whole-body PET/MR scanner. *Journal of nuclear medicine*. 2011;52(12):1914-1922.
88. Levin CS, Hoffman EJ. Calculation of positron range and its effect on the fundamental limit of positron emission tomography system spatial resolution. *Physics in Medicine & Biology*. 1999;44(3):781.
89. Bailey DL. Transmission scanning in emission tomography. *European Journal of Nuclear Medicine*. 1998;25(7):774-787.
90. Cherry S, Phelps M. Positron emission tomography: methods and instrumentation. *Diagnostic Nuclear Medicine 3rd ed Baltimore, MD: Williams & Wilkins*. 1996:139-159.

91. Zaidi H, Montandon M-L, Alavi A. Advances in attenuation correction techniques in PET. *PET clinics*. 2007;2(2):191-217.
92. Hubbell JH. Photon cross sections attenuation coefficients and energy absorption coefficients from 10keV to 100 GeV. *National Bureau of Standards*. 1969;1(NSRDS-NBS 29):80 p.
93. Christillin P. Nuclear Compton scattering. *Journal of Physics G: Nuclear Physics*. 1986;12(9):837.
94. Bengel FM, Ziegler SI, Avril N, Weber W, Laubenbacher C, Schwaiger M. Whole-body positron emission tomography in clinical oncology: comparison between attenuation-corrected and uncorrected images. *European journal of nuclear medicine*. 1997;24(9):1091-1098.
95. Huang S-C, Hoffman EJ, Phelps ME, Kuhl DE. Quantitation in positron emission computed tomography: 2. Effects of inaccurate attenuation correction. *J Comput Assisted Tomogr*. 1979;3(6):804-814.
96. Hustinx R, Dolin RJ, Bénard F, et al. Impact of attenuation correction on the accuracy of FDG-PET in patients with abdominal tumors: a free-response ROC analysis. *European journal of nuclear medicine*. 2000;27(9):1365-1371.
97. Bai C, Kinahan PE, Brasse D, et al. An analytic study of the effects of attenuation on tumor detection in whole-body PET oncology imaging. *Journal of Nuclear Medicine*. 2003;44(11):1855-1861.
98. Carroll LR, Kretz P, G. O. The orbiting rod source: improving performance in PET transmission correction scans. *New York: Society of Nuclear Medicine*. 1983(In: Esser PD, ed. Emission computed tomography – current trends.):235–247.

99. Stearns CW, Wack DC. A noise equivalent counts approach to transmission imaging and source design. *IEEE transactions on medical imaging*. 1993;12(2):287-292.
100. deKemp RA, Nahmias C. Attenuation correction in PET using single photon transmission measurement. *Medical physics*. 1994;21(6):771-778.
101. Bailey DL, Jones T. A method for calibrating 3D PET without scatter correction. Paper presented at: 1995 IEEE Nuclear Science Symposium and Medical Imaging Conference Record; 21-28 Oct. 1995, 1995.
102. Beyer T, Kinahan PE, Townsend DW, Sashin D. The use of X-ray CT for attenuation correction of PET data. Paper presented at: Proceedings of 1994 IEEE Nuclear Science Symposium - NSS'94; 30 Oct.-5 Nov. 1994, 1994.
103. Burger C, Goerres G, Schoenes S, Buck A, Lonn A, von Schulthess G. PET attenuation coefficients from CT images: experimental evaluation of the transformation of CT into PET 511-keV attenuation coefficients. *Eur J Nucl Med Mol Imag*. 2002;29(7):922-927.
104. Carney JP, Townsend Dw Fau - Rappoport V, Rappoport V Fau - Bendriem B, Bendriem B. Method for transforming CT images for attenuation correction in PET/CT imaging. *American Association of Physicists in Medicine*. 2006;33(4):976-983.
105. Chuanyong B, Ling S, Silva AJD, Zuo Z. A generalized model for the conversion from CT numbers to linear attenuation coefficients. *IEEE Transactions on Nuclear Science*. 2003;50(5):1510-1515.

106. Patrick JC, Terry Thompson R, So A, et al. Technical Note: Comparison of megavoltage, dual-energy, and single-energy CT-based  $\mu$ -maps for a four-channel breast coil in PET/MRI. *Medical physics*. 2017;44(9):4758-4765.
107. Guy MJ, Castellano-Smith IA, Flower MA, Flux GD, Ott RJ, Visvikis D. DETECT-dual energy transmission estimation CT-for improved attenuation correction in SPECT and PET. *IEEE Transactions on Nuclear Science*. 1998;45(3):1261-1267.
108. Kinahan PE, Alessio AM, Fessler JA. Dual Energy CT Attenuation Correction Methods for Quantitative Assessment of Response to Cancer Therapy with PET/CT Imaging. *Technology in Cancer Research & Treatment*. 2006;5(4):319-327.
109. Berger M, Hubbell J, Seltzer S, et al. XCOM: Photon cross sections database (NBSIR 87-3597). *National Institute of Standards and Technology, Washington DC*. 1998.
110. Blankespoor S, Xu X, Kaiki K, et al. Attenuation correction of SPECT using X-ray CT on an emission-transmission CT system: myocardial perfusion assessment. *IEEE Transactions on Nuclear Science*. 1996;43(4):2263-2274.
111. Carney J, Beyer T, Brasse D, Yap JT, Townsend DW. CT-based attenuation correction for PET/CT scanners in the presence of contrast agent. Paper presented at: 2002 IEEE Nuclear Science Symposium Conference Record2002.
112. Kinahan PE, Townsend DW, Beyer T, Sashin D. Attenuation correction for a combined 3D PET/CT scanner. *Medical physics*. 1998;25(10):2046-2053.
113. Park CR, Lee Y. Comparison of PET image quality using simultaneous PET/MR by attenuation correction with various MR pulse sequences. *Nuclear Engineering and Technology*. 2019.

114. Pichler BJ, Wehrl HF, Kolb A, Judenhofer MS. Positron Emission Tomography/Magnetic Resonance Imaging: The Next Generation of Multimodality Imaging? *Semin Nucl Med.* 2008;38(3):199-208.
115. Herzog H, Van Den Hoff J. Combined PET/MR systems: an overview and comparison of currently available options. *Q J Nucl Med M.* 2012;56(3):247-267.
116. Catana C, Drzezga A Fau - Heiss W-D, Heiss Wd Fau - Rosen BR, Rosen BR. PET/MRI for neurologic applications. *Journal of Nuclear Medicine.* 2012;53(1916–1925).
117. Catana C. Attenuation correction for human PET/MRI studies. *Physics in Medicine & Biology.* 2020.
118. Ladefoged CN, Law I, Anazodo U, et al. A multi-centre evaluation of eleven clinically feasible brain PET/MRI attenuation correction techniques using a large cohort of patients. *NeuroImage.* 2017;147:346-359.
119. Blumhagen JO, Ladebeck R, Fenchel M, Scheffler K. MR-based field-of-view extension in MR/PET: B0 homogenization using gradient enhancement (HUGE). *Magn Reson Med.* 2013;70(4):1047-1057.
120. Lindemann ME, Oehmigen M, Blumhagen JO, Gratz M, Quick HH. MR-based truncation and attenuation correction in integrated PET/MR hybrid imaging using HUGE with continuous table motion. *Medical physics.* 2017;44(9):4559-4572.
121. Reiner CS, Stolzmann P, Husmann L, et al. Protocol requirements and diagnostic value of PET/MR imaging for liver metastasis detection. *Eur J Nucl Med Mol Imag.* 2014;41(4):649-658.

122. Reichert IL, Robson MD, Gatehouse PD, et al. Magnetic resonance imaging of cortical bone with ultrashort TE pulse sequences. *Magn Reson Imaging*. 2005;23(5):611-618.
123. Keereman V, Fierens Y, Broux T, De Deene Y, Lonneux M, Vandenberghe S. MRI-based attenuation correction for PET/MRI using ultrashort echo time sequences. *Journal of nuclear medicine*. 2010;51(5):812-818.
124. Zaidi H, Hasegawa B. Determination of the attenuation map in emission tomography. *Journal of Nuclear Medicine*. 2003;44(2):291-315.
125. Defrise M, Rezaei A, Nuyts J. Transmission-less attenuation correction in time-of-flight PET: analysis of a discrete iterative algorithm. *Physics in medicine and biology*. 2014;59(4):1073.
126. Ferguson A. JM, YiSu, Debra Hewing, and Richard Laforest. Attenuation Effects of MR Headphones During Brain PET/MR Studies. *Journal of Nuclear Medicine Technology*. 2014;42:93–100.
127. Mantlik F, Hofmann M, Werner MK, et al. The effect of patient positioning aids on PET quantification in PET/MR imaging. *Eur J Nucl Med Mol Imag*. 2011;38(5):920-929.
128. Xie H, Zhao J, Dong Y, Lv Y. Attenuation Correction for Fixed MR Components in a Simultaneous PET/MR System. Paper presented at: 2017 IEEE Nuclear Science Symposium and Medical Imaging Conference (NSS/MIC); 21-28 Oct. 2017, 2017.
129. Tellmann L, Quick H, Bockisch A, Herzog H, Beyer T. The effect of MR surface coils on PET quantification in whole-body PET/MR: results from a pseudo-PET/MR phantom study. *Medical physics*. 2011;38(5):2795-2805.

130. MacDonald LR, Kohlmyer S, Liu C, Lewellen TK, Kinahan PE. Effects of MR surface coils on PET quantification. *Medical physics*. 2011;38(6):2948-2956.
131. Wollenweber S, Delso G, Deller T, Goldhaber D, Hüllner M, Veit-Haibach P. Characterization of the impact to PET quantification and image quality of an anterior array surface coil for PET/MR imaging. *Magnetic Resonance Materials in Physics, Biology and Medicine*. 2014;27(2):149-159.
132. Dregely I, Lanz T, Metz S, et al. A 16-channel MR coil for simultaneous PET/MR imaging in breast cancer. *European Society of Radiology*. 2014;25:1154–1161.
133. Sander CY, Keil B, Chonde DB, Rosen BR, Catana C, Wald LL. A 31-channel MR brain array coil compatible with positron emission tomography. *Magn Reson Med*. 2014;73(6):2363-2375.
134. Anazodo UC, Farag A, Theberge J, et al. Assessment of PET performance of a 32-Channel MR Brain Array Head Coil Compatible with PET for Integrated PET-MRI. Paper presented at: PSMR; May 23rd – 25th 2016; Cologne / Germany.
135. Oehmigen M, Lindemann ME, Gratz M, et al. A dual-tuned (13) C/(1) H head coil for PET/MR hybrid neuroimaging: Development, attenuation correction, and first evaluation. *Medical physics*. 2018;45(11):4877-4887.
136. Alles J, Mudde R. Beam hardening: Analytical considerations of the effective attenuation coefficient of x-ray tomography. *Medical physics*. 2007;34(7):2882-2889.
137. Paulus DH, Braun H, Aklan B, Quick HH. Simultaneous PET/MR imaging: MR-based attenuation correction of local radiofrequency surface coils. *Medical physics*. 2012;39(7):4306-4315.



138. Fürst S, Souvatzoglou M, Martinez-Möller A, Nekolla S, Schwaiger M, Ziegler S. Impact of MRI surface coils on quantification in integrated PET/MR. *The Journal of Nuclear Medicine*. 2012;53(supplement 1):436.
139. Lau JM, Laforest R, Sotoudeh H, et al. Evaluation of attenuation correction in cardiac PET using PET/MR. *Journal of Nuclear Cardiology*. 2017;24(3):839-846.
140. Kartmann R, Paulus DH, Braun H, et al. Integrated PET/MR imaging: Automatic attenuation correction of flexible RF coils. *Medical physics*. 2013;40(8):082301.
141. Eldib M, Bini J, Calcagno C, Robson PM, Mani V, Fayad ZA. Attenuation Correction for Flexible Magnetic Resonance Coils in Combined Magnetic Resonance/Positron Emission Tomography Imaging. *Investigative radiology*. 2014;49(2):63-69.
142. Frohwein LJ, Heß M, Schlicher D, et al. PET attenuation correction for flexible MRI surface coils in hybrid PET/MRI using a 3D depth camera. *Physics in Medicine & Biology*. 2018;63(2):025033.
143. Ehman EC, Johnson GB, Villanueva-Meyer JE, et al. PET/MRI: where might it replace PET/CT? *J Magn Reson Imaging*. 2017;46(5):1247-1262.
144. Fox MS, Farag A, Akbari A, Scholl TJ, Thompson T, Thiessen JD. Simultaneous X-Nuclei MRI and PET using <sup>23</sup>Na and <sup>18</sup>F-FDG. Paper presented at: The World Molecular Imaging Congress (WMIC)2018.
145. Yang H-J, Oksuz I, Dey D, et al. Accurate needle-free assessment of myocardial oxygenation for ischemic heart disease in canines using magnetic resonance imaging. *Science translational medicine*. 2019;11(494).

146. Nensa F, Poeppel TD, Beiderwellen K, et al. Hybrid PET/MR imaging of the heart: feasibility and initial results. *Radiology*. 2013;268(2):366-373.
147. Wilk B, Wisenberg G, Dharmakumar R, Thiessen JD, Goldhawk DE, Prato FS. Hybrid PET/MR imaging in myocardial inflammation post-myocardial infarction. *Journal of Nuclear Cardiology*. 2019.
148. Chen W, Jeudy J. Assessment of Myocarditis: Cardiac MR, PET/CT, or PET/MR? *Current cardiology reports*. 2019;21(8):76.
149. Han F, Rapacchi S, Hu P. Prospective cardiac motion self-gating. *Quantitative imaging in medicine and surgery*. 2017;7(2):215
150. Hargreaves BA, Worters PW, Pauly KB, Pauly JM, Koch KM, Gold GE. Metal-induced artifacts in MRI. *Am J Roentgenol*. 2011;197(3):547-555.
151. Muehe AM, Yerneni K, Theruvath AJ, et al. Ferumoxytol Does Not Impact Standardized Uptake Values on PET/MR Scans. *Mol Imag Biol*. 2019:1-8.
152. Munoz C, Neji R, Cruz G, et al. Motion-corrected simultaneous cardiac positron emission tomography and coronary MR angiography with high acquisition efficiency. *Magn Reson Med*. 2018;79(1):339-350.
153. Nuyts J, Dupont P, Stroobants S, Benninck R, Mortelmans L, Suetens P. Simultaneous maximum a posteriori reconstruction of attenuation and activity distributions from emission sinograms. *IEEE Trans Med Imaging*. 1999;18(5):393-403.
154. Nuyts J, Bal G, Kehren F, Fenchel M, Michel C, Watson C. Completion of a truncated attenuation image from the attenuated PET emission data. *IEEE Trans Med Imaging*. 2012;32(2):237-246.

## Chapter 2

### 2 Assessment of a Novel 32-Channel Phased Array for Cardiovascular Hybrid PET/MRI Imaging: MRI performance

#### 2.1 Introduction

Hybrid imaging systems combining positron emission tomography (PET) and magnetic resonance imaging (MRI), namely PET/MRI scanners, are unique in providing both functional and intrinsically-registered anatomical information from both PET and MRI simultaneously. PET/MRI systems are therefore highly advantageous for multimodality studies, which can improve the characterization and grading of metabolically active tumors using  $^{18}\text{F}$ -fluoro-deoxy-glucose (FDG)<sup>1,2</sup>, while superimposing such activity on anatomical images with the superior soft-tissue contrast of MRI to identify active inflammation<sup>3</sup>. In addition, by combining perfusion tracers such as  $^{13}\text{N}$ -labeled-Ammonia ( $^{13}\text{NH}_3$ ) with FDG, the PET/MRI has also been shown to be successful in cardiovascular imaging where left/right ventricular function and myocardial perfusion and blood flow in surrounding vessels of the heart can be quantified<sup>4-6</sup>.

Since the emergence of whole-body PET/MRI systems, several technical challenges have been identified and commonly reported around the accurate quantification of the 511 keV annihilation photons detected in PET images<sup>7-9</sup>. The greatest challenge, apart from respiratory and cardiac motion, is the accurate correction of PET counts due to attenuation within materials located between the radioactive source and the PET detectors. Attenuation

of 511 keV photons is caused by the presence of the patient body (tissues, air cavities, blood and bones) and the scanner hardware in the PET field-of-view (FOV). Hardware, such as the patient bed, audio communication system and radio frequency (RF) resonators have the most attenuating effect and cause scattering or simply block the gamma rays from reaching the PET detectors<sup>10-12</sup>. However, RF phased arrays are crucial for MRI parallel imaging as they achieve the shortest scan time with the highest spatial and temporal resolutions, and their use, particularly for cardiovascular MRI, is an essential part of the standard of care. The advantage of parallel imaging with high acceleration factor up to 4 in one-dimension for cardiac MRI was proven to be beneficial for imaging<sup>13</sup>. Therefore, a phased array with 32-channels is highly desired. Although a few dedicated PET/MRI RF phased arrays have been developed for brain<sup>14-16</sup> and breast<sup>17</sup> imaging, no phased array, to our knowledge, has been developed for PET/MRI cardiovascular imaging. Currently, MRI-only research systems offer phased arrays with up to 128-channels for cardiovascular imaging<sup>18</sup>, while clinical PET/MRI systems offer up to 12-channels. Although commercially available, PET/MRI arrays are typically restricted to a lower number of channels to reduce attenuation of gamma rays. Nevertheless, PET/MRI arrays have been reported to cause variation of the standardised uptake value (SUV) ranging from 18% to 60% closer to the array, if the attenuation correction (AC) is not included during the PET image reconstruction<sup>19-21</sup>.

Meanwhile, developing a dedicated PET/MRI phased array with a higher number of channels is technically challenging, leading researchers to focus on the approach of correcting the attenuation of the currently available MRI arrays<sup>12,22-24</sup>. The common approach to correct for attenuation of an RF phased array is to generate a hardware AC

map, also known as a  $\mu$ -map, produced from a CT scan at a specific tube voltage<sup>25,26</sup>. The process of generating a hardware-AC map is normally conducted by the scanner manufacturers for all vendor-provided hardware, prior to delivery of the scanner. AC maps are accurately included during PET image reconstruction for fixed rigid hardware, such as the patient table and rigid RF arrays. For more accurate AC of flexible RF arrays, fiducial markers can be added to guide the registration of the hardware AC map with the PET image

12.

Although, RF arrays with a lower number of channels are adequate for most oncologic applications, simultaneous PET/MRI for cardiovascular imaging can still benefit from faster parallel-imaging using a dedicated PET/MRI RF 32-channel phased array prospectively designed for minimal PET attenuation. It is, therefore, important to investigate alternative approaches to minimize the attenuation caused by a high-density phased array for cardiovascular PET/MRI imaging. In this work we evaluate the third-party dedicated 32-channel phased array (developed by a local company) optimised for parallel imaging of the heart with PET/MRI. The quality parameters for parallel imaging, such as the geometry factor (g-factor), SNR and noise correlation coefficients, are compared to the two commercially available and currently used, MRI-only 32-channel and the PET/MRI 12-channel arrays.

The reduction in PET signal due to attenuation caused by the candidate array was briefly examined and reported. Although this work focusses on the MRI performance of the array, the equally important PET performance of the candidate array will be compared in detail to the existing arrays and will be reported in a separate manuscript. Only a cursory evaluation of PET performance will be reported herein. We hypothesize that if the MRI

quality parameters of the PET/MRI 32-channel array are similar with those produced by MRI-only 32-channel array, and if global gamma ray attenuation of the PET/MRI 32-channel array is less than that of the mMR 12-channel array, the MRI performance of the PET/MRI 32-channel array would be acceptable for hybrid/simultaneous PET/MRI cardiovascular imaging.

## 2.2 Methods and Materials

### 2.2.1 Description of the arrays

The PET/MRI phased array consists of two parts; a posterior and an anterior, allowing the patient to be scanned in head-first, supine position. The RF elements were arranged to cover the entire heart region and can be connected to the scanner at four ports. The ports are arranged, with two ports for the anterior array, and two ports for the posterior array, allowing each part of the array to be used independently. The anterior and posterior part of the 32-channel arrays have sixteen elements each, arranged in a 4x4 fashion to maximize acceleration factor in directions within the coronal plane. The flexible body mMR 6-channel array (Siemens Healthcare Limited, Erlangen, Germany) elements are arranged in 3x2 fashion, which is similar in arrangement to the spine matrix array (Siemens Healthcare Limited, Erlangen, Germany). Therefore, the flexible body mMR 6-channel array was combined with six elements from the posterior spine matrix mMR array formulating a set of mMR 12-channel array used in this work.

In this study, a commercially available cardiac MRI-only 32-channel array (In-Vivo Corporation, Gainesville, FL, USA) was used, while the prototype novel PET/MRI 32-channel was provided for assessment by a local company (Ceresensa. Inc, Canada 2016).

**Figure 2-1 Phantom experiment setup for the three arrays during MRI measurements.**



**The experiment setup for the three arrays PET/MRI 32-channel, MRI-only 32-channel, and mMR 12-channel. Position of isocenter were kept unchanged from one acquisition to the other.**

### 2.2.2 MRI Phantom imaging

For this study, a balanced steady-state free precession (balanced-SSFP or TrueFISP in vendor's nomenclature) pulse technique was selected due to its ability to acquire sub-second scan time per slice and its sensitivity to high fluid-tissue contrast<sup>27</sup>. All MRI acquisitions were performed on a 3.0T PET/MRI system (Biograph mMR Software Version VE11P, Siemens Healthineers, Erlangen, Germany).

All three arrays operated with posterior and anterior parts, making the condition of the measurements identical as seen in Figure 1. Phantom imaging data were acquired using a standard cylindrical acrylic container (OD = 28cm) filled with a solution of both

NiSO<sub>4</sub>·6(H<sub>2</sub>O) and NaCl in distilled water. To mimic the location of the heart in a patient, the distance between the anterior and posterior array elements were kept to approximately 27cm and the 12cm high cylindrical phantom was centred between them, leaving the elements approximately 7.5cm away from the surface of the phantom. To examine the parallel imaging capabilities of each array, a single 2D-slice at the center of the phantom in the coronal plane was acquired using the manufacturer's 2D TrueFISP sequence. Multiple acquisitions were performed with phase encoding in left-right (LR) direction, for different acceleration factors ranging from  $R=1$  to  $R=6$ . A second set of acquisitions similar to the above was performed, changing the phase encoding into the foot-head (FH) direction, for the same number of acceleration factors. The image reconstruction utilised the generalized autocalibration partially parallel acquisitions (GRAPPA) technique<sup>28</sup>, with 64 reference lines for all accelerations. The 2D TrueFISP-GRAPPA parameters for the LR and FH encoding were: BW = 440 Hz/pixel, FOV = 253 x 253mm, spatial resolution of 1.3 x 1.3 x 8.0 mm<sup>3</sup>, flip angle = 50°, and TE/TR = 2.40/4.79ms. For each acceleration factor  $R$ , noise data was also acquired with the same parameters except the RF amplitude was set to zero. The above two sets of coronal acquisitions were repeated two times on the phantom for each array, with a total of 64 acquisitions for each array.

A reflected power test was performed to ensure that there is no undue change to the RF field transmitted by the integrated body resonator due to poor decoupling from the receiver array<sup>18</sup>. A low percent difference in reference voltage between the “with-array” and “no-array” conditions indicates that no undue amount of transmitted energy is absorbed within the receiver array. The reference voltage was determined by the scanner's automated RF calibration procedure and represents the voltage necessary to obtain a 180° flip angle using



a 1ms square RF pulse. This test was performed only on the PET/MRI 32-channel array, since it is not licensed or approved by a third-body regulator.

### 2.2.3 In-Vivo Imaging

For in-vivo imaging, acquisitions were performed on three healthy volunteers, recruited with written informed consent according to a research ethics protocol approved by the Research Ethics Board (protocol ID 6319). In addition to the same pulse sequences that were performed in the phantom acquisitions, ECG-triggered 2D TrueFISP cine images were acquired on a single breath-hold with axial double-oblique orientation and a 4-chamber view of the heart. The imaging parameters of the cine MRI with activated GRAPPA for  $R = 2$  (anterior-posterior phase encoding) were: TE/TR = 1.58/36.3 ms; 25 segments; spatial resolution of  $1.0 \times 1.4 \times 6.0 \text{ mm}^3$ ; FOV = 253 x 300mm; flip angle =  $50^\circ$ ; and BW =  $930 \pm 16 \text{ Hz/pixel}$ . For the three volunteers the average beat-to-beat interval was  $906 \pm 50 \text{ ms}$ . Each volunteer was fitted with MRI-compatible ECG electrodes, so that the data is retrospectively ECG-gated. Volunteers were imaged in the head-first supine position, with a total acquisition time of under 10 seconds in 13 heart beats. Each volunteer was imaged consecutively with all three arrays under the same conditions and using the same imaging parameters as described above. The full duration of an imaging session for one volunteer with the three arrays was under 60 minutes.

### 2.2.4 Data processing and analysis

For phased arrays, SNR is more likely to be overestimated if measured from the magnitude of the image, due to bias of the Rician-distributed noise in the magnitude image<sup>29,30</sup>. The noise measured by a phased array is influenced by the overlapping of each element and

cannot be treated as a single source of noise, i.e. a fraction of the noise observed by each element is correlated noise and must be accounted for via noise correlation coefficient to avoid overestimation. Notably, the mMR 12-channel array utilises OEM-specified combiner chip, while both MRI-only and PET/MRI arrays do not. Therefore, using raw data (k-space) for signal and noise was necessary to perform appropriate and fair comparison and identical reconstruction. Two techniques were introduced<sup>30,31</sup>, by which SNR of phased arrays can be estimated in a pixel-by-pixel fashion. Both techniques have addressed the geometric overlapping of array elements (known as g-factor). In this work, the g-factor was computed from both the estimated noise covariance, which was computed from noise correlation coefficients of the array elements in Appendix A (Pruessmann et al., 1999), and sensitivity map (spatial element sensitivity) which was estimated off-line. The formulas used to compute sensitivity, g-factor and SNR parameters are described by equations [1], [2] and [3] in<sup>30</sup>, and presented here for convenience.

$$\mathbf{S}_{pj} = \mathbf{S}_j * \mathbf{r}_p \quad [1]$$

$$\mathbf{g}_p = \sqrt{((\mathbf{S}^H \boldsymbol{\Psi}^{-1} \mathbf{S})^{-1})_{p,p} (\mathbf{S}^H \boldsymbol{\Psi}^{-1} \mathbf{S})_{p,p}} \quad [2]$$

$$\mathbf{SNR}_g = \frac{\mathbf{SNR}_0}{\mathbf{g}_p \sqrt{R}} \quad [3]$$

Where  $\mathbf{S}$  is the complex sensitivity matrix,  $\Psi$  the noise correlation coefficient,  $\mathbf{r}$  is the aliased  $\mathbf{p}$  pixel position and  $\mathbf{j}$  is the array element number. The g-factor-based  $\text{SNR}_g$  was estimated on a pixel-by-pixel fashion for multiple acceleration factors  $R=2$  to  $R=6$  from the fully sampled image  $\text{SNR}_0$ , which was found by the difference method<sup>32</sup>.

For the two phantom experiments, global mean, from masked images, and standard deviation (SD) of the  $\text{SNR}_0$ ,  $\text{SNR}_g$ , and, g-factor were calculated at each  $R$  value independently for both 1-dimension (phase encoding LR or FH) and 2-dimensions (phase encoding is in both LR and FH). The relationship between mean  $\text{SNR}_g$  and inverse g-factor as functions of  $R$  were examined and compared for the three arrays. Mean and SD of the noise correlation coefficients were estimated excluding the self-correlated coefficients (diagonal values of the matrix). The percentage difference of the quality parameters for the MRI-only and PET/MRI 32-channel arrays were estimated using equation [4], where  $v_1$  is the PET/MRI array parameter value and  $v_2$  is the MRI-only array parameter value. For the interpretation of the percentage difference, a criterion was established in which the absolute function in the formula was ignored allowing directional estimates. Instead, the measured parameters for the MRI-only array were subtracted from those of the PET/MRI array. Hence, a negative percentage difference would indicate a better performance of the PET/MRI array for the g-factor parameter. All quality parameters of the parallel imaging and data analysis for each array were computed using Matlab 9.3.0 (The MathWorks, Natick, MA, USA).

$$\% \textit{ difference} = \frac{v_1 - v_2}{0.5 (v_1 + v_2)} 100\% \quad [4]$$

### 2.2.5 PET activity test

To estimate PET photon attenuation, 2-point Dixon acquisitions were performed prior to the PET acquisition, with and without the array, on the mMR Ge-68 Daily Quality Control (QC) phantom (Siemens, Healthineers, Erlangen, Germany). The Dixon acquisition consisted of a 3D dual-echo spoiled gradient sequence with the following parameters: TE/TR = 1.23/3.96 ms; slice thickness = 3.1mm; flip angle = 9° and FOV = 312 x 500 mm. The phantom was mounted following the procedure used in the daily QC, where neither the patient table nor array were present in the bore of the PET/MRI system during the Dixon acquisition. An 8 mins PET acquisition was carried out immediately after the Dixon while the array was placed around the phantom. Placing the array took no more than 2 min, therefore, only the last 6 mins of the data were used for PET image reconstruction. The resultant data was labelled as “no-array, no-table” and was used as a base line to compare to PET/MRI array. The same acquisitions were repeated on the phantom but with the array’s anterior part placed on the top of the QC phantom, while the array’s posterior part was placed below the QC phantom. Mean of PET counts per seconds (CPS) from the acquisitions, without applying AC maps, were estimated from the central transaxial slice of the phantom for each PET acquisition.

## 2.3 Results

The voltage recorded for 180° RF pulse with the volunteer in the scanner, but without the PET/MRI 32-channel array, was 562 V. It was 598 V with the volunteer loading the array in the scanner, resulting in only 6% difference. This percentage difference of the reference voltages is indicative of the decoupling inefficiency of the array and shows that the

coupling between the array and the body resonator is minimal. In this case, the PET/MRI 32-channel array shows 94% decoupling efficiency.

### 2.3.1 MRI phantom imaging

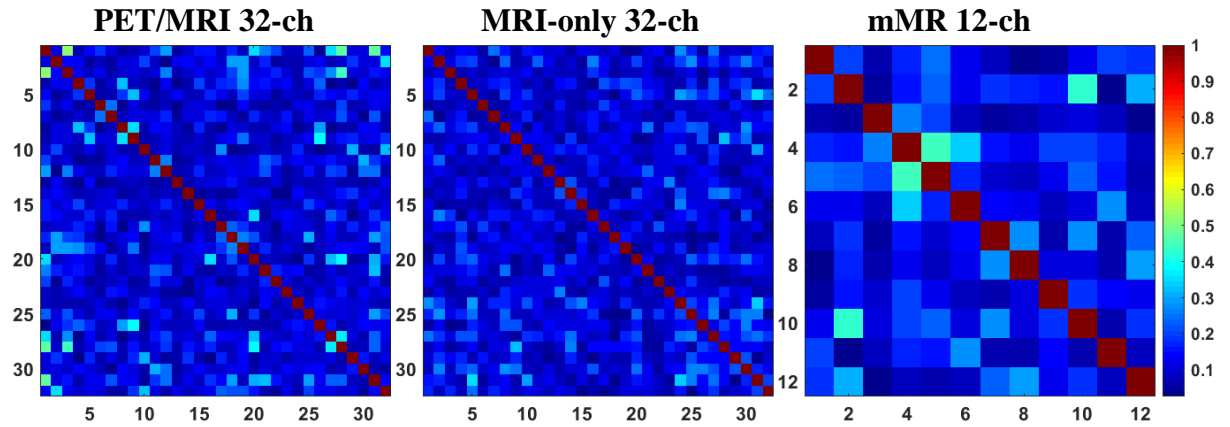
Table 2-1 summarizes the MRI quality parameter means and SDs, such as  $SNR_0$ ,  $SNR_g$  sensitivity-based g-factor and inverse g-factor as estimated for all arrays at all acceleration factors, in 1D (LR or FH) and 2D. The table also includes the mean and SD of the noise correlation coefficients for all arrays. Noise correlation coefficient matrices representing between-channel coupling for the three arrays are graphically represented in Figure 2- 2. Each array produced a mean noise correlation coefficient of less than 0.2 (20% correlation). For example, noise correlation means at R=2, excluding self-correlated elements (diagonal), were 10%, 11% and 15% for the MRI-only 32-channel, PET/MRI 32-channel and mMR 12-channel arrays, respectively.

**Table 2-1: Estimated mean  $\pm$  SD values of the parallel imaging quality parameters.**

	PET/MRI 32-channel					MRI-only 32-channel					mMR 12-channel				
	<i>R=1</i>	<i>R=2</i>	<i>R=3</i>	<i>R=4</i>	<i>R=6</i>	<i>R=1</i>	<i>R=2</i>	<i>R=3</i>	<i>R=4</i>	<i>R=6</i>	<i>R=1</i>	<i>R=2</i>	<i>R=3</i>	<i>R=4</i>	<i>R=6</i>
<b>noise correlation coefficient</b>	0.110 $\pm 0.004$	0.110 $\pm 0.002$	0.120 $\pm 0.011$	0.120 $\pm 0.004$	0.120 $\pm 0.003$	0.090 $\pm 0.003$	0.100 $\pm 0.004$	0.100 $\pm 0.001$	0.110 $\pm 0.001$	0.110 $\pm 0.002$	0.150 $\pm 0.001$	0.150 $\pm 0.021$	0.150 $\pm 0.011$	0.150 $\pm 0.001$	0.160 $\pm 0.001$
<b>Encoding 1D-LR</b>															
<b>SNR<sub>0</sub></b>	965 $\pm$ 112	-	-	-	-	871 $\pm$ 98	-	-	-	-	749 $\pm$ 90	-	-	-	-
<b>SNR<sub>g</sub></b>	-	608 $\pm$ 57	428 $\pm$ 38	271 $\pm$ 25	88 $\pm$ 22	-	581 $\pm$ 71	386 $\pm$ 66	229 $\pm$ 34	55 $\pm$ 18	-	488 $\pm$ 58	247 $\pm$ 26	99 $\pm$ 7	24 $\pm$ 3
<b>g-factor</b>	1	1.06 $\pm$ 0.05	1.25 $\pm$ 0.16	1.81 $\pm$ 0.54	7.03 $\pm$ 4.59	1	1.06 $\pm$ 0.05	1.32 $\pm$ 0.18	2.13 $\pm$ 0.79	15.41 $\pm$ 13.56	1	1.05 $\pm$ 0.04	2.10 $\pm$ 1.07	6.94 $\pm$ 5.42	41.75 $\pm$ 39.56
<b>1/g-factor</b>	1	0.98 $\pm$ 0.04	0.82 $\pm$ 0.10	0.60 $\pm$ 0.16	0.23 $\pm$ 0.15	1	0.95 $\pm$ 0.04	0.77 $\pm$ 0.10	0.53 $\pm$ 0.17	0.16 $\pm$ 0.15	1	0.96 $\pm$ 0.04	0.59 $\pm$ 0.25	0.28 $\pm$ 0.24	0.08 $\pm$ 0.13
<b>1D-FH</b>															
<b>SNR<sub>0</sub></b>	929 $\pm$ 107	-	-	-	-	816 $\pm$ 96	-	-	-	-	655 $\pm$ 83	-	-	-	-
<b>SNR<sub>g</sub></b>	-	648 $\pm$ 53	467 $\pm$ 35	279 $\pm$ 26	73 $\pm$ 19	-	549 $\pm$ 41	365 $\pm$ 59	216 $\pm$ 18	52 $\pm$ 12	-	443 $\pm$ 56	224 $\pm$ 23	90 $\pm$ 6	21 $\pm$ 2
<b>g-factor</b>	1	1.01 $\pm$ 0.02	1.16 $\pm$ 0.11	1.82 $\pm$ 0.59	8.97 $\pm$ 6.27	1	1.06 $\pm$ 0.05	1.32 $\pm$ 0.17	2.12 $\pm$ 0.79	15.44 $\pm$ 13.54	1	1.05 $\pm$ 0.04	2.10 $\pm$ 1.06	6.93 $\pm$ 5.40	43.77 $\pm$ 41.75
<b>1/g-factor</b>	1	0.99 $\pm$ 0.02	0.87 $\pm$ 0.08	0.60 $\pm$ 0.17	0.19 $\pm$ 0.16	1	0.95 $\pm$ 0.04	0.77 $\pm$ 0.10	0.53 $\pm$ 0.17	0.16 $\pm$ 0.15	1	0.96 $\pm$ 0.04	0.59 $\pm$ 0.25	0.27 $\pm$ 0.24	0.08 $\pm$ 0.13
<b>2D</b>	<i>R=2x2</i>	<i>R=2x3</i>	<i>R=2x4</i>	<i>R=3x3</i>	<i>R=3x4</i>	<i>R=2x2</i>	<i>R=2x3</i>	<i>R=2x4</i>	<i>R=3x3</i>	<i>R=3x4</i>	<i>R=2x2</i>	<i>R=2x3</i>	<i>R=2x4</i>	<i>R=3x3</i>	<i>R=3x4</i>
<b>SNR<sub>g</sub></b>	572 $\pm$ 23	404 $\pm$ 21	237 $\pm$ 16	324 $\pm$ 19	192 $\pm$ 14	623 $\pm$ 26	406 $\pm$ 19	233 $\pm$ 15	330 $\pm$ 16	198 $\pm$ 13	427 $\pm$ 21	196 $\pm$ 15	64 $\pm$ 14	132 $\pm$ 16	42 $\pm$ 9
<b>g-factor</b>	1.05 $\pm$ 0.03	1.23 $\pm$ 0.14	1.97 $\pm$ 0.66	1.59 $\pm$ 0.36	2.52 $\pm$ 0.94	1.06 $\pm$ 0.03	1.35 $\pm$ 0.18	2.28 $\pm$ 0.88	1.72 $\pm$ 0.42	2.73 $\pm$ 1.14	1.12 $\pm$ 0.06	2.75 $\pm$ 1.89	10.16 $\pm$ 5.84	5.41 $\pm$ 4.86	18.51 $\pm$ 13.03
<b>1/g-factor</b>	0.95 $\pm$ 0.03	0.82 $\pm$ 0.09	0.56 $\pm$ 0.16	0.66 $\pm$ 0.13	0.45 $\pm$ 0.15	0.94 $\pm$ 0.03	0.75 $\pm$ 0.10	0.50 $\pm$ 0.16	0.61 $\pm$ 0.13	0.42 $\pm$ 0.14	0.89 $\pm$ 0.05	0.50 $\pm$ 0.24	0.19 $\pm$ 0.22	0.34 $\pm$ 0.21	0.13 $\pm$ 0.16

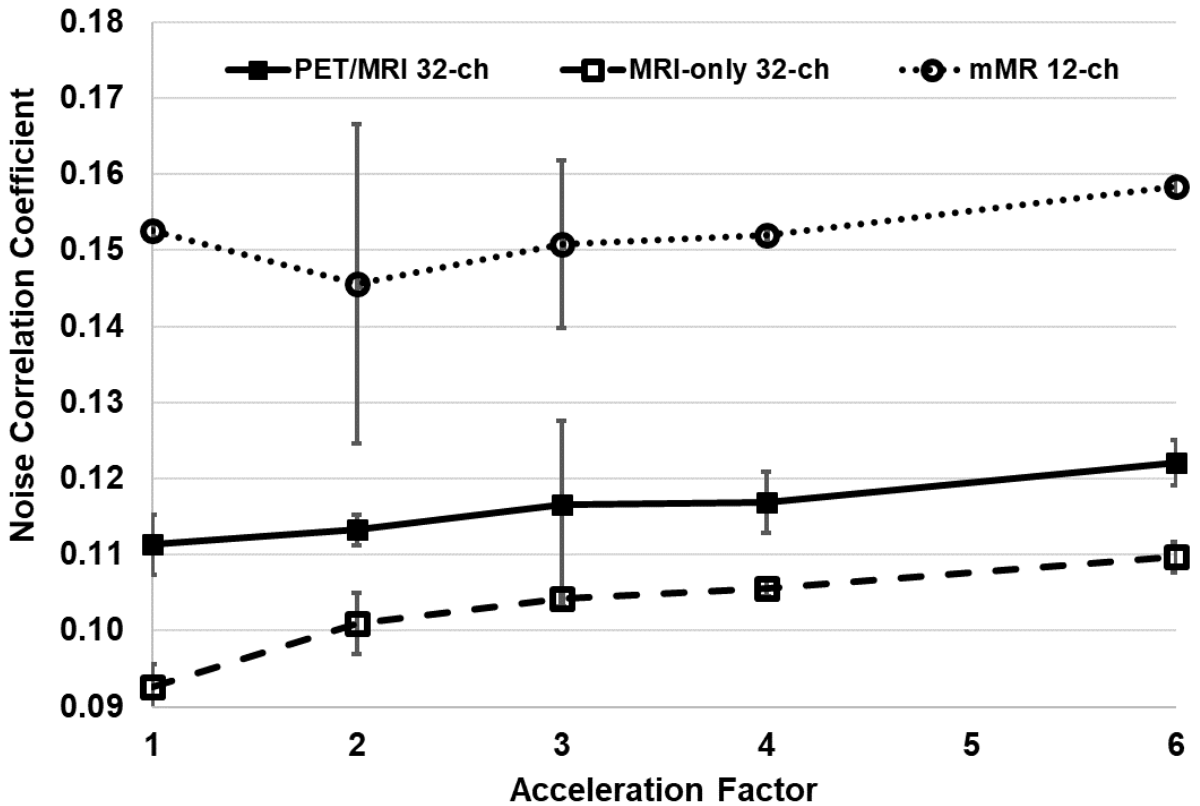
The parallel imaging quality parameters SNR<sub>g</sub>, g-factor and noise correlation coefficients, are estimated for different phase encoding direction in 1D (LR or FH) and in 2D (LR & FH).

**Figure 2-2: Noise correlation coefficients matrix for each of the three arrays.**



**Correlation matrix for the three arrays; PET/MRI 32-channel, MRI-only 32-channel, and mMR 12-channel. The scale of the color bar represents the correlation coefficients values, which could also be reported as correlation percentage. The average noise correlation coefficients (excluding the matrix diagonal) for the PET/MRI array was measured to be  $< 0.13$  ( $< 13\%$  correlation).**

**Figure 2-3: Mean and SD of the noise correlation coefficients shown as a function of acceleration factor for the three arrays.**



**Of note: the mMR 12-channel array mean noise correlation shows a drop at R = 2, with SD of 0.021 (2.1%). The MRI-only 32-channel shows the lowest values, yet noise correlation coefficients increases by 0.019 (1.9%) from R = 1 to R = 6, while the PET/MRI 32-channel array has shown an increase by 0.012 (1.2%).**

Figure 2-3 displays means and SDs of the noise correlation coefficients for the three arrays as a function of the acceleration factor, with the mMR 12-channel array producing the largest standard deviation (2.1%) of all three arrays.

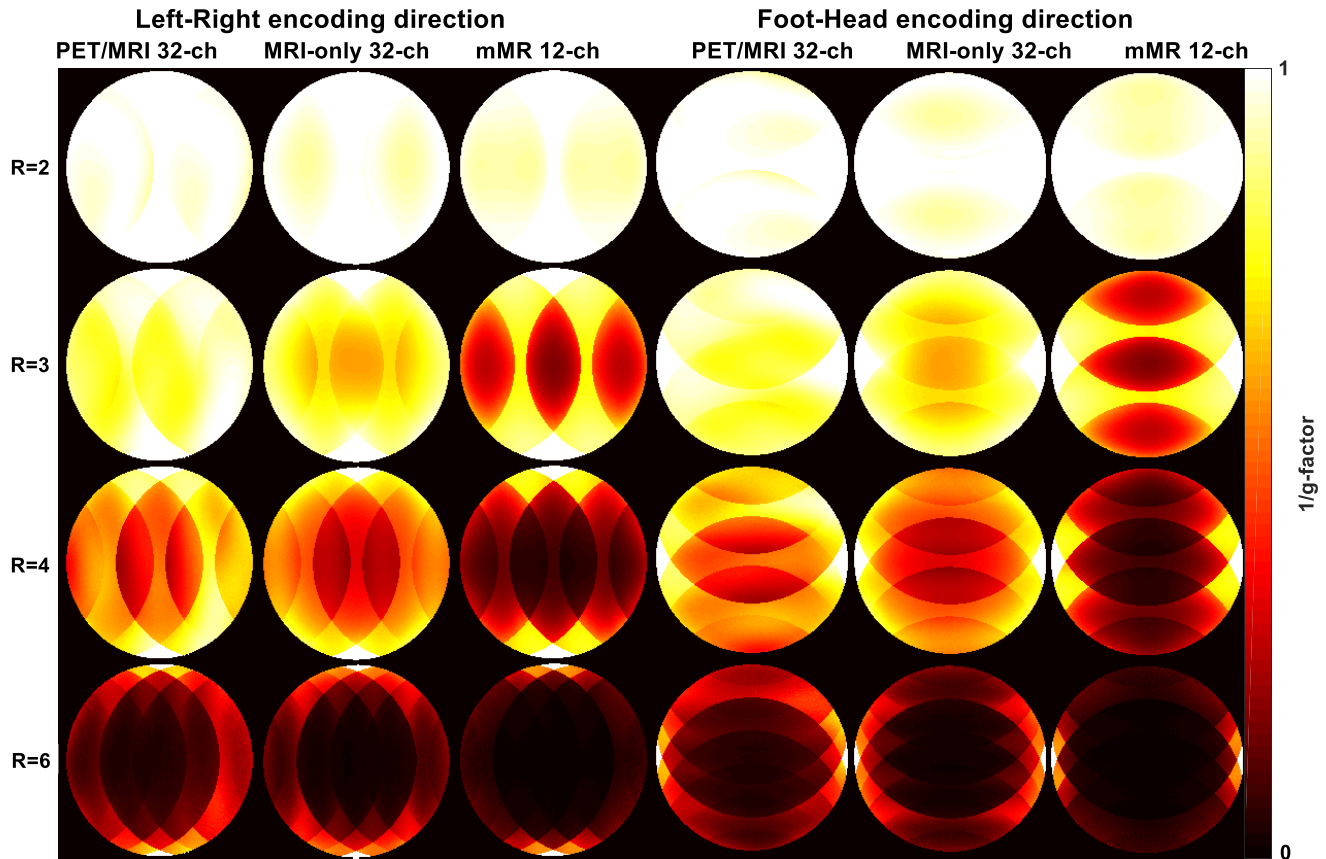
Figure 2-4 presents measured inverse g-factors maps for 1D acceleration (phase encoding in LR and FH direction) for all arrays. The 1/g-factor maps of the PET/MRI 32-channel array are compared to the two commercial arrays for each acceleration factor and produced



the lowest mean g-factor and, hence, the lowest noise amplification of the three arrays, as recorded in Table 2-1. For example, at acceleration factor  $R=3$  in the LR direction, the mMR array produced a mean g-factor of 2.10 compared to 1.32 for the MRI-only 32-channel array and 1.25 for the PET/MRI 32-channel array. A similar pattern of g-factor was also observed when estimated with encoding in the FH direction.

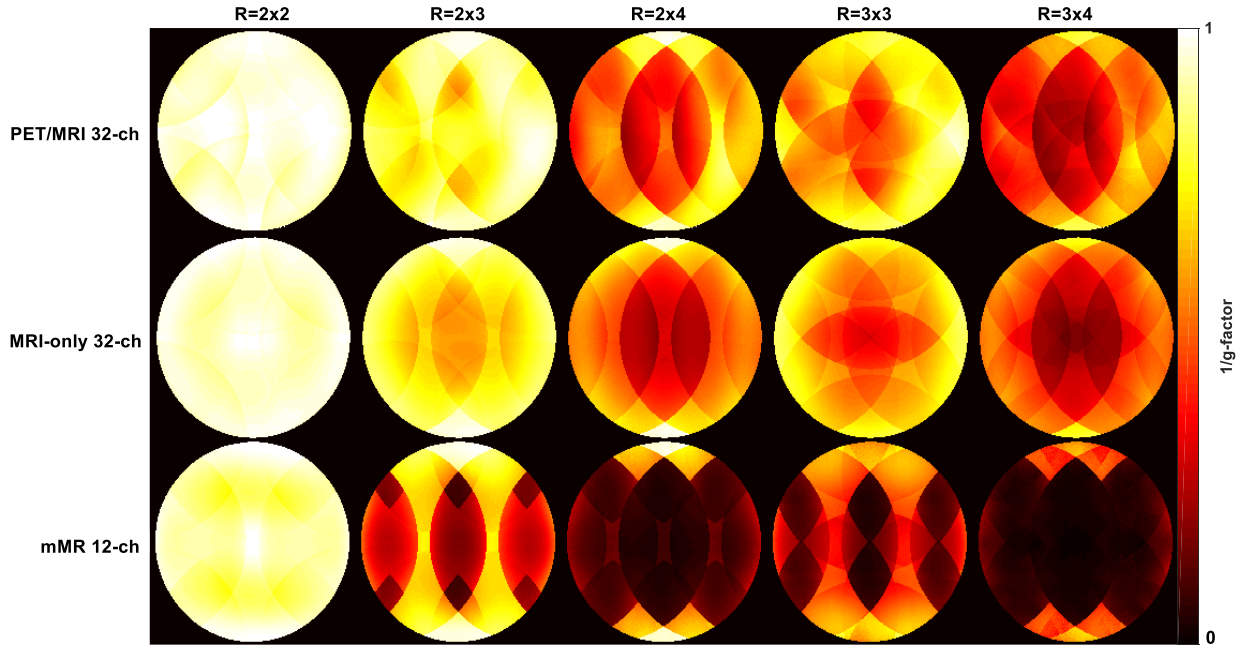
Using percentage difference formula number [4] with parameters in Table 2-1, one can compare any parameters of one array to another. Beyond acceleration factor of  $R=2$  in either encoding directions, the PET/MRI 32-channel array shows more than 30% improvement in g-factor and  $SNR_g$  compared to the mMR array. The PET/MRI 32-channel array mean g-factor for  $R=3$  in the FH encoding direction was improved relative to the LR phase encoding direction by 7%, while the MRI-only 32-channel array showed no changes in mean g-factors at  $R=3$  according to phase encoding direction.

**Figure 2-4:  $1/g$  factor maps for the three arrays with  $R=2$  to  $R=6$  in both LR and FH phase encoding direction.**



**Notice in the figure, a substantial noise amplification beyond  $R=2$  for the mMR 12-channel array in comparison to the two 32-channel arrays.**

**Figure 2-5: 1/g factor maps in the case of 2D acceleration with RR = 2x2 to RR=3x4.**



The PET/MRI 32-channel array achieves the least noise amplification with max of 0.97 at RR=3x3 in comparison to 0.88 for the MRI-only array, while the mMR 12-channel array produced.

**Table 2-2: Percent difference of parallel imaging quality parameters comparing both 32-channel arrays.**

PET/MRI 32-ch and MR-only 32-ch Percentage Difference (%)					
	R=1	R=2	R=3	R=4	R=6
SNR <sub>0</sub>	10.3	19.2	11.7	-1.1	-0.2
SNR <sub>g</sub>	5.2	4.4	10.4	16.9	45.6
Noise Correlation coefficients	18.4	11.6	11.2	10.2	10.7
Max g-factor	0	6.0	-5.1	-16.4*	-107.0*
Mean g-factor	0	0.5	-5.5	-15.9*	-74.7*
Mean 1/g-factor	0	-0.3	5.9	11.9	39.3

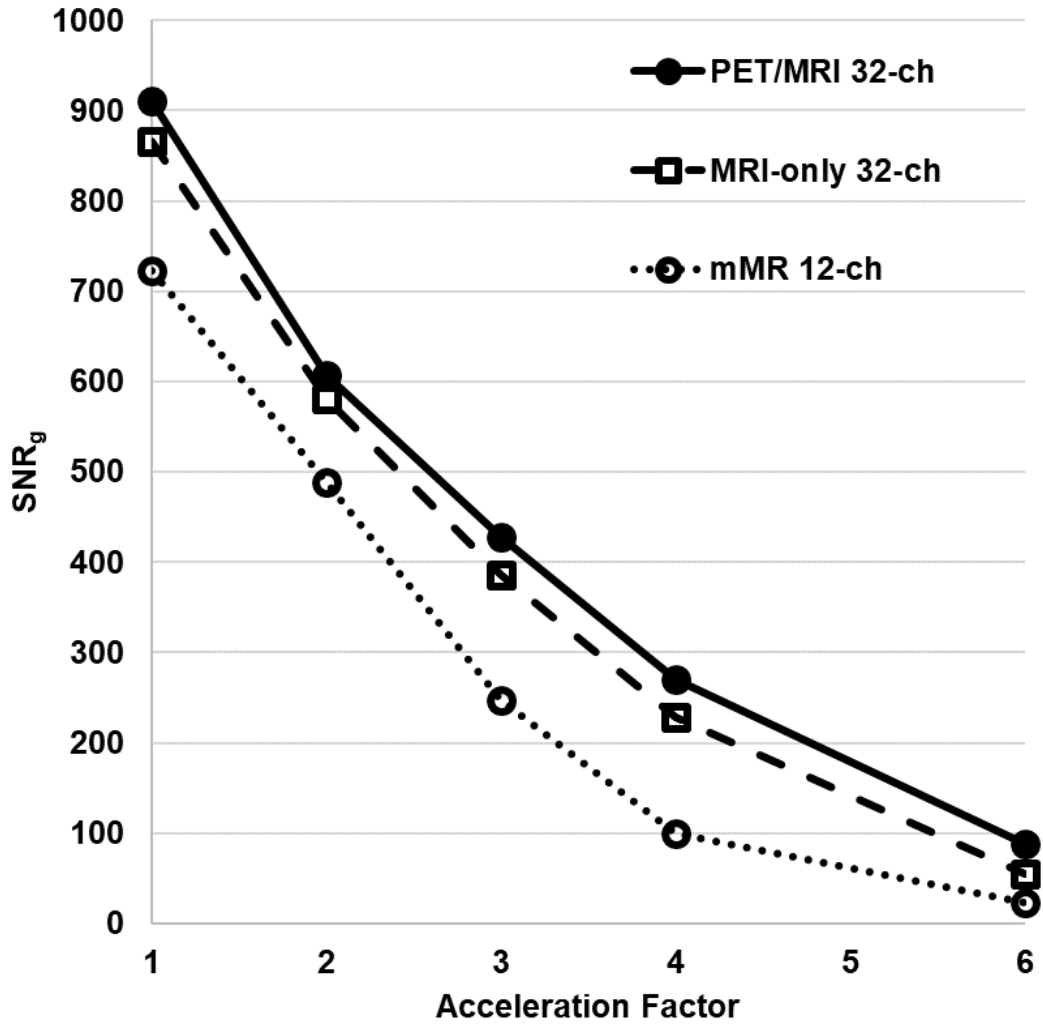
*\*Negative value indicates advantage of the PET/MRI 32ch over the MRI-only.*

Figure 2-5 presents the  $1/g$ -factor maps for selected 2D acceleration factors  $R_{LR} \times R_{FH} = 2 \times 2, 2 \times 3, 2 \times 4, 3 \times 3$  and  $3 \times 4$ . In Figure 2-5 and Table 2-1, the 2D acceleration is shown to be possible with the PET/MRI 32-channel for up to  $3 \times 3$  with only a SNR loss of less than half of that of the mMR 12-channel array, and 8% better than the MRI-only 32-channel array. Table 2-2 focuses on the percentage differences of the parallel imaging quality parameters between the two 32-channel arrays for the case of L-R encoding direction. The percentage difference between the non-accelerated ( $R=1$ )  $SNR_0$  for both arrays was 10.3%, while the  $SNR_0$  measured from the PET/MRI array at  $R=2$  was better than the MRI-only array by approximately 19%. The percentage differences in the case of mean  $g$ -factor for  $R=1$  and  $R=2$  were found to be negligible, while for accelerations factors  $R > 2$ , the mean  $g$ -factor of the PET/MRI array was more than 5% over that measured from the MRI-only array, as seen in Table 2-2. The mean and SD of  $SNR_g$ , as a function of acceleration factor for the three arrays are displayed in Figure 2-6.

### 2.3.2 MRI in-vivo imaging

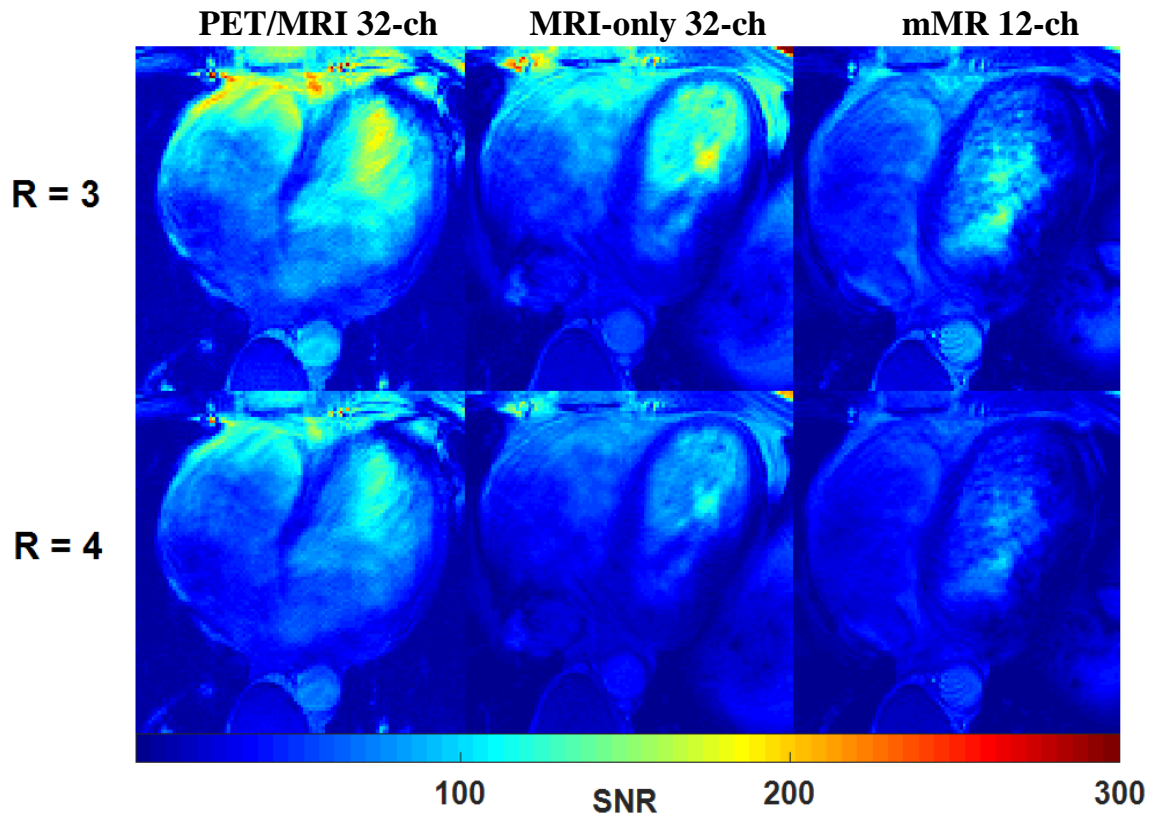
The  $SNR_g$  pixel-by-pixel maps from in-vivo acquisitions (single centre-slice 2D TrueFISP, cine disabled), at 1D acceleration factor  $R=3$  and  $R=4$ , were derived by utilising elements sensitivity and are presented in Figure 2-7. At the mid-ventricular level and up to the apex, the effect of the noise amplifications at  $R=3$  (and higher) are comparable for the 32-channel arrays and they outperform the mMR 12-channel array. A higher  $SNR_g$  from the in-vivo acquisitions (2D TrueFISP cine 4-chamber view) on a male volunteer was achieved using the PET/MRI 32-channel array (Figure 2-8). The line profile of the  $SNR_g$  across the center of a 4-chamber view of the heart was approximately 15% higher for the PET/MRI 32-channel array over the two other conventional arrays (Figure 2-9).

Figure 2-6: Estimated  $SNR_g$  as a function of acceleration rates from R=1 to R=6 with GRAPPA reconstruction.



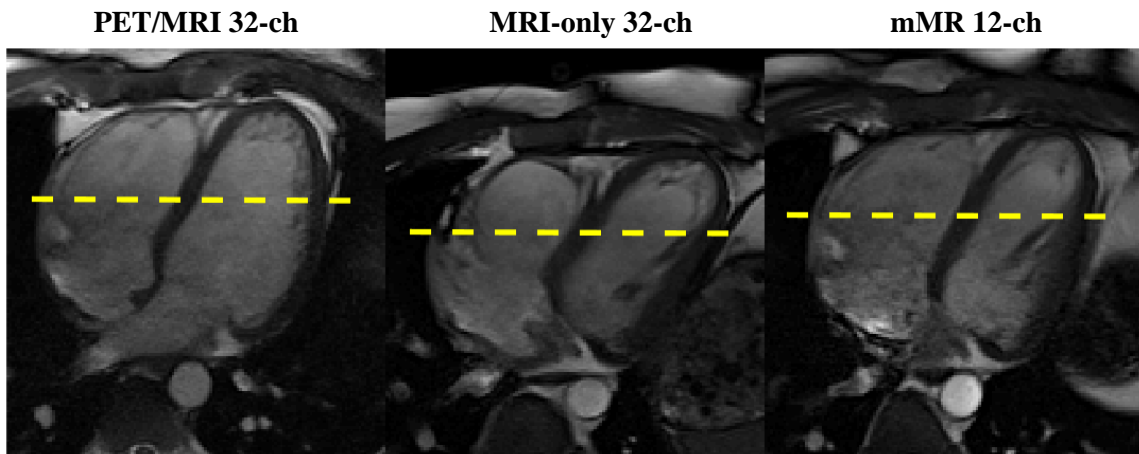
The estimated  $SNR_g$  shown here follows the theory and is in agreement with expected profile as first proposed by (Griswold et al., 2002)

**Figure 2-7: Comparison of In-vivo  $SNR_g$  maps generated using the three arrays at R=3 and R=4.**



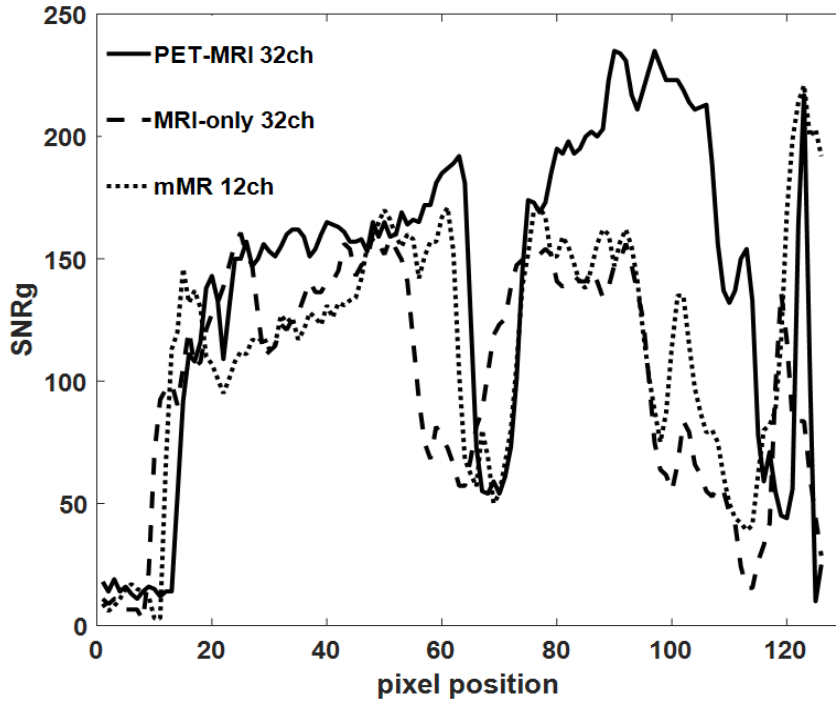
In-vivo maps of  $SNR_g$  (i.e. including noise amplification considerations) comparison of the three arrays, using a single centre-slice 2D TrueFISP image acquired at R=3 and R=4, with left-right encoding. The SNR maps show greater degradation of the SNR for the mMR 12- channel compared to the 32- channel arrays at higher acceleration factors.

**Figure 2-8: 4-chamber view images acquired with a 2D TrueFISP cine sequence on a male volunteer.**



**The first of 25 4-chamber view images acquired with a 2D-TrueFISP cine sequence on a male volunteer with acceleration factor of 2 (R=2).**

**Figure 2-9: A centre line profile of the  $SNR_g$  map of the heart for the three arrays.**



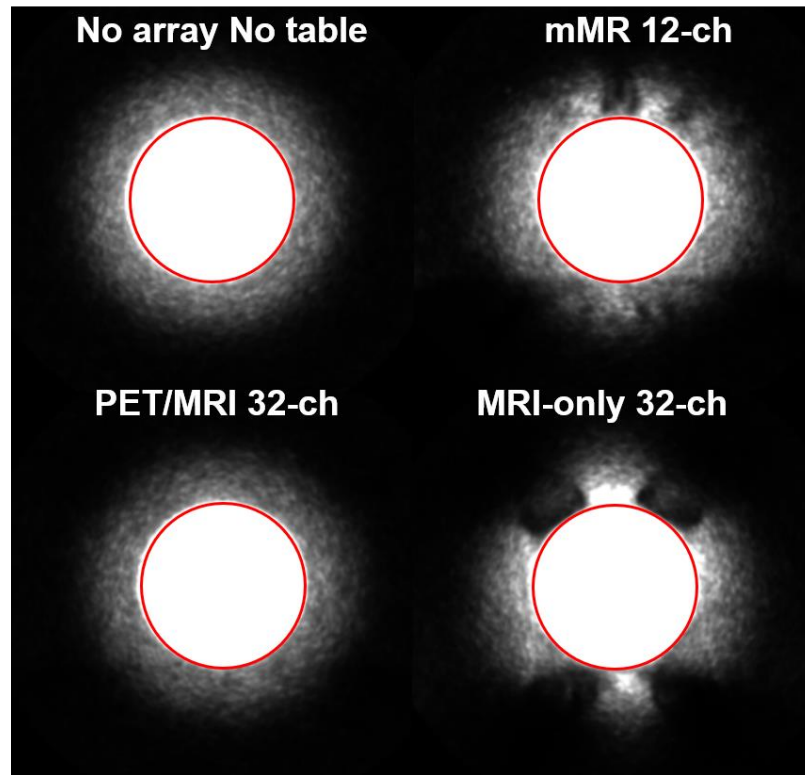
**The centre line (dashed line in Fig.2-8) profile of the heart showing  $SNR_g$  generated by the three arrays using a 2D TrueFISP cine 4-chamber view. The scanning plane/orientation are not identical, and the line had to be centred in the heart as much as possible for each acquisition above.**

### 2.3.3 PET imaging

Figure 2-10 compares center-slice of the PET activities acquired on the Ge-68 phantom for the three arrays and the “no-array, no-table” measurement. The estimated global mean of the PET counts per second (CPS), from the circled region contouring the phantom, were found to be: 557CPS, 534CPS, 436CPS and 395CPS, for “no-table no-array”, PET/MRI 32-channel array, MRI-only 32-channel array and mMR 12-channel array respectively. The difference between the PET CPS from “no-table, no-array” to PET/MRI 32-channel array was 4.1%.



**Figure 2-10: PET counts per second (CPS) map of the middle slice of the Ge-68 phantom for each array separately and reference (“no-array, no-table”).**



**The global mean count per seconds were measured from the region contoured by the red circle. The figure is windowed to accentuate the hardware attenuation artefacts visible immediately outside the phantom. All images used identical windowing.**

## 2.4 Discussion and Conclusion

Overall, the MRI performance assessed by the percentage differences of noise correlation, g-factor and SNR between the two 32-channel arrays is found to be similar and favoured the PET/MRI array greatly at acceleration of  $R=4$  and  $R=6$ . The design of this dedicated PET/MRI array has provided superior (>30%) in all the results over the mMR 12-channel array for acceleration factors greater than 2, theoretically allowing for use of shorter breath-holds, which is often critical in cardiac imaging.

The method used in this work to assess the MRI quality parameters for parallel imaging are commonly used by researchers as reported in <sup>13,18,33-35</sup>. This work has combined the use of both parallel imaging techniques with high density arrays to shorten the breath-hold during acquisition which is necessary for cardiovascular imaging. At R=4 using TrueFISP imaging, the shortest breath-hold that could be achieved was approximately 9 seconds producing 25 images of a single slice.

Unlike the two currently-used arrays, the anterior portion of the PET/MRI array is very light and thin and as such does not conform to the subject's chest under its own weight. This was resolved by using straps to achieve adequate conformity and proximity to the subject's body. With this design, its elements have the highest proximity to the heart of the three arrays, which benefits penetration depth and results into a better SNR far from the array as demonstrated by Figure 2-9.

We recorded lower noise correlation SDs (0.5%) for both 32-channel arrays compared to the mMR 12-channel array, as seen in Figure 3, which indicates greater stability of the arrays' noise correlation coefficients as a function of acceleration factor during parallel imaging. One element of the PET/MRI 32-channel array produced a noise coefficient of 61% and this may have caused the high mean of the coefficients. This could be due to off-resonance tuning of the element which introduced excess noise to the neighbouring ones.

We have demonstrated with the phantom results in Figures 2-4 and 2-5 that the 32-channel PET/MRI array produces higher SNR than the other two arrays for 1D and 2D acceleration, which confirms the array is a strong candidate for use as the MRI receiver array in hybrid

PET/MRI cardiovascular imaging. As seen in Table 2-1, at almost all R values, the mean g-factor of the PET/MRI 32-channel array showed better results than those of the other two arrays. The SNR behaviour from phantom and *in vivo* measurements matches those reported in <sup>28</sup> regarding parallel imaging theories compared to the effect of acceleration on SNR measured with phased arrays. It was noticed that the estimated SNR<sub>g</sub> of the MRI-only 32-channel array at R=4 is 17% less than the PET/MRI array, yet it produced the smallest noise correlation coefficient. The reason for this behaviour could be due to smaller element size and geometry differences from one array to the other, or, alternative reasons may be a suboptimal output gain adjustment or imperfect signal pre-amplification. The parallel imaging quality parameters of the prospectively designed PET/MRI 32-channel array are comparable to the MRI-only array confirming its ability to be employed for 1D acceleration up to R=6, and 2D parallel imaging up to acceleration of 3x3.

In conclusion, the PET/MRI 32-channel array prospectively-designed for simultaneous PET and MRI demonstrated competitive MRI performance compared to both the 32-channel MRI-only array and the 12-channel PET/MRI array. PET photon attenuation caused by the PET/MRI 32-channel array was measured to be <5% compared to the no-array PET photon activities. The PET performance will be studied in detail and will be presented in a separate manuscript.

We therefore conclude, that the PET/MRI 32-channel array studied here, is a viable alternative for simultaneous cardiovascular PET/MRI using parallel imaging. The PET/MRI array can surpass currently used arrays, particularly for high parallel imaging acceleration applications.

## 2.5 Acknowledgements

The authors gratefully acknowledge: Funding from MITACS (Application Ref. IT12869) (to JThé), an industry-sponsored internship (to AF) in collaboration with Multi Magnetics Inc (London, Ontario, Canada). Partial salary support of AF by NSERC Discovery Grant (No. RGPIN-2016-05055) (to JThé), infrastructure support by Ontario Research Fund (RE07-021) (to FSP) and by Canada Foundation for Innovation Grant (11358) (to FSP).

## 2.6 References

1. Pichler BJ, Wehrl HF, Kolb A, Judenhofer MS. Positron Emission Tomography/Magnetic Resonance Imaging: The Next Generation of Multimodality Imaging? *Semin Nucl Med.* 2008;38(3):199-208.
2. Catana C, Drzezga A Fau - Heiss W-D, Heiss Wd Fau - Rosen BR, Rosen BR. PET/MRI for neurologic applications. *Journal of Nuclear Medicine.* 2012;53(1916–1925).
3. White JA, Rajchl M, Butler J, Thompson RT, Prato FS, Wisenberg G. Active Cardiac Sarcoidosis First Clinical Experience of Simultaneous Positron Emission Tomography– Magnetic Resonance Imaging for the Diagnosis of Cardiac Disease. *Circulation.* 2013;127(22):e639-e641.
4. Camici PG, Prasad SK, Rimoldi OE. Stunning, Hibernation, and Assessment of Myocardial Viability. *Circulation.* 2008;117(1):103-114.
5. Nensa F, Beiderwellen K, Heusch P, Wetter A. Clinical applications of PET/MRI: current status and future perspectives. *Diagnostic and Interventional Radiology.* 2014;20(5):438-447.
6. Nensa F, Bamberg F, Rischpler C, et al. Hybrid cardiac imaging using PET/MRI: a joint position statement by the European Society of Cardiovascular Radiology (ESCR) and the European Association of Nuclear Medicine (EANM). *European Journal of Hybrid Imaging.* 2018;2(1):14.
7. Pichler B, Judenhofer M, Wehrl H. PET/MRI hybrid imaging: devices and initial results. *Eur Radiol.* 2008;18(6):1077-1086.

8. Wagenknecht G, Kaiser H-J, Mottaghy FM, Herzog H. MRI for attenuation correction in PET: methods and challenges. *Magnetic Resonance Materials in Physics, Biology and Medicine*. 2013;26(1):99-113.
9. Rausch I, Quick HH, Cal-Gonzalez J, Sattler B, Boellaard R, Beyer T. Technical and instrumental foundations of PET/MRI. *European Journal of Radiolog*. 2017;94:A3–A13.
10. Tellmann L, Quick H, Bockisch A, Herzog H, Beyer T. The effect of MR surface coils on PET quantification in whole-body PET/MR: results from a pseudo-PET/MR phantom study. *Medical physics*. 2011;38(5):2795-2805.
11. MacDonald LR, Kohlmyer S, Liu C, Lewellen TK, Kinahan PE. Effects of MR surface coils on PET quantification. *Medical physics*. 2011;38(6):2948-2956.
12. Kartmann R, Paulus DH, Braun H, et al. Integrated PET/MR imaging: Automatic attenuation correction of flexible RF coils. *Medical physics*. 2013;40(8):082301.
13. Wintersperger BJ, Reeder SB, Nikolaou K, et al. Cardiac CINE MR imaging with a 32-channel cardiac coil and parallel imaging: Impact of acceleration factors on image quality and volumetric accuracy. *J Magn Reson Imaging*. 2006;23(2):222-227.
14. Anazodo UC, Thiessen JD, Ssali T, et al. Feasibility of simultaneous whole-brain imaging on an integrated PET-MRI system using an enhanced 2-point Dixon attenuation correction method. *Frontiers in Neuroscience*. 2015;8(434).
15. Sander CY, Keil B, Chonde DB, Rosen BR, Catana C, Wald LL. A 31-channel MR brain array coil compatible with positron emission tomography. *Magn Reson Med*. 2014;73(6):2363-2375.

16. Anazodo UC, Farag A, Theberge J, et al. Assessment of PET performance of a 32-Channel MR Brain Array Head Coil Compatible with PET for Integrated PET-MRI. Paper presented at: PSMR; May 23rd – 25th 2016; Cologne / Germany.
17. Dregely I, Lanz T, Metz S, et al. A 16-channel MR coil for simultaneous PET/MR imaging in breast cancer. *European Society of Radiology*. 2014;25:1154–1161.
18. Schmitt M, Potthast A, Sosnovik DE, et al. A 128-channel receive-only cardiac coil for highly accelerated cardiac MRI at 3 Tesla. *Magn Reson Med*. 2008;59(6):1431-1439.
19. Paulus DH, Braun H, Aklan B, Quick HH. Simultaneous PET/MR imaging: MR-based attenuation correction of local radiofrequency surface coils. *Medical physics*. 2012;39(7):4306-4315.
20. Fürst S, Souvatzoglou M, Martinez-Möller A, Nekolla S, Schwaiger M, Ziegler S. Impact of MRI surface coils on quantification in integrated PET/MR. *The Journal of Nuclear Medicine*. 2012;53(supplement 1):436.
21. Ouyang J, Petibon Y, Huang C, Reese TG, Kolnick AL, Fakhri GE. Quantitative simultaneous positron emission tomography and magnetic resonance imaging. *Journal of Medical Imaging*. 2014;1(3):1-7, 7.
22. Ferguson A. JM, YiSu, Debra Hewing, and Richard Laforest. Attenuation Effects of MR Headphones During Brain PET/MR Studies. *Journal of Nuclear Medicine Technology*. 2014;42:93–100.
23. Eldib M, Bini J, Robson P, et al. Markerless attenuation correction for carotid MRI surface receiver coils in combined PET/MR imaging. *Physics in Medicine & Biology*. 2015;60(12):4705.

24. Frohwein LJ, Heß M, Schlicher D, et al. PET attenuation correction for flexible MRI surface coils in hybrid PET/MRI using a 3D depth camera. *Physics in Medicine & Biology*. 2018;63(2):025033.
25. Carney JP, Townsend DW, Rappoport V, Bendriem B. Method for transforming CT images for attenuation correction in PET/CT imaging. *American Association of Physicists in Medicine*. 2006;33(4):976-983.
26. Patrick JC, Terry Thompson R, So A, et al. Technical Note: Comparison of megavoltage, dual-energy, and single-energy CT-based  $\mu$ -maps for a four-channel breast coil in PET/MRI. *Medical physics*. 2017;44(9):4758-4765.
27. Haacke EM, Wielopolski PA, Tkach JA, Modic MT. Steady-state free precession imaging in the presence of motion: application for improved visualization of the cerebrospinal fluid. *Radiology*. 1990;175(2):545-552.
28. Griswold MA, Jakob PM, Heidemann RM, et al. Generalized autocalibrating partially parallel acquisitions (GRAPPA). *Magn Reson Med*. 2002;47(6):1202-1210.
29. Henkelman RM. Measurement of signal intensities in the presence of noise in MR images. *Medical physics*. 1985;12(2):232-233.
30. Pruessmann KP, Weiger M, Scheidegger MB, Boesiger P. SENSE: Sensitivity encoding for fast MRI. *Magn Reson Med*. 1999;42(5):952-962.
31. Robson PM, Grant AK, Madhuranthakam AJ, Lattanzi R, Sodickson DK, McKenzie CA. Comprehensive quantification of signal-to-noise ratio and g-factor



for image-based and k-space-based parallel imaging reconstructions. *Magn Reson Med.* 2008;60:895–907.

32. Price RR, Axel L, Morgan T, et al. Quality assurance methods and phantoms for magnetic resonance imaging: Report of AAPM nuclear magnetic resonance Task Group No. 1. *Medical physics.* 1990;17(2):287-295.
33. Wiggins G, Triantafyllou C, Potthast A, Reykowski A, Nittka M, Wald L. 32-channel 3 Tesla receive-only phased-array head coil with soccer-ball element geometry. *Magn Reson Med.* 2006;56(1):216-223.
34. Meise FM, Rivoire J, Terekhov M, et al. Design and evaluation of a 32-channel phased-array coil for lung imaging with hyperpolarized 3-helium. *Magn Reson Med.* 2010;63(2):456-464.
35. Reeder SB, Wintersperger BJ, Dietrich O, et al. Practical approaches to the evaluation of signal-to-noise ratio performance with parallel imaging: Application with cardiac imaging and a 32-channel cardiac coil. *Magn Reson Med.* 2005;54(3):748-754

## Chapter 3

### 3 Evaluation of 511keV Photon Attenuation from a Novel 32-Channel Phased Array prospectively-designed for Cardiovascular Hybrid PET/MRI Imaging.

#### 3.1 Introduction

Simultaneous positron emission tomography (PET) and magnetic resonance imaging (MRI) is a valuable tool for assessing different forms of cardiac diseases using PET tracers sensitive to perfusion ( $^{13}\text{N}$ -ammonia), inflammation or myocardial viability ( $^{18}\text{F}$ -FDG), or sympathetic innervation ( $^{11}\text{C}$ -HED) in combination with MRI measurements of fibrosis, function, and more. However, this value is tied to how accurately PET measurements can be quantified and interpreted. A recent joint position statement from the European Society of Cardiovascular Radiology (ESCR) and the European Association of Nuclear Medicine (EANM)<sup>1</sup>, pointed out some unsolved issues of PET quantification in cardiovascular hybrid PET/MRI imaging. The statement identified the need for high-temporal and spatial resolutions for imaging of coronary atherosclerosis and other heart diseases. While, accurate PET quantification is an ongoing topic of research, the root cause of inaccurate quantification is usually associated with inaccurate attenuation correction (AC) inflicted by one or more of; the method/models used for PET attenuation correction<sup>2-5</sup>; natural motion due to patient respiration and heart activity<sup>6-8</sup>; and registration of flexible hardware<sup>9-14</sup>. Notably, one of the causes of inaccurate quantification of PET is the radio

frequency arrays (mobile and/or flexible), which are required to achieve high-temporal and spatial resolution in cardiovascular imaging. Photon attenuation from rigid and fixed arrays can be accurately corrected for, using a dual-energy computed tomography-based AC map (DCTAC)<sup>15</sup>, however one must consider the accuracy of the derived linear attenuation coefficient (LAC) at 511keV.

The effect of a fixed phased array on PET quantification has been studied extensively<sup>9</sup> and it is reported that PET tracer activities were underestimated by 19% when the AC map was not applied. Even when flexible phased arrays are designed to minimize attenuation, deviations in PET quantification as large as 10%-15% were reported in regions of interest adjacent to the flexible phased arrays<sup>11,12</sup>. Thus, applying AC map for flexible arrays is ideal for accurate PET quantification in most applications. Thereafter, more studies were dedicated to establishing a method to correct for attenuation of flexible arrays and in particular the registration of the AC map to PET images. A method for accurate registration of AC map of flexible RF arrays was developed and reported using fiducial markers to guide the registration of the hardware AC map with the PET image<sup>11,12</sup>. Most recently, the AC maps of flexible arrays were spatially registered using alternative methods without the need for markers: 1) An automatic algorithm using data from an ultra-short echo time (UTE) MRI scan<sup>14</sup>; 2) A method using the Microsoft Kinect V2 depth camera to track the 3D surface of the RF array and localize it inside the scanner's FOV and determine hardware AC map deformation parameters<sup>16</sup>. However, such approaches could not address the full range of imaging conditions, for example, the marker methods require markers to be present and fixed on the array during PET acquisition, which could affect the MRI images, besides may cause inaccurate registration which may result to inaccurate quantification of

PET<sup>17</sup>. Meanwhile, offline algorithms used for AC and registration require dedicated processors and are not straightforward for practical implementation in a clinical setting. Moreover, all AC map registration methods have still produced regional PET images with attenuation of >2.4%, and hence, the PET quantification issue remains unresolved when using the standard arrays.

Knowing the effect of the vendor's standard arrays on PET quantification, there is an urgent need to develop and validate a PET-compatible cardiac array that does not require hardware attenuation correction.

In a previous study we assessed a novel 32-channel, phased-array, prospectively-designed for PET/MRI cardiovascular imaging, and reported that it was capable of achieving high spatial and temporal resolution (up to acceleration factor R=6) for MRI imaging<sup>18</sup>.

In the present study, the same novel array is thoroughly evaluated for PET image quality and compared to two standard arrays. Hardware AC maps for the posterior part of each array were developed together with the NEMA-phantom AC map. In order to quantify the effect of each part of the array on PET counts separately, NEMA Standard Publication NU 2-2001 for image quality measurements<sup>19</sup> were performed using the anterior, posterior, and both anterior/posterior parts of each of the three arrays, as well as, for no-array. Applying attenuation correction during image reconstruction were performed using two approaches: 1) MRAC; where PET image reconstruction used MRI-based AC map for the liquid in phantom, produced by the scanner, together with a dual-energy CT-based AC map for the housing of the NEMA Body-Phantom. 2) DCTAC; where reconstruction of the PET image used dual-energy CT-based AC maps for both the liquid in the phantom and the housing

of the phantom. Although we report using two reconstruction approaches, the scope of the study is not to compare the AC approaches. Instead, the two approaches were used to demonstrate the PET performance of the novel array in the best-case scenario of attenuation correction (DCTAC) and conventional PET reconstruction (MRAC) at low resolution.

## 3.2 Materials and Methods

The method and some of the materials described here are adapted from NEMA Standard Publication NU 2-2001 for PET image quality and accuracy of attenuation<sup>19</sup>, which has been used for assessing image quality of PET systems and instrumentation<sup>20,21</sup>.

### 3.2.1 The arrays under evaluation and phantom

A NEMA Body phantom IEC-2007 (National Electrical, Manufacturers Association Washington, DC, USA) was employed to carry out all PET quantification in this work (figure 3-1-a). As shown in figure 3-1 (b, c, and d), the three arrays used in this study are; the novel 32-channel PET/MRI array (Ceresensa, Canada 2016) consisting of two parts, anterior (flexible) and posterior (fixed); the 12-channel mMR array (Siemens Healthcare Limited, Erlangen, Germany) comprised of a 6-channel body matrix (flexible anterior) and 6-channel spine-matrix (fixed posterior); and the standard 32-channel MRI array (In-Vivo Corporation, Gainesville, FL, USA) with anterior (flexible) and posterior (fixed) parts.

### 3.2.2 AC maps

In order to achieve accurate PET quantification, AC maps for all hardware within the scanner must be developed and applied during attenuation correction, this includes the NEMA phantom housing (i.e. phantom without its liquid content). Therefore, we developed all necessary hardware AC maps using a Dual Energy CT (GE Healthcare, Discovery CT750 HD, Waukesha, USA) scan of the hardware components following the method of bilinear transformation of Hounsfield units (using mono-energetic reconstruction at 70kVp and 140kVp) to 511keV linear attenuation coefficient<sup>22</sup>. The developed DCTAC maps were for both the empty and filled NEMA body phantom and the

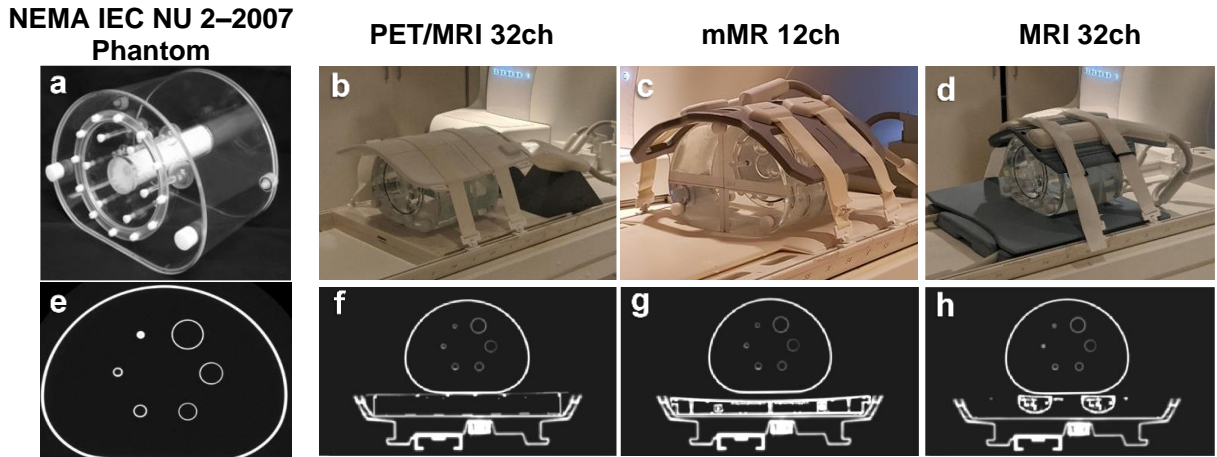
posterior part of each array, while the spine-matrix array was excluded, since its AC map is provided by the vendor.

For non-hardware AC maps, such as that related to the de-ionized water included in the NEMA phantom, two scenarios were examined: 1) Rely on MRAC to correct for water attenuation, with the rationale that this is the scenario of a non-research/ clinical study where pre-acquired patient CT data is not normally available to the PET/MRI system; 2) Develop DCTAC map for the phantom filled with water and use it for off-line attenuation correction of the PET image, with the rationale that, this is the scenario of a research setting, where patient PET/CT or CT-only data could be available for offline reconstruction.

### 3.2.3 PET phantom preparation and measurements set-up

The phantom background is defined to be the phantom volume without the six spherical-inserts nor the lung-insert. The phantom background (volume ~10.2L) was filled with deionized water and injected with  $^{18}\text{F}$ -FDG to reach an activity concentration of  $5.3 \pm 0.1 \text{ kBq/ml}$ . All six spheres (with inner diameters 10, 13, 17, 22, 28, and 37 mm) were filled with  $^{18}\text{F}$ -FDG to reach an activity concentration of  $201 \pm 5 \text{ kBq/ml}$ , making the phantom activities reach a 1:38 background-to-sphere ratio, where the background activity corresponds to a typical injected dose for total body studies<sup>19</sup>.

**Figure 3-1: NEMA body phantom (a) together with the novel PET/MRI 32ch, standard mMR12ch and MRI 32ch arrays.**



**NEMA body phantom (a) together with the novel PET/MRI 32ch, standard mMR12ch and MRI 32ch arrays (b, c and d respectively). The DCTAC maps for each hardware showing here the axial central slice for the NEMA phantom with posterior view of PET/MRI 32ch, mMR12ch and MRI 32ch arrays (e, f, g and h respectively). All  $\mu$ -maps are windowed to the same level.**

Markers were produced on the patient table, as well as the phantom body, and when both markers were matched the same position of the phantom on the table was consistently achieved with +/- 1mm tolerance. During all measurements, the isocenter was selected to be at the center line between position number 4 and 5 of the spine-matrix (marked on the patient table). This set-up ensured that no additional objects employed for positioning during the PET measurement and hence, data are free from added errors. The set-up also ensured the elimination of attenuation variation that the patient table itself may contribute.



### 3.2.4 Image acquisition and attenuation correction

For ease of reading throughout this manuscript, the anterior part of an array is denoted with letter A while the posterior part is denoted with letter P, and therefore both parts of an array are denoted with A&P, and part(s) may be referred to as case(s).

All PET acquisitions were performed on a 3.0T PET/MRI system (Biograph mMR Software Version VE11P, Siemens Healthineers, Erlangen, Germany), and followed the identical workflow routine. Evaluation of one complete array required one imaging session consisting of four PET measurements, where the first measurement was started once the activity reached the concentration described above. Each measurement comprised of a Dixon MRAC acquisition (2.5min) and a PET acquisition (10min). The four PET measurements were carried out in the following order: 1) the complete array (A&P) and NEMA phantom; 2) the posterior part (P) of the same array and NEMA phantom; 3) the anterior part (A) of the same array and NEMA phantom; 4) the NEMA phantom with no-array. Two imaging sessions were performed for each array, yielding two data sets for data analysis.

#### 3.2.4.1 MRAC

By MRAC, here, we refer to the PET/MR scanning conditions where only the posterior part of the array and the patient table hardware AC maps, together with MR-based AC map of the liquid in the phantom, are used for PET attenuation correction during image reconstruction. A MRAC map of the liquid portion of the NEMA phantom was acquired with the manufacturer's standard 2-point Dixon (3D dual-echo spoiled gradient sequence) using, TR/TE=4.14/2.51, Matrix size=240x126x127 at a resolution of 2.08x2.08x2.02 mm<sup>3</sup> and is intrinsically registered to the PET images. The AC maps of each array's posterior

part along with the NEMA phantom housing were registered to the scanner offline. For clarity, the reconstruction of the no-array AC images on the scanner used the phantom housing and patient table hardware AC maps, together with the phantom water MRAC map. The Biograph mMR's standard PET reconstruction algorithm, an Ordinary Poisson-Ordered Subsets Expectation Maximization (OP-OSEM)<sup>23</sup> approach, was applied using 3 iterations, 21 subsets, and a 4mm Gaussian filter.

#### 3.2.4.2 DCTAC

In order to obtain the ideal AC for both the hardware and liquid portion of the NEMA phantom, the raw, nonattenuation-corrected (NAC) data of each measurement was reconstructed offline using DCTAC of the NEMA phantom including the liquid portion and other hardware DCTAC maps. All PET reconstructions were performed offline using the manufacturer's e7-tools (Siemens Molecular Imaging, Knoxville, USA). The PET images were reconstructed using the same algorithm and parameters as described under the MRAC section above. The PET images output matrix size, which was 344x344x127 to achieve ideal reconstruction modality<sup>21</sup>.

#### 3.2.5 Data analysis

All data were corrected for the PET decay, due to the time used for hardware changing and sequence set-up, scatter and attenuation, before carrying out the analysis. All image processing and data analysis were computed using Matlab 9.3.0 (The MathWorks, Natick, MA, USA).

### 3.2.5.1 NAC data

NAC data are important in this analysis since it does not include any errors that an AC process might introduce. From NAC data, the global mean and standard deviation of each masked image (slice) were estimated. This mean and standard deviation were estimated for all cases of the three arrays, as well as for the no-array. The no-array data was considered the frame of reference that each part of an array was compared to. Therefore, relative percentage differences (RPD) between no-array and each part of an array were estimated and reported using equation 4 as reported in<sup>18</sup> and presented here for convenience, where  $v_1$  is the no-array case and  $v_2$  is any given case (A, P or A&P).

$$RPD = \frac{v_1 - v_2}{0.5 (v_1 + v_2)} 100\%$$

### 3.2.5.2 AC data

According to the NEMA NU 2–2001 standard, PET image quality can be analyzed from parameters such as contrast recovery (CR), background variability (BV) and contrast-to-noise ratio (CNR). Therefore, each sphere’s CR, BV and CNR were estimated from the relationships described in<sup>19</sup>, and the mean and standard deviation for each array and for no-array were computed and reported. Relative percentage difference maps between PET images from no-array and images from each array part were computed. PET image quality parameters were estimated for both scenarios of AC data; images reconstructed by the scanner and images reconstructed offline using e7-tools. Statistical evaluation of the resulting means used a one-factor analysis of variance (ANOVA) with ‘array’ as the

between-subject factor ( $\alpha = 0.05$ ). In the null hypothesis, no significant differences exist between all three arrays (equal means), and in the alternative hypothesis, means are significantly different with no a priori direction. The test was applied on the data from each array part (A, P and A&P) and the degree of freedom, F-factor and  $p$ -values are reported.

### 3.3 Results

This study focused on assessing each part of the novel array independently for global and regional attenuation through PET image quality indicators and compared it to the no-array data as a frame of reference. The study particularly aimed to quantify the attenuation effects of the flexible (anterior) part of the array, since registration of its AC map is typically considered a great challenge likely to be alleviated by the use of essentially PET-transparent anterior parts.

#### 3.3.1 AC maps

The NEMA-phantom is shown in figure 3-1-a, and the array under evaluation in fig. 3-1-b together with the two standard arrays fig. 3-1-c and d. Figure 3-1- e, f and h, demonstrate the in-house developed DCTAC maps for the NEMA phantom, the novel 32ch posterior, and the MRI 32ch posterior array respectively, while figure 3-1-g shows the spine-matrix AC map provided by the vendor. All posterior AC maps are shown with added patient table and NEMA phantom map which are used during PET image reconstruction on the scanner.

### 3.3.2 Global means

#### 3.3.2.1 NEMA Phantom NAC data

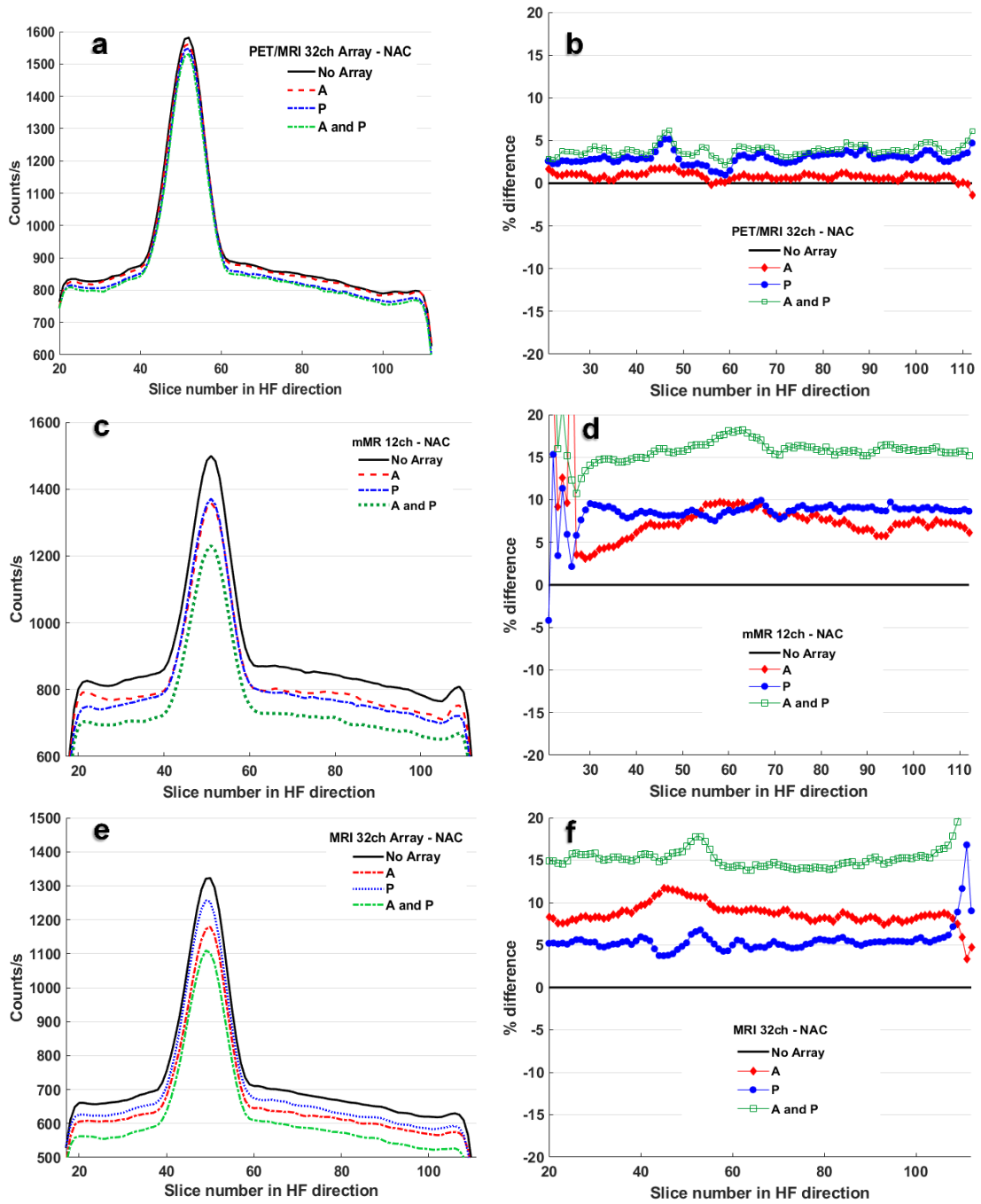
Figure 3-2- a, c and e, show the NAC data acquired for each of the three arrays PET/MRI 32ch (novel), mMR 12ch, and MRI 32ch respectively, where the decay-corrected mean of each image counts-per-second (CPS) in the z-plane are plotted, for each array parts A, P, A&P and no-array. The RPD between each part of an array and no-array are shown in figure 3-2- b, d and f. It is observed that the novel array demonstrated a steady RPD < 5% in all cases of A, P, and A&P. The RPD for both standard arrays varied between 4% and 19%. The detailed RPD of the global mean for each array and its parts are reported in table 3-1.

**Table 3-1: RPD of the global means for each case A, P, and A&P.**

		<b>A</b>	<b>P</b>	<b>A&amp;P</b>
<b>PET/MRI</b>	<i>NAC%</i>	1.9±0.6	3.0±0.7	4.3±0.7
	<i>MRAC%</i>	2.1±0.8	0.7±3.1	1.5±3.9
	<i>DCTAC%</i>	1.9±0.9	-1.8±3.5	0.0±2.5
<b>mMR</b>	<i>NAC%</i>	7.3±2.3	8.7±1.3	15.6±1.4
	<i>MRAC%</i>	4.8±0.9	10.7±3.6	13.4±3.4
	<i>DCTAC%</i>	4.6±1.2	-3.7±2.8	2.8±2.6
<b>MRI</b>	<i>NAC%</i>	8.9±1.5	5.8±2.2	15.3±1.9
	<i>MRAC%</i>	8.3±0.9	5.6±1.5	7.4±8.2
	<i>DCTAC%</i>	7.9±1.3	-2.4±3.6	9.5±2.7
<i>p-value</i>	<i>MRAC</i>	0.001	0.014	0.008
	<i>DCTAC</i>	0.001	0.050	0.121

**RPD of the global means for each case A, P, and A&P; NAC, reconstructed with MRAC and DCTAC. The negative value represents over-correction of attenuation.**

**Figure 3-2: Non attenuation correction (NAC) and relative percentage difference (RPD) plots for each array for all cases A, P, A&P.**



NAC data are shown in the left column of the figure, with plots showing as counts-per-second vs the acquisition plane number for all cases A, P, A&P and no-array. Plots are for a) the novel PET/MRI 32ch, c) the mMR 12ch, and e) the MRI 32ch arrays. The right column includes the corresponding RPD plots for each array (b, d, and f) at case A, P and A&P.

### 3.3.2.2 MRAC

In table 3-1 RPD of global means are also reported for each case of each array, where RPD for A&P-MRAC case for the novel array is estimated to be 1.5% compared to 13.4% and 7.4% for the same case with the mMR 12ch and MRI 32ch respectively.

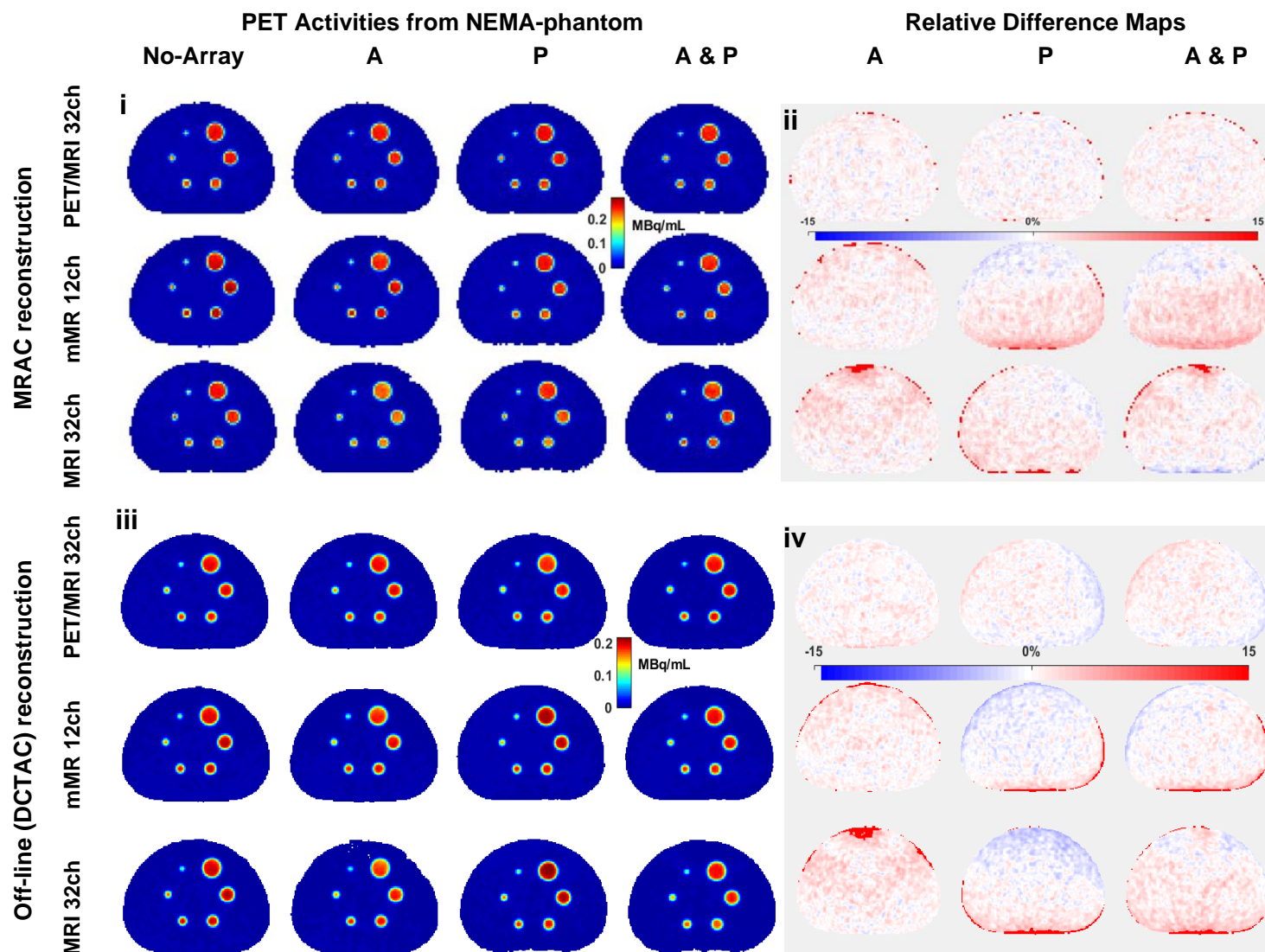
Figure 3-3-i shows the MRAC constructed PET images obtained on the NEMA-phantom with the four cases no-array, A, P, and A&P labelled for each array, all spheres are visible. In figure 3-3-ii RPD maps are shown for the three arrays, which are the results of comparing each case of an array with no-array, by means of percentage difference by pixel-by-pixel approach. In figure 3-3-ii also, the RPD from the anterior part of the novel array ranged from -0.5% to 1.0%, while the RPD from mMR 12ch and MRI 32ch ranged from -1.4% to 19.3%.

### 3.3.2.3 DCTAC

The global mean of RPD between each case vs no-array using the DCTAC reconstruction are reported in table 3-1. The RPD of global means, for both mMR 12ch and MRI 32ch, in case P, are -3.7% and -2.4% respectively, while for the novel array it is -1.8%. The A&P case for the novel array produced a global mean RPD of 0.0%, compared to 2.8% and 9.5% for the standard arrays. In figure 3-3-iii the NEMA phantom images reconstructed using the DCTAC for all cases as well as no-array with all spheres showing. Figure 3-3-iv, shows the RPD maps for all cases of each array resulted from their DCTAC data, where the lowest regional variations belong to the novel array A case. The RPD from both mMR 12ch and MRI 32ch in figure 3-3-iv, shows high regional variation in case A (close to the top of the RPD maps), which was not the case of the novel array.



Figure 3-3: Reconstructed AC images of the NEMA-phantom and RPD maps for all cases (no-array, A, P, A&P).



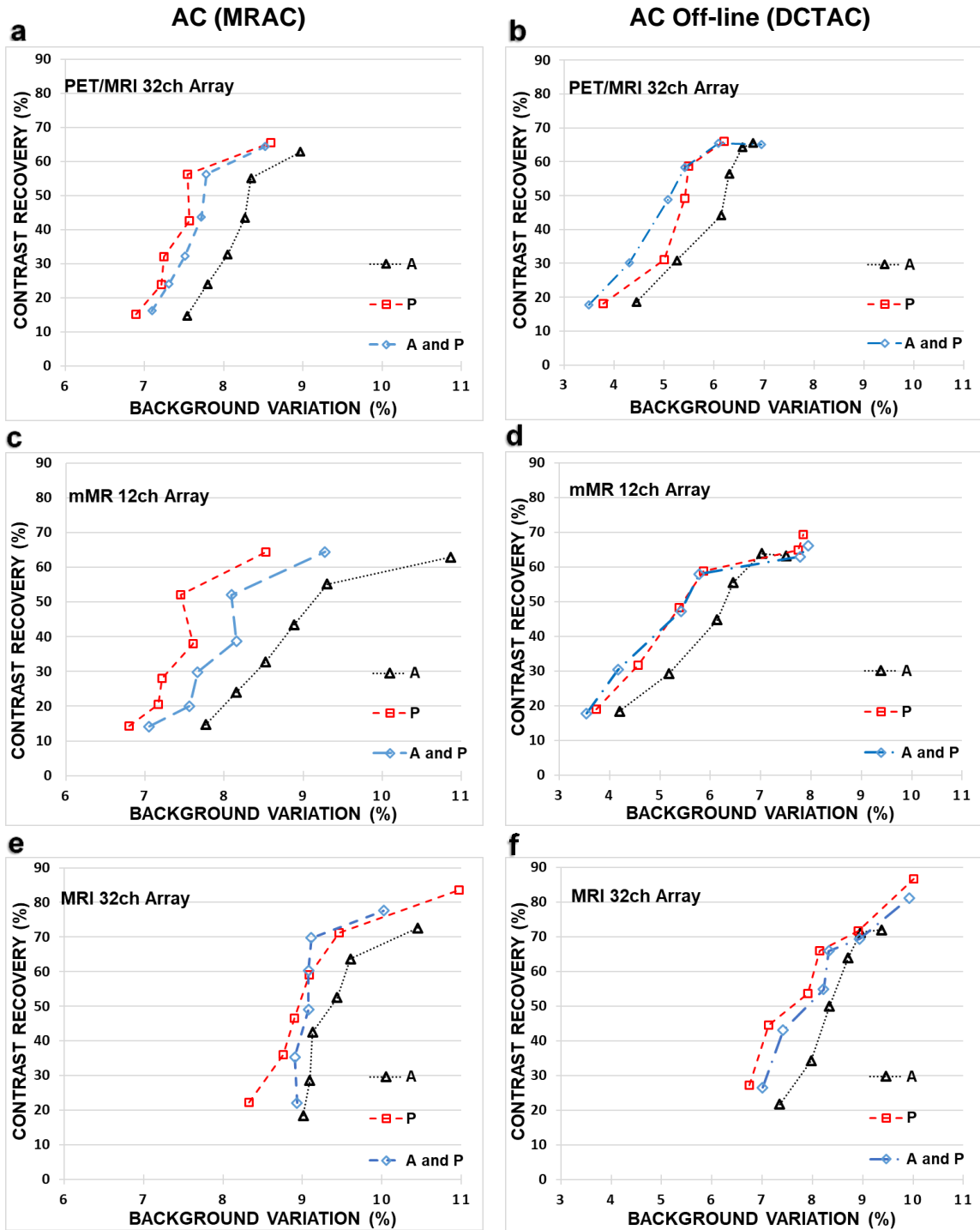
Images in (ii) and (iv) are the RPD maps corresponding to MRAC and DCTAC.

### 3.3.3 Image quality

PET image quality parameters CR and BV using the MRAC reconstructions, for each array and each case are shown in figure 3-4 – a, c and e. Background variation with the smallest range and magnitude was found in the novel array. The contrast recovery for case P of the MRI 32ch array is measured to be 83.6% for the 37mm sphere, superseding the contrast recovered by no-array for the same sphere size. From the MRAC data, the percentage of background variation for the MRI 32ch were found to be in a range between 8.3% and 9.0% for the 10mm sphere and between 10.0% and 11.0% for the 37mm sphere, which were higher compared to the novel array.

In figure 3-4-b, d, and f, the image quality parameters BV estimated from DCTAC data are plotted for all parts of the arrays. BV from the A&P case of the novel array reported to be the lowest in all data.

Figure 3-4: Contrast recovery vs. background variation (from six spheres) for each array.



The PET images for this analysis was reconstructed using both MRAC (a, c and e) and DCTAC (b, d and f).

### 3.3.4 Anterior analysis

Table 3-2 lists the relative differences between no-array contrast recovery and each array's anterior (A case) for all spheres, where the lowest RPD for sphere sizes 10mm, 22mm, and 37mm using the MRAC data, was for the novel array. The case A of the novel array recorded the lowest RPD across all sphere sizes, as seen from the DCTAC data in table 3-2.

Figure 3-5-a is a histogram combined with line plot (solid line plot) presenting the CNR from DCTAC data for case A of each array together with the no-array, as reference. The novel array anterior part is found to have the closest CNR values to the reference array for all sphere sizes. Both the MRI 32ch and the mMR 12ch surpasses, or are lower than, the no-array reference. The BV and CR from the MRAC data from case A for all sphere sizes are plotted in figure 3-5 b and c respectively. The BV produced by the novel array has recorded the closest values to the no-array data with BV ranging from 7.5% at 10mm sphere to 8.9% at 37mm sphere. Following the same pattern, the CR values were found to be the closest to no-array with range from 14.7% to 62.8%.

**Table 3-2: CR relative percentage difference between no-array and the anterior (A) part of each array for each sphere size.**

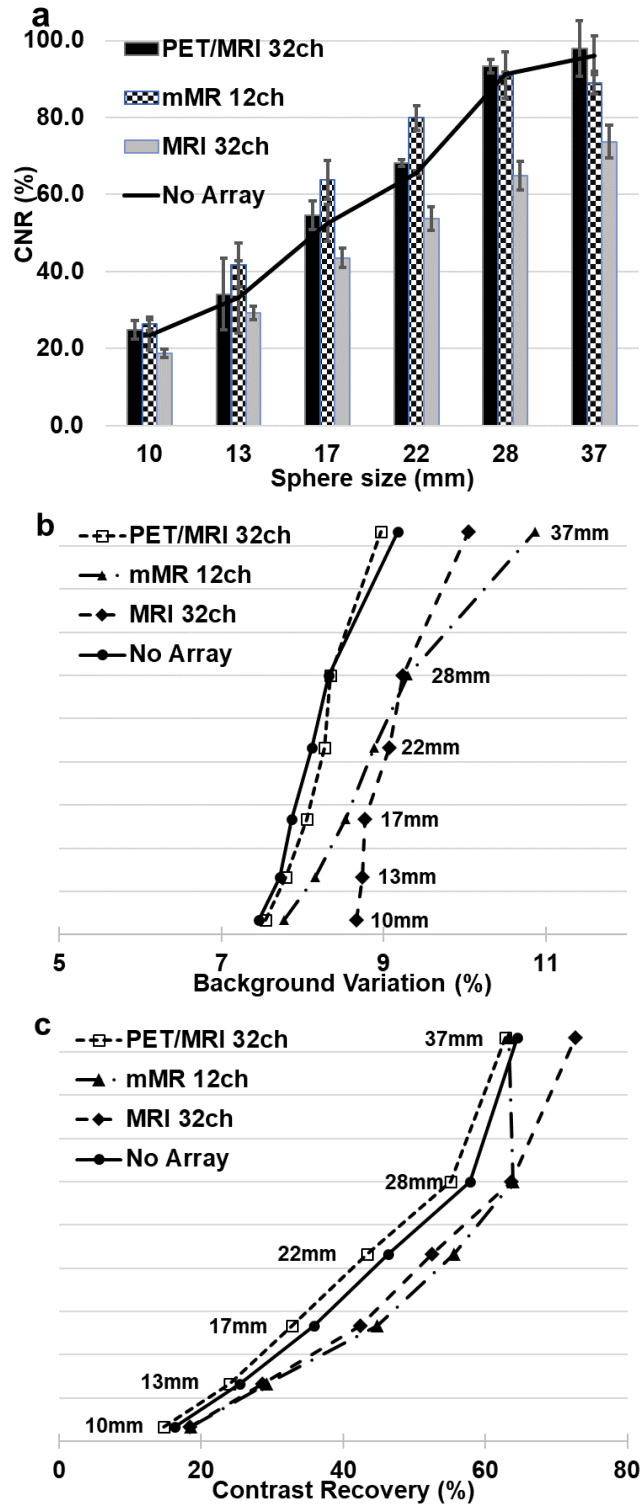
		Sphere size (mm)	10	13	17	22	28	37
MRAC	PET/MRI 32ch (%)	4.8	2.8	5.2	3.8	2.1	-1.5	
	mMR12ch (%)	15.1	2.6	-4.0	-5.4	2.0	5.2	
	MRI 32ch (%)	-20.2	-17.9	-22.7	-16.4	-13.1	-17.3	
	<i>p</i> -value	0.003	0.01	0.00	0.001	0.00	0.00	
DCTAC	PET/MRI 32ch (%)	3.8	0.9	3.6	2.0	3.7	2.4	
	mMR12ch (%)	6.0	8.0	4.1	3.5	4.2	6.6	
	MRI 32ch (%)	-10.6	-7.7	-9.5	-11.1	-6.8	-6.2	
	<i>p</i> -value	0.007	0.011	0.129	0.053	0.050	0.001	

The CR was estimated for both reconstruction methods (MRAC and off-line DCTAC).

### 3.3.5 Data analysis

Differences between mean activities for each case (A, P or A&P) of the three arrays were tested with 1x3 one-factor ANOVA using the array as a factor. For the case A&P, there was no statistically significant difference between group means as determined by one-way ANOVA ( $F(2,6) = 3.0$ ,  $p = 0.121$ ). For the cases of A and P, there were statistically significant differences between group means as determined by ANOVA ( $F(2,6) = 33.1$ ,  $p = 0.001$ ) and ( $F(2,6) = 4.2$ ,  $p = 0.050$ ) respectively.

Figure 3-5: CNR, BV and CR data for each anterior component of the three arrays are compared to no-array for all spheres.



### 3.4 Discussion

In this work, a novel array prospectively designed for hybrid PET/MRI cardiovascular imaging, was evaluated for 511keV photon attenuation. The evaluation incorporated a comparison of the novel array PET performance measuring PET image quality parameters using the NEMA NU 2-2001 Body Phantom compared to a reference measurement (no-array). The novel array's separate parts were also assessed individually and together and compared to its counterparts from two standard arrays currently used in PET/MRI cardiovascular imaging. Two different PET image reconstruction techniques (MRAC and DCTAC) were used to assess the novel array performance in the context of non-research (clinical) and research settings.

To date, research on hardware performance in PET/MRI environment, specifically RF phased arrays, have been focusing on flexible/mobile anterior part, since it is the most challenging for AC<sup>11-13</sup>. Nevertheless, in this study, all configurations/settings of the array (A, P or two parts A&P) were evaluated for each of the three arrays. This was fair since the setting for simultaneous PET/MRI cardiovascular imaging utilizes both anterior and posterior parts of an array. However, we chose not to produce DCTAC maps for the anterior part of each array, nor to apply the AC maps during PET image AC reconstruction, in order to mimic the non-research setting (clinical).

Notably, the results obtained in this study for the anterior part of both standard arrays are in agreement with previously reported results by<sup>11-13</sup>. The anterior part only of the mMR 12ch array caused overall loss of counts of 4.7% (table 3-1), and may cause up to 2.55% residual error after applying AC maps and utilizing specially developed algorithms to

reconstruct PET images off-line, as reported by<sup>11</sup>. Similarly, for the MRI 32ch anterior case, it was reported by<sup>13</sup> that loss of true counts could be as high as 10%, while regionally estimated to be as high as 22% and as-low-as 2.7% globally, after correction using CT-based AC map and using a complex algorithm off-line. Both standard arrays anterior parts affected the PET images, which is emphasised by the high values in the RPD map and are visible in (fig. 3-3, ii and iv). These effects are found to be in agreement with the results reported by<sup>12</sup>.

In this study we have shown that the novel array anterior has a superior performance ( $\leq 2\%$  RPD) with no attenuation correction maps applied, while both A&P attenuates less than 2.5% together after posterior-correction. Although no AC-map for the anterior of the novel array was used, the array had not affected the PET images, which was confirmed by RPD map homogeneity and low regional variation.

This, in comparison to its counterparts from the two standard arrays (mMR 12ch and MRI 32ch), is considered to be advantageous, in the sense that no registration is needed. Such advantage was significant ( $p=0.001$ ) for the anterior, though the A&P case for the three arrays difference was not significant ( $p=0.121$ ). At first, this may suggest that the attenuation from the complete A&P set for all arrays are not significantly different. However, upon a closer inspection AC data (fig. 3-4 d, e and f) of the P case and RPD maps (fig. 3-3 ii and iv) for both standard arrays, one notices that the AC map of the posterior parts are over correcting, which is contradicted by the underestimated attenuation caused by the anterior part. Hence, AC map of the anterior part is necessary when using the A&P set for better global attenuation estimation. Considering the background variability as a representation of PET image homogeneity, the novel array can achieve the



highest image homogeneity, since it produced the lowest BV. The BV is also a measure of statistical noise in the image confirming that the novel array causes the least noise (e.g., from inaccurate attenuation correction or poor convergence during iterative reconstruction).

### 3.5 Conclusions

This study presented the PET performance of a novel 32ch RF phased array, prospectively-designed for hybrid PET/MRI cardiovascular imaging. Although the novel array has 32 elements (almost 3 times more than the mMR 12ch), yet, we have shown that the novel array had better attenuation qualities that resulted in better PET images. The results from this study together with MRI-performance of the same array reported in<sup>18</sup> suggests its suitability for PET/MRI cardiovascular imaging. This novel array can operate without needing AC for the anterior part, simplifying the attenuation correction while at the same time improving PET image quality.

### 3.6 Acknowledgement

The authors gratefully acknowledge: Funding from MITACS (Application Ref. IT12869) (to JThé), an industry-sponsored internship (to AF) in collaboration with Multi Magnetics Inc (London, Ontario, Canada). partial salary support of AF by NSERC Discovery Grant (No. RGPIN-2016-05055) (to JThé), infrastructure support by Ontario Research Fund (RE07-021) (to FSP) and by Canada Foundation for Innovation Grant (11358) (to FSP).

The authors would like to thank Mr. John Butler, MRT for his assistance with obtaining radioactive tracers.

### 3.7 References

1. Nensa F, Bamberg F, Rischpler C, et al. Hybrid cardiac imaging using PET/MRI: a joint position statement by the European Society of Cardiovascular Radiology (ESCR) and the European Association of Nuclear Medicine (EANM). *European Journal of Hybrid Imaging*. 2018;2(1):14.
2. Catana C, van der Kouwe A, Benner T, et al. Towards Implementing an MR-based PET Attenuation Correction Method for Neurological Studies on the MR-PET Brain Prototype. *J Nucl Med*. 2010(0161-5505 (Print)).
3. Ghadiri H, Shiran MB, Ay MR, Soltanian-Zadeh H, Rahmim A, Zaidi H. A novel energy mapping approach in CT-based attenuation correction of PET data using multi-energy CT imaging. Paper presented at: 2011 IEEE Nuclear Science Symposium Conference Record; 23-29 Oct. 2011, 2011.
4. Marshall HR, Patrick J, Laidley D, et al. Description and assessment of a registration-based approach to include bones for attenuation correction of whole-body PET/MRI. *Medical physics*. 2013;40(8):082509.
5. Wagenknecht G, Kaiser H-J, Mottaghy FM, Herzog H. MRI for attenuation correction in PET: methods and challenges. *Magnetic Resonance Materials in Physics, Biology and Medicine*. 2013;26(1):99-113.
6. Kolbitsch C, Prieto C, Tsoumpas C, Schaeffter T. A 3D MR-acquisition scheme for nonrigid bulk motion correction in simultaneous PET-MR. *Medical physics*. 2014;41(8Part1):082304.

7. Huang C, Ackerman JL, Petibon Y, et al. Motion compensation for brain PET imaging using wireless MR active markers in simultaneous PET–MR: Phantom and non-human primate studies. *NeuroImage*. 2014;91:129-137.
8. Lindemann ME, Nensa F, Quick HH. Impact of improved attenuation correction on 18F-FDG PET/MR hybrid imaging of the heart. *PLoS One*. 2019;14(3):e0214095.
9. MacDonald LR, Kohlmyer S, Liu C, Lewellen TK, Kinahan PE. Effects of MR surface coils on PET quantification. *Medical physics*. 2011;38(6):2948-2956.
10. Fürst S, Souvatzoglou M, Martinez-Möller A, Nekolla S, Schwaiger M, Ziegler S. Impact of MRI surface coils on quantification in integrated PET/MR. *The Journal of Nuclear Medicine*. 2012;53(supplement 1):436.
11. Paulus DH, Braun H, Aklan B, Quick HH. Simultaneous PET/MR imaging: MR-based attenuation correction of local radiofrequency surface coils. *Medical physics*. 2012;39(7):4306-4315.
12. Kartmann R, Paulus DH, Braun H, et al. Integrated PET/MR imaging: Automatic attenuation correction of flexible RF coils. *Medical physics*. 2013;40(8):082301.
13. Eldib M, Bini J, Calcagno C, Robson PM, Mani V, Fayad ZA. Attenuation Correction for Flexible Magnetic Resonance Coils in Combined Magnetic Resonance/Positron Emission Tomography Imaging. *Investigative radiology*. 2014;49(2):63-69.
14. Eldib M, Bini J, Robson P, et al. Markerless attenuation correction for carotid MRI surface receiver coils in combined PET/MR imaging. *Physics in Medicine & Biology*. 2015;60(12):4705.

15. Patrick JC, Terry Thompson R, So A, et al. Technical Note: Comparison of megavoltage, dual-energy, and single-energy CT-based  $\mu$ -maps for a four-channel breast coil in PET/MRI. *Medical physics*. 2017;44(9):4758-4765.
16. Frohwein LJ, Heß M, Schlicher D, et al. PET attenuation correction for flexible MRI surface coils in hybrid PET/MRI using a 3D depth camera. *Physics in Medicine & Biology*. 2018;63(2):025033.
17. Eldib M, Bini J, Faul DD, Oesingmann N, Tsoumpas C, Fayad ZA. Attenuation Correction for Magnetic Resonance Coils in Combined PET/MR Imaging. *PET Clinics*. 2016;11(2):151-160.
18. Farag A, Thompson RT, Thiessen JD, Butler J, Prato FS, Théberge J. Assessment of a novel 32-channel phased array for cardiovascular hybrid PET/MRI imaging: MRI performance. *European Journal of Hybrid Imaging*. 2019;3(1):13.
19. NEMA N-NEMA. Performance Measurements of Positron Emission Tomographs, NEMA Standards Publication NU 2-2001. In: Publication NS, ed. Rosslyn, VA 22209: International and Pan American; 2001.
20. Daube-Witherspoon ME, Karp JS, Casey ME, et al. PET Performance Measurements Using the NEMA NU 2-2001 Standard. *Journal of Nuclear Medicine*. 2002;43(10):1398-1409.
21. Ziegler S, Jakoby BW, Braun H, Paulus DH, Quick HH. NEMA image quality phantom measurements and attenuation correction in integrated PET/MR hybrid imaging. *EJNMMI Physics*. 2015;2(1):18.
22. Carney JP, Townsend Dw Fau - Rappoport V, Rappoport V Fau - Bendriem B, Bendriem B. Method for transforming CT images for attenuation correction in

PET/CT imaging. *American Association of Physicists in Medicine*. 2006;33(4):976-983.

23. Comtat C, Bataille F, Michel C, et al. OSEM-3D reconstruction strategies for the ECAT HRRT. Paper presented at: IEEE Symposium Conference Record Nuclear Science 2004.; 16-22 Oct. 2004, 2004.

## Chapter 4

### 4 Improved PET/MRI accuracy by use of static transmission source in empirically-derived hardware attenuation correction.

#### 4.1 Introduction:

Hybrid positron emission tomography (PET) and magnetic resonance imaging (MRI) systems are becoming increasingly important in cardiovascular diagnostic imaging<sup>1</sup>. In cardiac PET/MRI, accurate measurement of PET activity is necessary for evaluating cardiac function<sup>2</sup> and inflammation<sup>3,4</sup>, and grading tumors based on their standardized-uptake-values (SUV)<sup>5</sup>. One aspect that affects the accuracy of PET quantification is the attenuation of photons absorbed by fixed or mobile hardware present during scans, such as RF arrays, the patient table, and headphones. The adverse effects of such hardware on PET quantifications has been reported numerously in publications; for example, the patient table of the PET/MRI system causes up to 18.7% loss of PET true-counts<sup>6</sup>, while RF resonators, for the same system, caused true-count losses varying between 3% to 14%<sup>7-13</sup>.

In addition to the patient AC map, it is necessary to include AC maps of hardware present in the PET field of view (FOV) during the scan. However, unlike patient AC maps, which can be determined using an MRI attenuation correction acquisition (MRAC)<sup>14</sup>, hardware is often invisible to MRI. To overcome such hardware attenuation, it is often required to prospectively-redesign some hardware (i.e. rigidly fixed RF arrays) for simultaneous PET/MRI, aiming to reduce their photon attenuation<sup>9</sup>. However other hardware, such as

the patient table, would be challenging to redesign, and hence techniques to correct their attenuation is still a topic of study.

In a PET-only system, the challenge of hardware AC is addressed through transmission scan that can be carried out after patient injection with the emission tracers or, simultaneously as transmission-emission scans<sup>15</sup>. In this setting, a rotating rod containing a radioactive source either emitting positrons (Ge-68/Ga-68)<sup>16</sup> or a source emitting a single photon (Cesium-137)<sup>17</sup>, is utilized to map the hardware for attenuation. Meanwhile in an integrated PET/CT system, this challenge is simpler, since hardware is visible on the CT scan, and hence, CT images can be used to map hardware attenuation. To produce CT-based AC of hardware, the CT HU are converted and scaled into LAC of PET annihilation photon energies (511keV), which are estimated by either, a bilinear transformation model from a single CT energy (140kVp)<sup>18</sup>, from a dual-energy CT to PET energy level<sup>19-22</sup>, or multi-energy CT imaging<sup>23</sup>. The bilinear model is based on different slopes for air-water ( $HU < 0$ ) and water-bone ( $HU > 0$ ). Although, the bilinear transformation model of CT-HU to PET LAC is optimized for densities ranging from air-to-bone, it is still employed in AC of hardware on PET/MRI system. This led to an attempt to improve the model and address material with high atomic number (Z) (Oehmigen et al., 2020), nevertheless the group reported general limitations when larger amounts of highly attenuating materials are to be corrected. While CT-based attenuation correction is the silver-standard for hardware AC of PET images, with CT-based AC, images still have errors up to 4.7%<sup>24</sup>. Causes of these errors invoke the use of a broad polychromatic spectrum X-ray at lower photon energies for CT image acquisition, unlike PET image acquisition, which is monochromatic. Hence, the transformation of HU to LAC at 511keV requires extensive energy mapping.



Additionally, the polychromatic X-ray in CT can cause beam hardening artefacts, especially with materials with a high atomic number (e.g. electronics found in hardware), which further degrades the measurement of accurate attenuation coefficients<sup>23</sup>.

With this in mind, TX-based AC has an advantage as an alternative to CT-based AC methods for PET/MRI systems. The transmission-based AC is based on acquiring a “blank” scan (without the hardware), and a transmission scan (with the hardware), where the ratio of the two scans, in simple terms, is the LAC. The method based on a rotating radioactive source “rod” to produce AC maps on PET and PET/CT systems has been used for decades<sup>21,25</sup>. However, it is not possible to incorporate the rotating rod into the PET/MRI system, due to complexity of the system design. Furthermore, the ability to reduce radioactive dose with MRI in PET/MRI would be diminished if a radioactive source is used to measure the tissue and hardware AC. It would also increase the scan time, which would further diminish the advantages of simultaneous PET/MRI. As an alternative to the rotating rod, liquid fluoro-deoxy-glucose (<sup>18</sup>F-FDG) was injected in an annulus-shaped phantom tube that circumfused the hardware and was used as a transmission source<sup>26</sup>. However, this alternative transmission method required more complex algorithms to allow the simultaneous reconstruction of emission and transmission data.

This study aims to propose TX-based AC using a “uniform and static” radioactive source (Ge-68 rod) for generating AC maps for hardware used in PET/MRI systems as alternative to using CT or rotating radioactive source techniques. Thus, the novelty of this study is to develop a new technique using a uniform-static source for LAC estimation of hardware like a patient table or RF arrays.

## 4.2 Materials and Methods:

### 4.2.1 Theory

The linear attenuation coefficient ( $\mu$ ) describes the fraction of photons from a monoenergetic gamma ray that is attenuated by material, per unit path length ( $l$ ). This is expressed as the ratio of the number of photons detected ( $I$ ) by the PET detector along the line of response (LOR) with the hardware in place, to the number of photons detected ( $I_0$ ) from a blank scan (without the hardware), and is described as:

$$\frac{I}{I_0} = e^{-\mu l} \quad [1]$$

In the case of a PET TX-scan of hardware for coincident detection of photon at any detector, eq (1) can be written in a discrete form of Lambert's law:

$$\frac{I}{I_0} = e^{-\sum_p \mu_{i,j}(\mathbf{p}) \cdot l_{i,j}(\mathbf{p})} \quad [2]$$

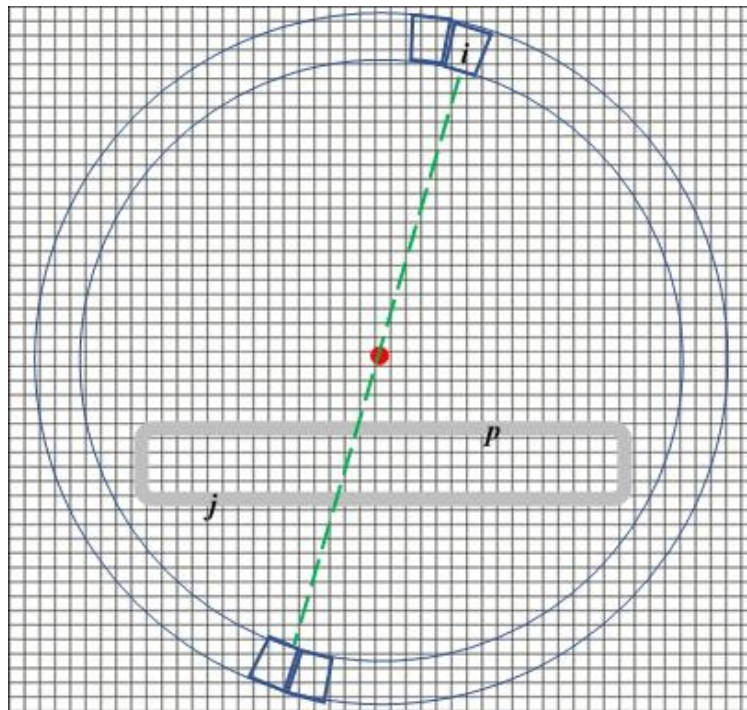
Where  $i$  is the detector index,  $j$  is the voxel index, and  $\mathbf{p}$  is the hardware voxel position in the PET FOV (figure 4-1). Since both LAC and path length are functions of position, in a PET-only scanner a rotating rod at multiple locations can provide the position of each point of the hardware, and the partial path length is known. In this study, we chose to use a known position of the radioactive source (Ge-68 rod), at the center of the bore (along x, y and z axis), this together with knowing the locations of the detectors<sup>27</sup> and 3D data profile

of the hardware, the partial path length at each point in the hardware can be calculated. Therefore, the hardware profile was registered to known voxel-size and voxel-positions, which together with the known position of the radioactive source, each position indices have a partial path length at a given LOR which can be estimated using the following relation:

$$l_{i,j} = \sum_p d_i(\mathbf{p}) \cdot b_j(\mathbf{p}) \quad [3]$$

Where  $d$  is the voxel size, and  $b = 1$  when a voxel contains a hardware profile and is otherwise equal to 0. Since position indices and partial path length projected are known, LAC can now be estimated and assigned to each voxel.

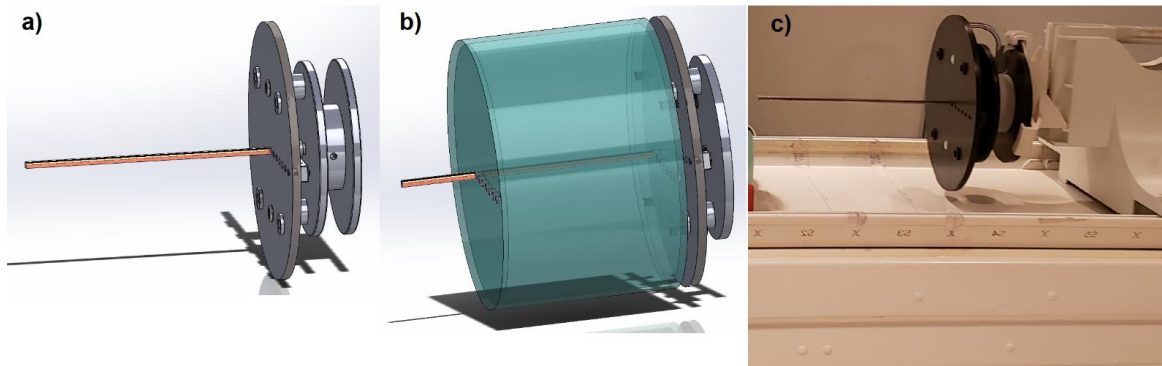
**Figure 4-1: Illustration of physical relation of hardware voxels position ( $p$ ) along a LOR and corresponds to voxel indices ( $j$ ) and detector indices ( $i$ ).**



#### 4.2.2 Acrylic cylinder and TX-fixture

In order to test the proposed method accuracy, one must confirm the LAC value measured by the method with a known theoretical LAC value of a known material. For this purpose, a phantom and a fixture to hold both the phantom (empty acrylic cylinder) and the radioactive source were reconstructed. To align the source in a known position and maintain consistent position in all scans, a fixture, namely a TX-fixture, was developed to hold the rod with better than 1mm tolerance. The TX-fixture, utilizes the vendor's daily-QC phantom holder for mounting to the table at any position. The TX-fixture was designed to hold and secure multiple or single rod (s) of Ge-68; 37 MBq; (Sanders Medical, USA), where the rod has an outer diameter of 8mm and a length of 280mm. It also permits attaching the cylinder and the rod together or each individually as seen in figure 4-2, a, b and c. Cylinder material selection criteria as an attenuation validator, included: known LAC value at 511keV, geometric symmetry, synthetic / controllable chemical contents. We chose acrylic with purity of 99.99% and known chemical composition ( $C_5O_2H_8$ ). The cylinder was hollow with the exception of a series of circular holes at its bases where the rod source was positioned. The cylinder was manufactured with; 9mm wall thickness, 210 mm length and 310mm diameter (figure 4-2-b).

**Figure 4-2: The apparatus (TX-fixture) and setting used in PET acquisitions.**



**In this figure, a) schematic of the TX-fixture showing the radioactive Ge-68 rod positioned in the center, during blank scan, b) both the acrylic cylinder phantom and the rod attached to the TX-fixture, and c) the QC-daily phantom holder securing the TX-fixture to achieve a reproducible position on the patient table.**

#### 4.2.3 TX-based AC

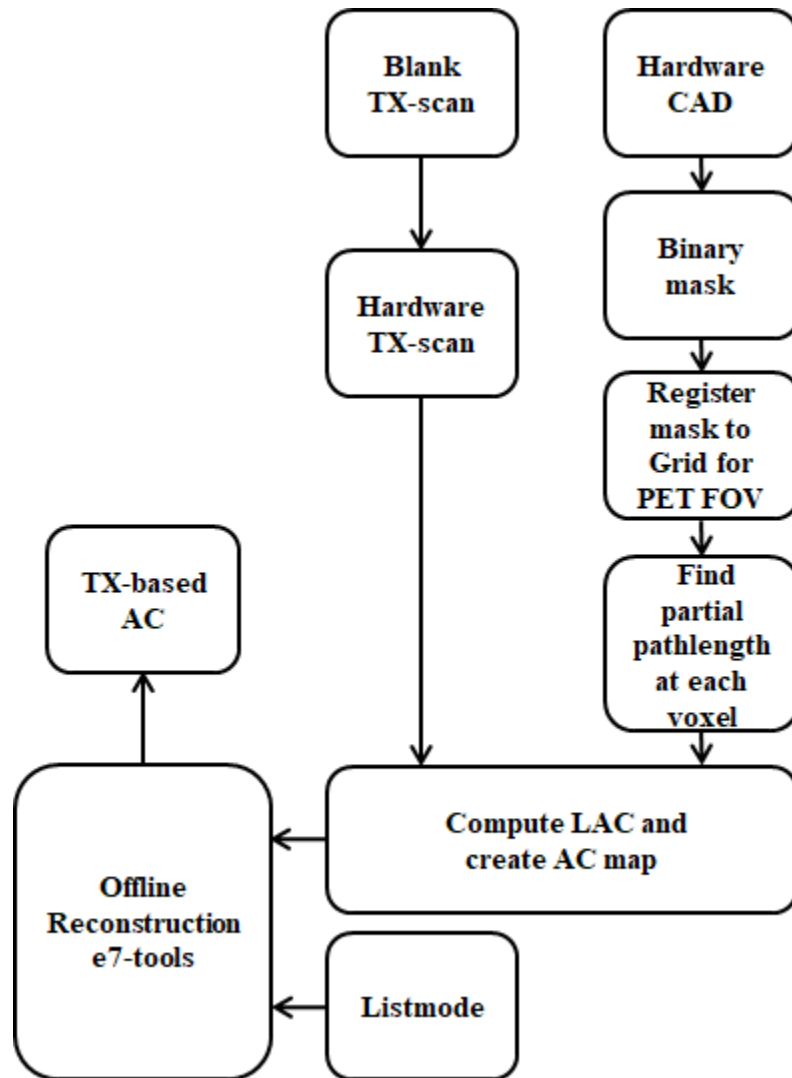
In figure 4-3 a flow chart of the steps followed to produce TX-based AC map is shown. A set of PET TX acquisitions was performed post QC-daily normalization routine on a 3.0T PET/MRI system (Biograph mMR Software Version VE11P, Siemens Healthineers, Erlangen, Germany). The TX acquisition included; 1) a blank acquisition of the rod, centered by the TX-fixture in the bore, with no-table or other hardware in the PET-FOV, therefore photon counts can be used as a reference and becomes the target to reach; 2) a TX scan with the cylinder attached to the TX-fixture with the rod in the same position as the blank TX scan. The time between the two scans, blank and with hardware, was approximately 7 min resulting to  $\sim 0.0009\%$  decay of the Ge-68 activities, and therefore decay correction was ignored. For patient MRAC, a two-point Dixon, 3D spoiled gradient sequence using, TR=4.14ms, TE=2.51ms and 1.2ms, Matrix size=240x126x127, was acquired to generate a tissue AC map with segmentation of air, lung, water, and fat. A PET

acquisition was performed for 5 minutes with matrix size 344x344x127 at a resolution of 2.09x2.09x2.02 mm<sup>3</sup>. PET reconstruction on the scanner was performed by an Ordinary Poisson Ordered Subsets Expectation Maximization (OP-OSEM) algorithm<sup>28</sup> including 3 iterations, 21 subsets, and a 4mm Gaussian filter. For derivation of the TX-based LAC of the cylinder a 3D-CAD profile was scaled to the same parameter as that of the PET acquisition and registered to image voxel. The partial path length of each voxel along the LOR to each detector was calculated from a simulated PET-FOV of the scanner geometry (8 rings each including 56 detectors at a rotating angle of  $\sim 6.4^\circ$ )<sup>27</sup>. Positioning the rod at the center of both the PET-FOV and the cylinder, allowed for symmetrical and homogeneous conditions, and therefore the distance between the source and a detector could be treated as a constant at a given plane number. Therefore, partial path lengths were assumed to be unchanged across planes for a given voxel. The resultant TX-based AC map was used with list-mode data, from the TX scan of the cylinder, to reconstruct the PET images.

Although scatter correction is not in the scope of this manuscript, however, it was assumed in this study that scatter has no dominant effect, since scatter depends on the source distribution which is homogenous in this case.

All offline PET reconstructions using TX-based AC in this study were performed using the manufacturer's offline reconstruction tool (e7-tools, Siemens Molecular Imaging, Knoxville, USA).

**Figure 4-3 Flow chart describing the process of generating hardware TX-based AC map.**



**In this process, the hardware  $\mu$ -map is generated using the PET/MRI scanner and a static radioactive source.**

#### 4.2.4 Theoretical LAC of acrylic

To verify the accuracy and validity of the TX-based LAC derived for the cylinder, we used the "un-renormalized" Scofield (1973) theoretical values of the photo-effect cross section for all elements with atomic number  $Z \geq 2$  of the acrylic chemical composition. The

analytical results used for  $Z = 1$  are the same as those used in the<sup>29</sup> compilation. LAC of acrylic was mapped at energy levels in the range between 0.1 and 1.0 MeV, where LAC was subsequently interpolated at 511 keV using 4<sup>th</sup> order polynomial fitting.

#### 4.2.5 CT-based AC

The cylinder was scanned using Dual-Energy CT (GE Healthcare, Discovery CT750 HD, Waukesha, USA), with the following parameters: tube voltage = 140 and 70 kVp; tube current = 630 mA; pitch = 0.515625 degree; FOV= 60 x 60 cm<sup>2</sup>; and exposure time = 912 seconds. The HU were converted to LAC at 511 keV using a bilinear model<sup>19</sup>. The CT-based AC map was used together with the nonattenuation-corrected (NAC) of the cylinder to reconstruct the cylinder AC images offline.

#### 4.2.6 Validation of the technique

The validation criteria of the technique were identified as the agreements of PET total photon counts and distribution between both TX-based AC of the cylinder, and the blank AC. We have selected an agreement threshold of  $\leq 1\%$ , aiming to improve attenuation accuracy over the CT-based AC method which is currently achieving (2.7%). After validating the technique, it was applied to the posterior part of the 32-channel cardiac array and the patient table.

#### 4.2.7 Posterior array

The same procedure as described above was performed to derive the hardware AC map of the posterior part of the cardiac array. However, the hardware profile was derived from a 3D-CT map<sup>9</sup>. The posterior profile was created by transforming the maps into binary values



where each voxel containing posterior information was assigned 1, otherwise 0. In this TX-scan the posterior array was placed in the bore and positioned on the patient-table rails. The targeted area, including the elements, were centered in the PET-FOV, and with this setting the TX scan of the posterior array, without the patient table, matched the location of the posterior array when used for cardiovascular imaging.

#### 4.2.8 Patient table

We chose the patient table area in this study to be centered between the S2 and S3 markings on the patient table which normally relates to the position of the elements of the spine matrix for this scanner. This allowed a consistent and match of the locations of the posterior array, table and cardiac patient during AC reconstruction using the TX-based AC maps. For this setting the daily-QC phantom holder was mounted to the patient table, with no other object present, and the TX-scan was performed as described earlier.

#### 4.2.9 In Vivo reconstruction

A patient was recruited, with written informed consent according to a research ethics protocol, approved by the Western University Health Science Research Ethics Board (HSREB) (protocol ID R-20-069). The volunteer was injected with 462MBq of  $^{18}\text{F}$ -FDG tracer for a PET/CT scan first, and then the PET/MRI scan was started 3 hours and 15 minutes later. However, none of the PET/CT data was used in this study. Simultaneously with a two-point Dixon acquisition, as described earlier, a 3D PET acquisition was performed using the same parameters as those used for the TX-scans. A set of cardiovascular MRI scans were acquired, but we report here only on two acquisitions related to this study and analysis. A 2D axial half-Fourier single-shot turbo spin-echo (HASTE) MRI was acquired using imaging parameters TR/TE = 1000ms/82ms, 20 slices,

slice thickness (ST) = 6mm, matrix = 256x154, FOV = 380x380mm and flip angle (FA) = 139°.

Positions of TX-based maps for subject, table and array were matched. This is done by acquiring the *in vivo* image at the center of a known location, between S2 and S3, same as the table and array regions used in calculating the TX-based LAC. In-vivo PET list-mode data was reconstructed offline with the TX-based AC maps for both posterior array and patient table, using the e7-tools software. The AC images produced offline were analyzed and compared to the vendor-provided, CT-based AC images produced by the PET/MRI system itself.

#### 4.2.10 Data analysis

In all analysis, hardware NAC data was compared to blank NAC data and hardware AC data was compared to blank AC data, while for in vivo imaging, TX-based AC was compared to CT-based AC. Hardware images reconstructed from the TX-based AC map were quantitatively compared to its corresponding CT-based AC images and blank images using relative percentage difference (RPD) defined voxel-wise as  $(\text{Blank}_{\text{data}} - \text{CT-based}_{\text{data}}) / \text{Blank}_{\text{data}} * 100\%$  and  $(\text{Blank}_{\text{data}} - \text{TX-based}_{\text{data}}) / \text{Blank}_{\text{data}} * 100\%$ . Furthermore, distribution of photon counts was examined using histogram analysis. In order to examine the effect of both TX-based AC and CT-based AC on cardiovascular quantification, 17-segment polar plots of short-axis PET images were produced according to the American Heart Association (AHA) standard for cardiac polar plots<sup>30</sup>. The segment values, which cover from base to apex of the heart, were compared for both AC techniques.

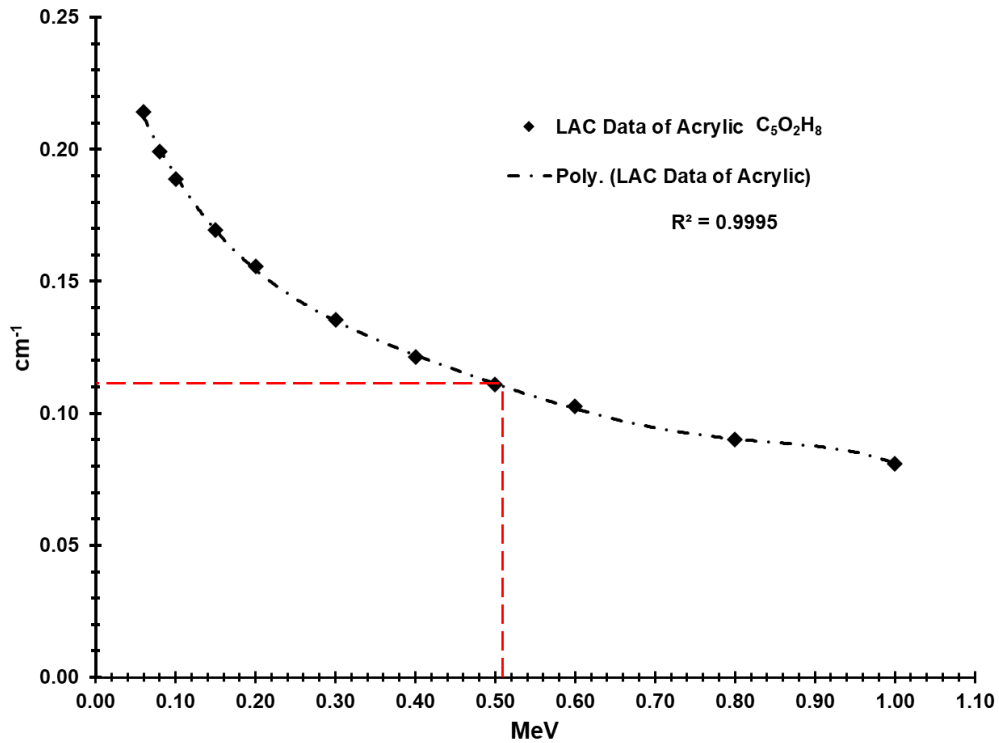
All computation of this work was performed using Matlab 9.7.0.13 (The MathWorks, Natick, MA, USA).

## 4.3 Results and discussion:

### 4.3.1 TX-based AC map and validation of LAC

The TX-based procedure described in this work produced an AC map of the cylinder material with an average LAC of  $0.10851 \pm 0.00380 \text{ cm}^{-1}$ . The theoretical Z-based LAC derived from the chemical composition of acrylic described by<sup>29</sup> was estimated to be  $0.10698 \pm 0.00321 \text{ cm}^{-1}$ . The coefficient of determination of the fitted 4<sup>th</sup> order polynomial function is calculated to be  $R^2 = 0.9995$ . The percentage difference between the theoretically derived LAC and measured LAC, using TX-based technique, was found to be  $1.3 \pm 0.3\%$  which was not statistically significantly different ( $p=0.7060$ ).

**Figure 4-4: Theoretical estimation of acrylic material from mapped LAC values from 0.1 to 1.0 MeV.**



**The fitted model ( $R^2=99.95\%$ ) produced LAC of acrylic at 511keV = 0.10698 cm-1 as indicated with the red dashed lines.**

#### 4.3.2 TX-based AC, and CT-based AC for hardware

Figure 4-5 shows the line profiles, from the center of the PET image resulted from scanning the Ge-68 rod with and without different hardware in the PET-FOV. The line profiles are arranged in three clusters, each is related to the hardware under examination and includes a line profile for NAC PET and two-line profiles for AC PET reconstructed with TX-based and CT-based methods. The cylinder scans produced the line profile seen in figure 4-5-a and represents NAC PET, the TX-based AC PET reconstructed offline and, CT-based AC PET (produced by the CT scanner in a separate CT scan of the cylinder), respectively. The

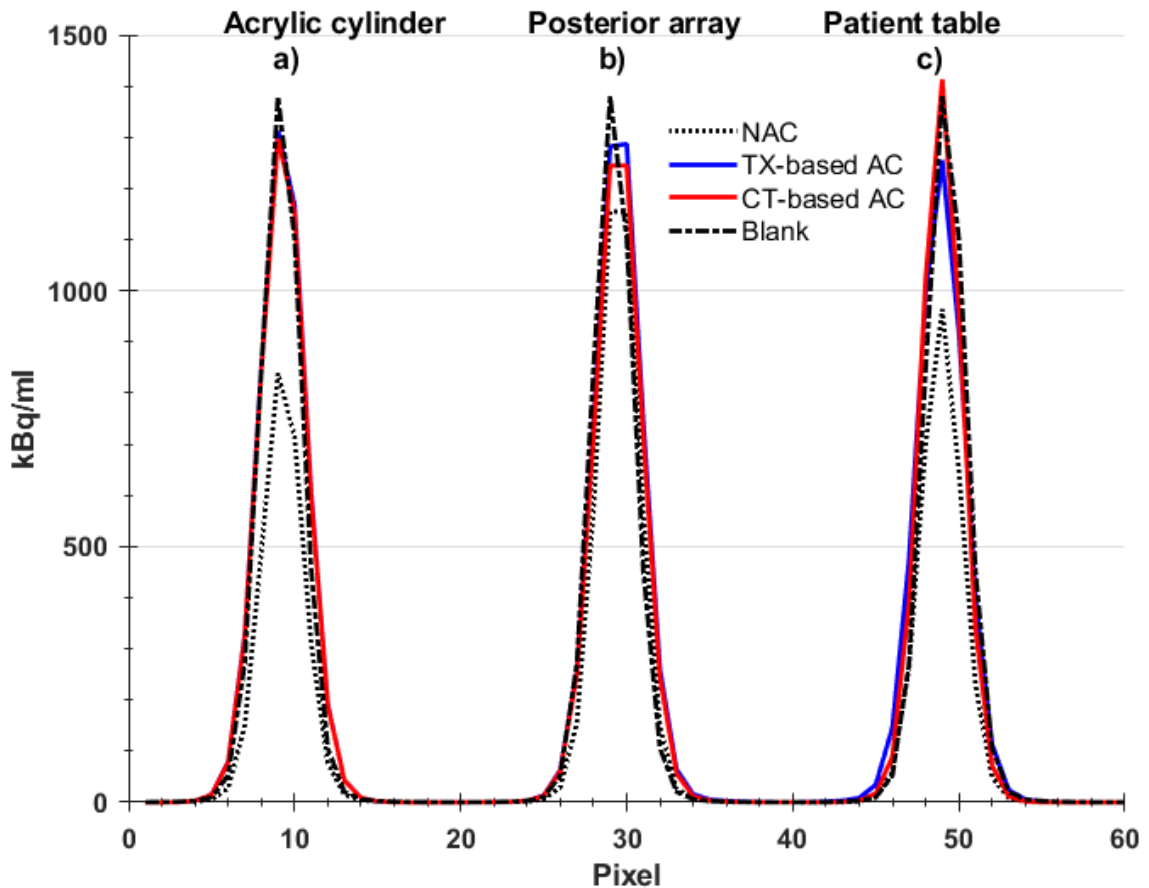
RPD values comparing the two AC PET reconstructions are reported in table 4-1, where TX-based AC PET mean and standard deviation (std) was different from blank by  $0.4 \pm 1.4$  %, while the RPD of mean values in the case of CT-based AC was  $-1.9 \pm 0.8$  %.

Figure 4-5-b, shows the NAC and both AC PET line profiles from the posterior array results using the TX and the CT-based AC correction. As reported in table 4-1, the TX-based AC map, for posterior array, produced PET images with RPD of  $0.5 \pm 1.5$ %, while, CT-based AC produced RPD of  $0.7 \pm 0.5$ %. The posterior array was estimated to attenuate about  $1.6 \pm 0.6$ % comparing between NAC of the posterior array and the NAC of blank. In figure 4-5-c, the results from the patient table are showing the NAC data compared to both AC techniques. Table 4-1, reported the RPD value between the NAC PET of the patient table, and the NAC PET of the blank, which was found to be  $8.7 \pm 1.2$ %, which is consistent with what has been reported earlier<sup>6</sup>. For the patient table TX-based AC reported to produce global mean RPD of  $-0.7 \pm 1.4$ % while for the CT-based AC the RPD was  $-4.3 \pm 1.3$ %.

In general, figure 4-6 shows both quantitative and qualitative analysis of both TX-based and CT-based AC PET data and comparison to blank data. In figure 4-6 (a, c, and e) the RPD, between blank images and its corresponding images of each AC technique or NAC, are displayed for each transaxial plane number. In figure 4-6 (b, d, and f) the distribution of photon counts per second and their frequency for each hardware; acrylic cylinder, posterior array and patient table, respectively, are shown by histogram plot. Notably, the CT-based AC PET distribution displays more frequent counts per second at lower values, over TX-based AC PET. Likewise, the distribution of TX-based AC PET is closer to those produced from blank in the case of the patient table, although this might not be apparent (fig. 4-6-f), as the dashed red line belonging to CT-based plot are only covered by the

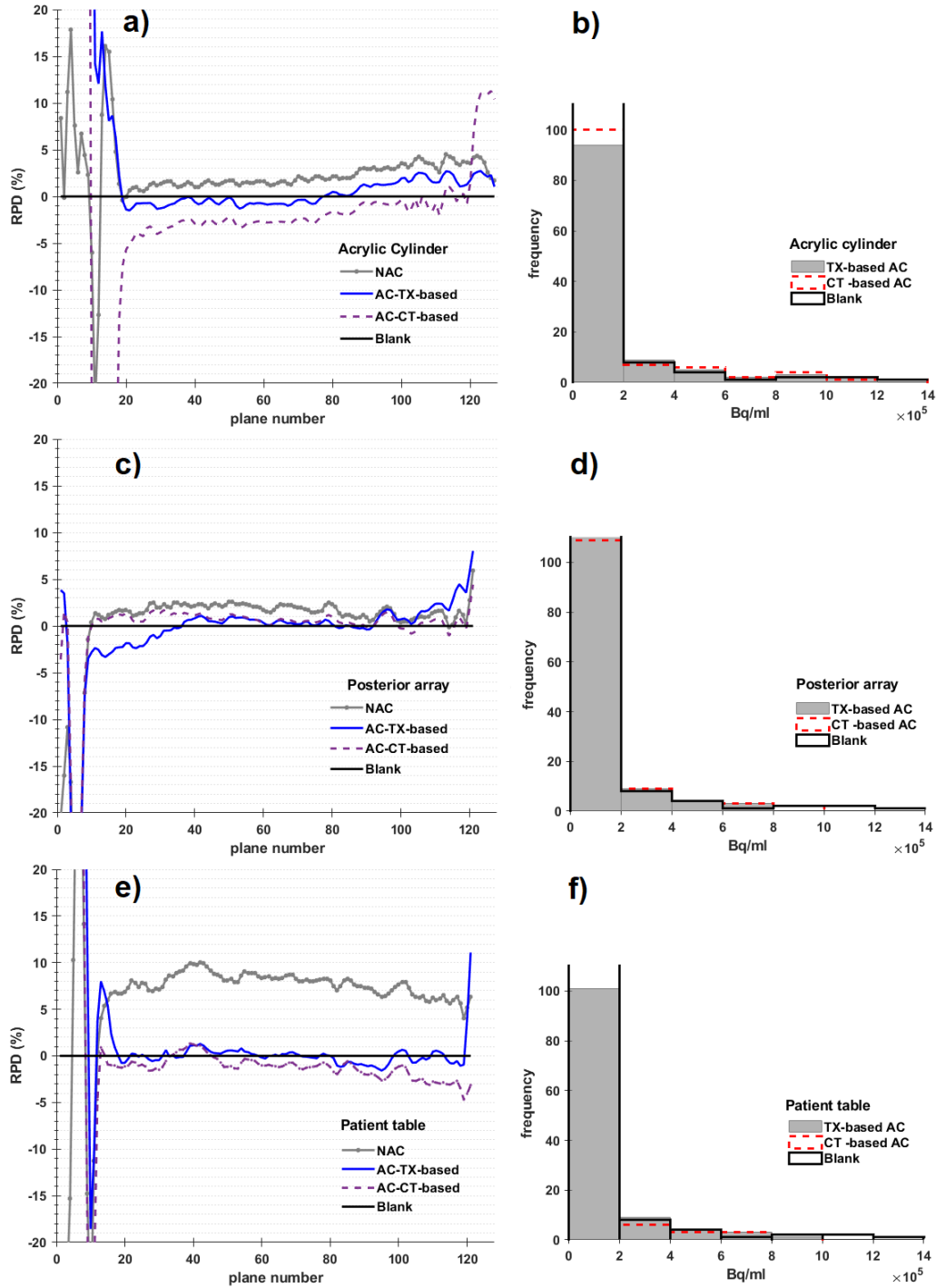
black lines of the blank data. The percentage mean difference between AC and NAC blank were estimated to be in the range of 11 to 18%.

**Figure 4-5: Line plot of a profile from pixels centred on the PET image for the three-hardware.**



For the three-hardware configurations examined in this study, left line plot results from acrylic cylinder with NAC PET, TX-based AC PET, CT-based AC PET, and blank (black-dashed line). The same order of plots is repeated for the posterior array and patient table respectively.

**Figure 4-6: RPD of NAC, TX-based AC and CT-based AC PET images for the hardware under examination.**



The RPD of NAC, TX-based AC and CT-based AC PET images for the acrylic cylinder, posterior array, and patient table are shown in (a), (c) and (e)) respectively, compared to blank. Distribution of photon counts are displayed in histograms in (b), (d) and (f)) comparing TX-based AC to CT-based AC and blank

**Table 4-1: Relative percentage difference for non-corrected and corrected images of hardware for TX-based AC and CT-based AC methods.**

	<i>NAC</i>	<i>TX-based AC</i>	<i>CT-based AC</i>	<i>TX-to-CT</i>
	mean $\pm$ std	mean $\pm$ std	mean $\pm$ std	mean $\pm$ std
<i>Acrylic Cylinder</i>	2.2 $\pm$ 1.1	0.4 $\pm$ 1.4	-1.9 $\pm$ 0.8	-
<i>Posterior array</i>	1.6 $\pm$ 0.6	0.5 $\pm$ 1.5	0.7 $\pm$ 0.5	-
<i>Patient table (S2-S3)</i>	8.7 $\pm$ 1.2	-0.7 $\pm$ 1.4	-4.3 $\pm$ 1.3	-
<i>In-vivo</i>	-	-	-	4.1 $\pm$ 0.9

**RPD for NAC and AC images of hardware scan to NAC and AC image of blank scan. In-vivo data from TX-based AC and CT-based AC are compared.**

### 4.3.3 In-Vivo data

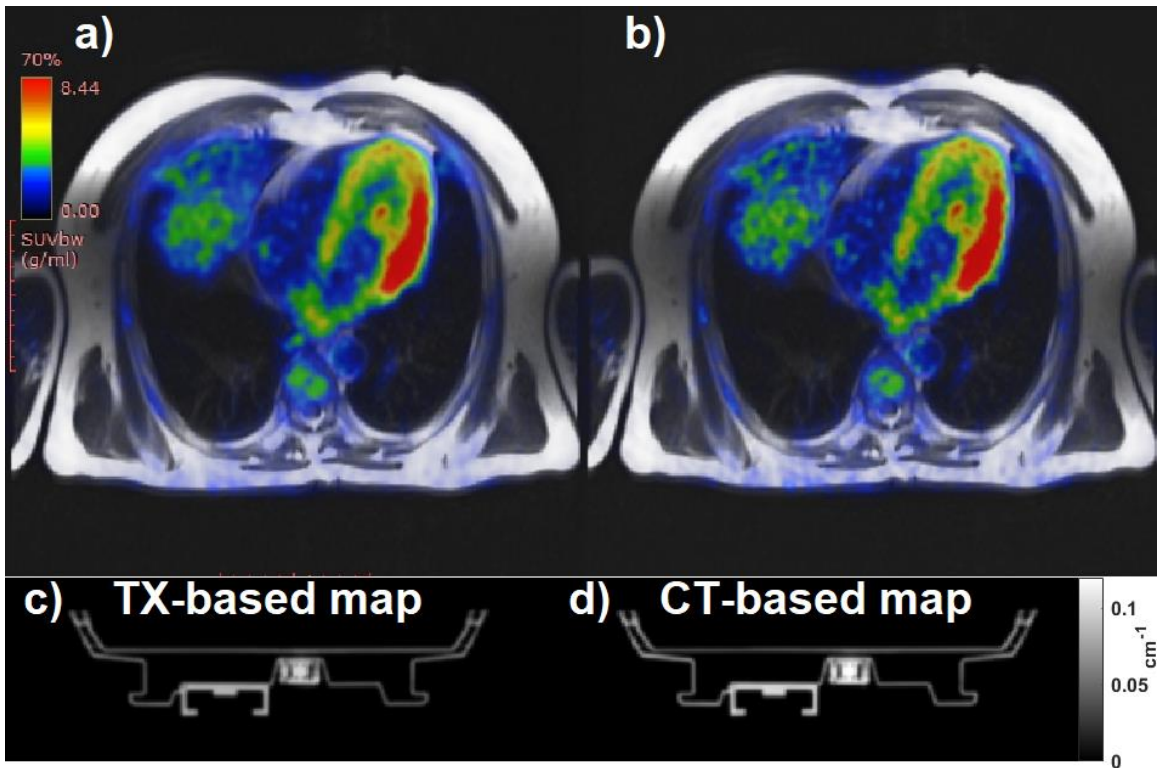
The AC PET images reported here are products of reconstruction with hardware AC maps (posterior array and patient table) and the patient MRAC map determined by segmentation of fat/water Dixon MRI. Both PET and 2D-HASTE MRI images are fused in figure 4-7, using hardware TX-based AC (fig. 4-7-a) and CT-based AC (fig. 4-7-b). The CT-based AC map and TX-based AC map of the patient table are displayed with the same scale in figure 4-7 (a and b), respectively. In figure 4-8-a, the RPD map produced from both CT-based and TX-based PET data shows higher RPD values towards the posterior region. The RPD between the TX-based and CT-based maps is displayed in figure 4-8-b.

In figure 4-9, a polar plot of the LV PET images is shown for TX-based AC (fig. 4-9-a) and CT-based AC (fig. 4-9-b), respectively. We estimated the difference between CT-



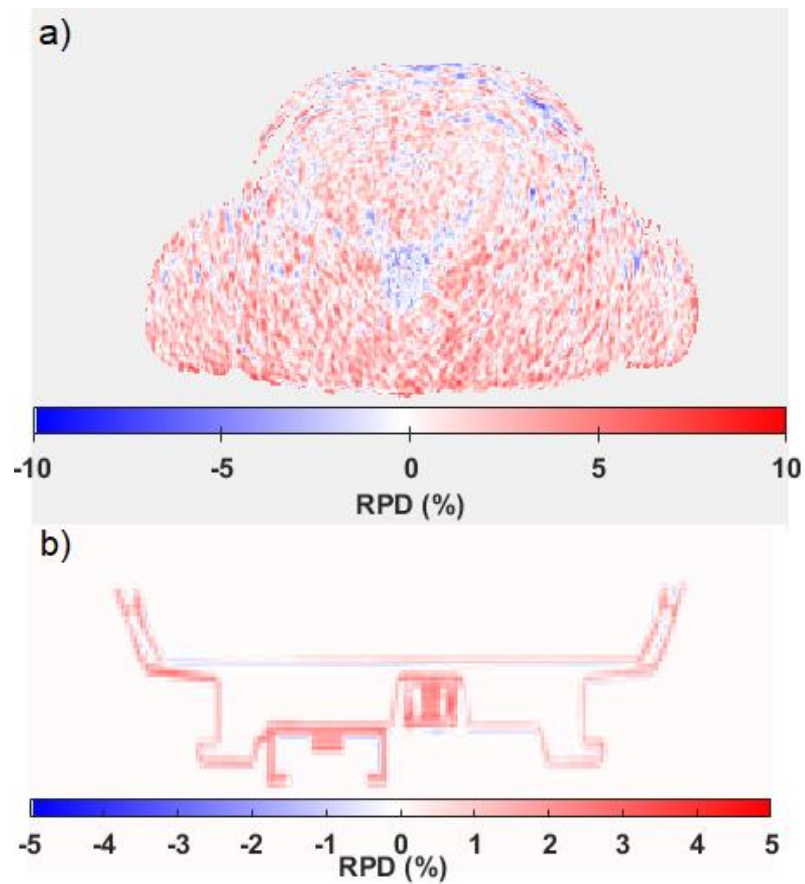
based and TX-based attenuation-corrected PET images for the following regions: Apex, Apical, Mid and Basal which are represented by the four circles of the polar plot, from inward to outward, respectively. The RPDs for these regions were Apex  $-3.1 \pm 1.2\%$ , Apical  $1.5 \pm 1.1\%$ , Mid  $-3.4 \pm 1.0\%$  and Basal  $1.2 \pm 1.1\%$ .

**Figure 4-7: Fused images of  $^1\text{H}/\text{FDG}$  for a volunteer, using TX-based and CT-based  $\mu$ -maps of the patient table.**



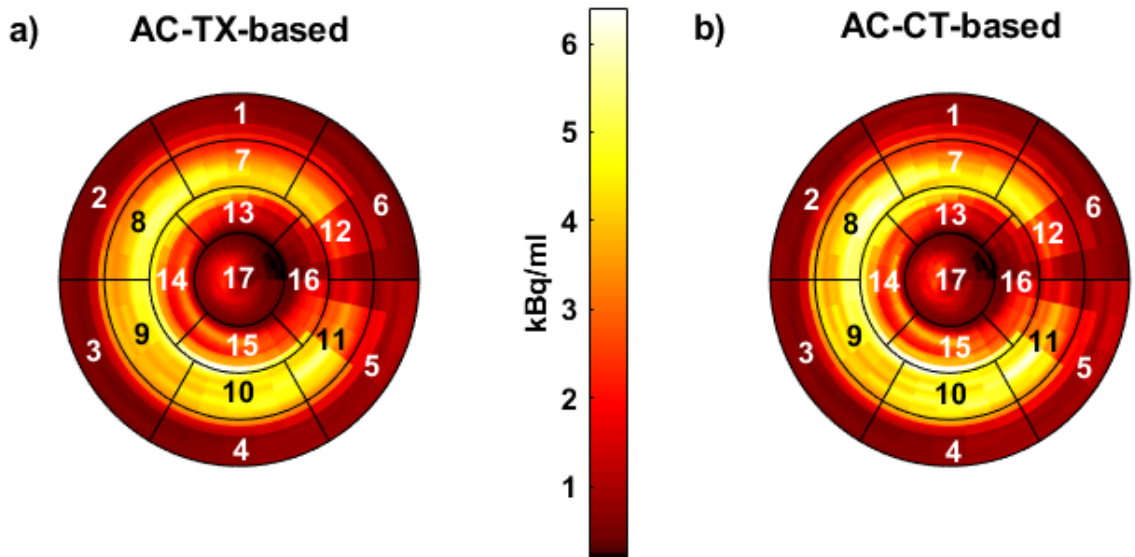
Above, the fused images (a and b top) of the 2D-HASTE MRI to  $^{18}\text{F}$ -FDG PET for a volunteer. a) is the offline reconstructed PET with the scanner using hardware TX-based maps (both, patient table and posterior part of the array), while b) is for the same PET data, reconstructed using hardware CT-based maps. The lower row of the figure (c and d), shows respectively, the TX-based and the CT-based maps of the patient table

**Figure 4-8: RPD map of in vivo PET data resulted from comparing TX-based AC to CT-based AC and RPD map of the hardware AC maps.**



**RPD map resulted from comparing in-vivo images reconstructed using TX-based AC to CT-based AC shown in figure 4-7 (a, b); b) is the RPD map of the hardware AC maps displayed in figure 4-7 (c, d).**

**Figure 4-9: Polar plot of 17-segment for the LV short-axis of the heart, using TX-based AC and, CT-based AC.**



#### 4.4 Discussion:

Hardware attenuation correction based on PET transmission scans, is well established and was applied using the PET/MRI scanner with two different techniques<sup>31,32</sup>. The technique reported by Kawaguchi et al. was for the brain and it was not applied to hardware. The group suggested the need for additional techniques to incorporate MR-invisible hardware. Additionally, tissue segmentation was an issue in Kawaguchi's work due to the three unknowns of tissue textures in the formulation. Another TX-based technique was performed by<sup>32</sup> using a fixed radioactive source (Ge-68 cylinder) where they reported improved of AC of the patient table from 4.5% (CT-based AC) to 2.7% (TX-based). Their technique considered derivation of the LAC from two-point projection but they used a non-uniform TX source.

In this work, we utilized Lambert's law, as a technique to estimate LAC at 511keV of acrylic material with known theoretical value of LAC for validation. We simplified the technique by providing a uniform source (Ge-68 rod), the hardware profile, its voxel position and estimated partial path length which was used in LAC estimation. The TX-based method described here, was used to estimate AC maps for the posterior part of a phased array RF coil, and the patient table, at the regions used for simultaneous PET/MRI cardiac imaging. The maps produced from the TX-based technique were used, instead of CT-based AC, to reconstruct PET images of a volunteer offline. TX-based AC and CT-based AC for hardware has shown that PET images resulted from TX-based AC differed by less than 1% compared to the blank "truth" for all hardware cases.

The hardware used for TX-based AC was homogeneous enough, density-wise, to consider the formulation for only one unknown, which might not be the case for hardware that has larger areas with multiple densities. This technique also requires the knowledge of the hardware position and profile and hence it is effective for fixed hardware, but might not be as effective for mobile/flexible hardware.

The coefficient of determination of the polynomial fit ( $R^2=0.9995$ ) provides confidence in the interpolated LAC value derived from mapped energies, while the RPD between the theoretical and TX-based measured LACs validated both the acrylic cylinder attenuation coefficient and, the technique for further work. The difference between NAC and AC from the blank PET image suggests that the AC procedure performed on the NAC data, compensates for scatter corrected AC PET verses non-scatter corrected NAC PET. We also considered that the difference might represent the scatter and attenuation errors estimated

by the system. Therefore, the AC data of the blank was the baseline that we used in the analysis and for comparison.

It is worth noting here that both partial volume effect and positron long range of the Ge-68, have no effect on the results. Since both effects are more observed within tissues, while the derived LAC from TX-based depends on the number of LOR crossing the voxels of the hardware AC map rather than on imaging pixels within the rod itself.

The negative RPD value between the blank and the acrylic CT-based AC images indicates overcorrection of the CT-based AC compared to the TX-based AC. This also suggests that CT-based AC of patient table is inaccurate compared to AC PET data from the blank scan. The more frequent counts observed at lower value in figure 4-6 (b, d, and f) may be interpreted as increased scattering artifacts, which may also explain the overcorrecting behavior by CT-based AC for hardware that is previously reported in the literature <sup>6</sup>. Meanwhile, the RPD resulting from the comparison of in-vivo PET images reconstructed by both methods, suggests that CT-based AC is less accurate than the TX-based AC, which is quantified by mean RPD of  $4.1 \pm 0.9\%$  and reported in table 4-1.

Although this work targeted a specific region of the patient table used in cardiac imaging, the technique can be employed to produce an AC map for the entire table, or other targeted regions of the body. In our future work we will be reporting on the development of an AC map for the full table.

## 4.5 Conclusion:

The TX-based AC technique described in this study resulted in similar or improved attenuation corrected PET images compared to CT-based AC. All TX-based AC produced mean RPD of <1%, when compared to blank data. Although the cardiac results from a patient reported here are encouraging, with changes in RPD of in-vivo PET matching the improvements observed in phantom, more patients / volunteers would benefit statistical analysis. The AC maps results from the three different types of hardware demonstrated a consistent result, that is, the current CT-based AC for hardware using a bilinear model is modestly inaccurate.

Here, we have shown that the generation of TX-based AC maps using a static radioactive source and the PET/MRI system itself, for fixed hardware, is feasible. The strength of this work is that the technique allows PET and PET/MRI research sites, where access to CT or PET/CT systems is limited, to still produce highly accurate AC maps for their hardware. The TX-based hardware AC map generated using the PET/MRI system also reduces time and effort in comparison to using CT or PET/CT systems to generate hardware AC maps.

## 4.6 Acknowledgments:

The authors gratefully acknowledge: Dr. Udunna Anazodo for utilizing the PET data acquired under protocol ID 6319. The authors also thank Ms. Chantelle Graf for recruiting the patient, and both Mr. John Butler and Ms. Heather Biernaski for performing patient PET/MRI scan. The authors also acknowledge: Funding from MITACS (Application Ref.

IT12869) (to JThé), an industry-sponsored internship (to AF) in collaboration with Multi Magnetics Inc (London, Ontario, Canada). Partial salary support of AF by NSERC Discovery Grant (No. RGPIN-2016-05055) (to JThé), infrastructure support by Ontario Research Fund (RE07-021) (to FSP) and by Canada Foundation for Innovation Grant (11358) (to FSP).

## 4.7 Reference

1. Nensa F, Bamberg F, Rischpler C, et al. Hybrid cardiac imaging using PET/MRI: a joint position statement by the European Society of Cardiovascular Radiology (ESCR) and the European Association of Nuclear Medicine (EANM). *European Journal of Hybrid Imaging*. 2018;2(1):14.
2. O' Doherty J, Chalampalakis Z, Schleyer P, Nazir MS, Chiribiri A, Marsden PK. The effect of high count rates on cardiac perfusion quantification in a simultaneous PET-MR system using a cardiac perfusion phantom. *EJNMMI Physics*. 2017;4(1):31.
3. Wisenberg G, Thiessen J, Pavlovsky W, Butler J, Wilk B, Prato F. Same day comparison of PET/CT and PET/MR in patients with cardiac sarcoidosis. *Journal of Nuclear Cardiology*. 2019:1-12.
4. Wilk B, Wisenberg G, Dharmakumar R, Thiessen JD, Goldhawk DE, Prato FS. Hybrid PET/MR imaging in myocardial inflammation post-myocardial infarction. *Journal of Nuclear Cardiology*. 2019.

5. Lindemann ME, Guberina N, Wetter A, Fendler W, Jakoby B, Quick HH. Improving 68-Ga-PSMA PET/MR hybrid imaging of the prostate with unrenormalized absolute scatter correction. *Journal of Nuclear Medicine*. 2019.
6. Fürst S, Souvatzoglou M, Martinez-Möller A, Schwaiger M, Nekolla SG, Ziegler SI. Impact of flexible body surface coil and patient table on PET quantification and image quality in integrated PET/MR. *Nuklearmedizin, Georg Thieme Verlag KG*. 2014;53(03): 79-87.
7. Aklan B, Paulus DH, Wenkel E, et al. Toward simultaneous PET/MR breast imaging: Systematic evaluation and integration of a radiofrequency breast coil. *Medical physics*. 2013;40(2):024301.
8. Dregely I, Lanz T, Metz S, et al. A 16-channel MR coil for simultaneous PET/MR imaging in breast cancer. *European Society of Radiology*. 2014;25:1154–1161.
9. Farag A, Thompson RT, Thiessen JD, Biernaski H, Prato FS, Théberge J. Evaluation of 511 keV photon attenuation by a novel 32-channel phased array prospectively designed for cardiovascular hybrid PET/MRI imaging. *European Journal of Hybrid Imaging*. 2020;4(1):7.
10. Kartmann R, Paulus DH, Braun H, et al. Integrated PET/MR imaging: Automatic attenuation correction of flexible RF coils. *Medical physics*. 2013;40(8):082301.
11. MacDonald LR, Kohlmyer S, Liu C, Lewellen TK, Kinahan PE. Effects of MR surface coils on PET quantification. *Medical physics*. 2011;38(6):2948-2956.
12. Paulus DH, Braun H, Aklan B, Quick HH. Simultaneous PET/MR imaging: MR-based attenuation correction of local radiofrequency surface coils. *Medical physics*. 2012;39(7):4306-4315.



13. Tellmann L, Quick H, Bockisch A, Herzog H, Beyer T. The effect of MR surface coils on PET quantification in whole-body PET/MR: results from a pseudo-PET/MR phantom study. *Medical physics*. 2011;38(5):2795-2805.
14. Galldiks N, Langen K-J. Amino acid PET in neuro-oncology: applications in the clinic. In: Taylor & Francis; 2017.
15. Bailey DL. Transmission scanning in emission tomography. *European Journal of Nuclear Medicine*. 1998;25(7):774-787.
16. Carroll LR, Kretz P, G. O. The orbiting rod source: improving performance in PET transmission correction scans. *New York: Society of Nuclear Medicine*. 1983(In: Esser PD, ed. Emission computed tomography – current trends.):235–247.
17. deKemp RA, Nahmias C. Attenuation correction in PET using single photon transmission measurement. *Medical physics*. 1994;21(6):771-778.
18. Burger C, Goerres G, Schoenes S, Buck A, Lonn A, von Schulthess G. PET attenuation coefficients from CT images: experimental evaluation of the transformation of CT into PET 511-keV attenuation coefficients. *Eur J Nucl Med Mol Imag*. 2002;29(7):922-927.
19. Carney JP, Townsend Dw Fau - Rappoport V, Rappoport V Fau - Bendriem B, Bendriem B. Method for transforming CT images for attenuation correction in PET/CT imaging. *American Association of Physicists in Medicine*. 2006;33(4):976-983.
20. Guy MJ, Castellano-Smith IA, Flower MA, Flux GD, Ott RJ, Visvikis D. DETECT-dual energy transmission estimation CT-for improved attenuation correction in SPECT and PET. *IEEE Transactions on Nuclear Science*. 1998;45(3):1261-1267.

21. Kinahan PE, Townsend DW, Beyer T, Sashin D. Attenuation correction for a combined 3D PET/CT scanner. *Medical physics*. 1998;25(10):2046-2053.
22. Patrick JC, Terry Thompson R, So A, et al. Technical Note: Comparison of megavoltage, dual-energy, and single-energy CT-based  $\mu$ -maps for a four-channel breast coil in PET/MRI. *Medical physics*. 2017;44(9):4758-4765.
23. Ghadiri H, Shiran MB, Ay MR, Soltanian-Zadeh H, Rahmim A, Zaidi H. A novel energy mapping approach in CT-based attenuation correction of PET data using multi-energy CT imaging. Paper presented at: 2011 IEEE Nuclear Science Symposium Conference Record; 23-29 Oct. 2011, 2011.
24. Shirmohammad M, Ay MR, Sarkar S, Ghadiri H, Rahmim A. Comparative assessment of different energy mapping methods for generation of 511-keV attenuation map from CT images in PET/CT systems: A phantom study. Paper presented at: 2008 5th IEEE International Symposium on Biomedical Imaging: From Nano to Macro; 14-17 May 2008, 2008.
25. Witoszynskij S, Andrzejewski P, Georg D, et al. Attenuation correction of a flat table top for radiation therapy in hybrid PET/MR using CT- and  $^{68}\text{Ge}/^{68}\text{Ga}$  transmission scan-based  $\mu$ -maps. *Physica Medica*. 2019;65:76-83.
26. Mollet P, Keereman V, Bini J, Izquierdo-Garcia D, Fayad ZA, Vandenberghe S. Improvement of Attenuation Correction in Time-of-Flight PET/MR Imaging with a Positron-Emitting Source. *Journal of Nuclear Medicine*. 2014;55(2):329-336.
27. Aklan B, Oehmigen M, Beiderwellen K, et al. Impact of Point-Spread Function Modeling on PET Image Quality in Integrated PET/MR Hybrid Imaging. *Journal of Nuclear Medicine*. 2016;57(1):78-84.

28. Comtat C, Bataille F, Michel C, et al. OSEM-3D reconstruction strategies for the ECAT HRRT. Paper presented at: IEEE Symposium Conference Record Nuclear Science 2004.; 16-22 Oct. 2004, 2004.
29. Hubbell JH. Tables of X-ray mass attenuation coefficients and mass energy-absorption coefficients from 1 keV to 20 MeV for elements Z=1 to 92 and 48 additional substances of dosimetric interest. <http://www.nist.gov/pml/data/xraycoef/index.cfm>. 1982.
30. Cerqueira MD, Weissman NJ, Dilsizian V, et al. Standardized Myocardial Segmentation and Nomenclature for Tomographic Imaging of the Heart. *Circulation*. 2002;105(4):539-542.
31. Kawaguchi H, Hirano Y, Yoshida E, et al. A proposal for PET/MRI attenuation correction with  $\mu$ -values measured using a fixed-position radiation source and MRI segmentation. *Nuclear Instruments and Methods in Physics Research Section A: Accelerators, Spectrometers, Detectors and Associated Equipment*. 2014;734:156-161.
32. Xie H, Zhao J, Dong Y, Lv Y. Attenuation Correction for Fixed MR Components in a Simultaneous PET/MR System. Paper presented at: 2017 IEEE Nuclear Science Symposium and Medical Imaging Conference (NSS/MIC); 21-28 Oct. 2017, 2017

## Chapter 5

### 5 Conclusion and future work

#### 5.1 Summary

The overall goal of the thesis was to improve sensitivity and quantitative accuracy of cardiac PET when PET data is collected simultaneously with the whole-body hybrid PET/MRI imaging system. An important point is that this is to be achieved without diminishing the performance of the MRI. To achieve this, three objectives were formulated which were realized using two novel “inventions”, the three objectives are:

- a) Objective 1: characterize a high-density RF phased array with MRI performance similar to dedicated cardiac phased array on MRI-only platform.
- b) Objective 2: incorporate into this array a design features which would dramatically reduce PET signal attenuation compared to dedicated cardiac RF arrays on both MRI-only and PET/MRI platforms.
- c) Objective 3: develop a technology that will allow accurate determination of the 511keV attenuation coefficients of hardware that is used for accurate quantitative of PET signal that can be achieved without the need of x-ray CT.

This was achieved through two novel inventions:

- a) Novel invention 1: the software and hardware developed to complete the characterization of the prospectively-designed, novel 32-channels phased array cardiac dedicated RF phased array and its implementation address objectives 1 and 2.

- b) Novel invention 2: redesign, manufacturing and implementation of a method using a static radioactive line source to generate an accurate attenuation correction map of rigid hardware using the hybrid PET/MRI system itself without the need for CT scanners.

While achieving the first objective, the issue of misregistration of  $\mu$ -map of the phased array flexible parts is eliminated. This is determined by the negligible photons attenuation of true counts produced by the flexible part of the novel array. Nevertheless, the need to address accurate attenuation correction  $\mu$ -map for rigid hardware is also recognised. Hence, the new approach, based on transmission scan of a static radioactive source, was developed and evaluated for the patient table and the rigid, and attenuating, part of the RF array. The novel TX-based approach, using the PET/MRI system, has two advantages; any site that has the hybrid PET/MRI system can create the desired hardware maps, and the generated maps are free of beam hardening artifact typically introduced by the CT scanning of the hardware.

## 5.2 Conclusions

### 5.2.1 Chapter 2

The MRI performance of the novel prospectively-designed PET/MRI 32-channel array qualifies it to be a viable alternative to the conventional arrays for cardiovascular hybrid PET/MRI. The SNR at different acceleration factors ( $R > 2$ ) were better on average by 30% than the receivers' array currently used in cardiac PET/MRI.

### 5.2.2 Chapter 3

Results of this novel 32-channel cardiac array PET performance evaluation, together with its reported MRI performance assessment in chapter 2, suggest that the novel array is a strong alternative to the standard arrays currently used for cardiovascular hybrid PET/MRI imaging. It enables accurate PET quantification and high-temporal and spatial resolution for MR imaging.

### 5.2.3 Chapter 4

A new approach based on the transmission scan of a static radioactive source was developed and evaluated for the patient table and the rigid part of the array. The LAC of the acrylic cylinder measurements using the TX-based technique was in agreement with those in the literature confirming the validity of the technique. The over-estimation of photon counts caused by the CT-based model used for the patient table, was improved by the TX-based technique. Therefore, TX-based AC of hardware using the PET/MRI system itself is possible, and can produce more accurate images when compared to the CT-based hardware AC in cardiac PET images.

## 5.3 Answering the research question

Several findings revealed during this work show promise in achieving accurate quantification of PET while performing high temporal and spatial resolutions on MRI.

The goal of the redesign of the high-density RF phased arrays to suit PET environment has been achieved. Although the prospectively-designed novel array was developed and tested as a prototype, with no further improvements or iterations, the array performed

exceptionally well. Therefore, developing high-density 32 channels RF array of prospectively-designed for Cardiovascular PET/MRI is possible, which answers the first research question listed at the end of the introduction of chapter 1.

While the flexible 6-channel vendor array is capable of producing acceleration images at R=2 in the left-right encoding with less degradation to SNR, the novel array has still achieved higher SNR than the vendor array at the same acceleration factor. At higher acceleration factors, 3 and 4 specifically and at spatial resolution of 1x1x3 mm, the novel array produced reasonable SNR for diagnostics, while the vendor arrays have noticeable degradation of SNR and deemed unfit for diagnostics.

The above-mentioned spatial resolution, and at R=4 with no averaging, was achieved using a TrueFisp sequence and the novel array within an acquisition time of 14 sec. This, together with reasonable SNR at R=4, indicates the readiness of the novel array to provide high spatial and temporal resolutions, which answers the second research question in chapter 1.

A few patients and volunteers were imaged with the array and with the same time and work flow as the vendors array. A general trend of satisfaction is reported, which addresses the third research question posed earlier in chapter 1.

Even with tripling the number of elements in the novel RF phased array, the attenuated photons were in the range of -0.1% to 2%, much less than those produced by any of the vendors arrays with lower number of channels. In fact, the anterior part of the novel 32 channel RF phased array produced an error less than the errors that would have been produced having registered and applied its attenuation correction  $\mu$ -map, and yet, no extra time and computation were needed. The anterior part is therefore recommended to be used

with no associated hardware attenuation correction map for AC image reconstruction. These results provide an answer to research questions four, five and partially six.

Although the photon attenuation due to the posterior part of the novel array was in the acceptable range of errors ( $< 3\%$ ), further attempts aiming to eliminate the beam hardening effect that may affect the LAC estimation, encouraged development of a novel approach (the TX-based  $\mu$ -map). Besides developing TX-based hardware  $\mu$ -map for the posterior array, a TX-based hardware  $\mu$ -map for the patient table was also developed. The quantification of reconstructed cardiac images using both CT-based  $\mu$ -map and TX-based  $\mu$ -map has shown approximate 4% difference. The elimination of beam hardening effects in the TX-based map were achieved, and this theoretically improves the accuracy of the LAC, hence improving accuracy of the PET quantification. With these findings and results, both research questions seven and eight are answered.

## 5.4 Impact of the work of the thesis

### 5.4.1 On cardiovascular imaging with PET/MRI

The availability of a 32-channel phased array prospectively-designed for PET/MRI cardiovascular imaging, capable of acquiring an image fast, is a must. Several cardiovascular studies have shown the need for such tool to assist in both; reducing the scan time (especially for cardiac patient who can not hold their breath for more than 10 seconds and when free-breathing sequences are not available); and to harness the PET sensitivity by accurately quantifying tracer activities. Future broader availability of such tools will facilitate the development of shorter and more quantitatively accurate



cardiovascular imaging protocols. Additionally, the novel array provides improved spatial and temporal resolution over the 12ch-array, which could be employed in 3D acquisitions, such as, 3D cine imaging where cardiac and respiratory motions can be resolved in 3D.

#### 5.4.2 On hybrid PET/MRI imaging modalities

The two novel approaches presented here were motivated by the need for elegant solutions without unnecessary complexities. It is the author's hope that similar paths will be followed and explored in research and development. In specific terms, the expected impact is that the redesign approach used in the development of the cardiac RF phased arrays presented in this thesis will be used to improve other simultaneous hybrid PET/MRI hardware components.

If brain, breast, thorax and other RF arrays are redesigned or developed with their attenuation correction  $\mu$ -map generated with non-CT-based methods, the accuracy of PET quantification will improve, and hence confidence in the quantification-based diagnostic of cardiovascular diseases (and others) by PET/MRI, is assured.

The novel TX-based AC method presented in this work simplifies the process of generating LAC compared to what is normally performed using a rotating rod, which requires long acquisition times. Furthermore, the method addresses once and for all the beam hardening and bilinear transformations associated with the CT-based AC method for hardware used with PET/MRI modality, hence AC for the tissue and others can be focused upon.

### 5.5 Future Work

The novel array results have shown the feasibility of such devices to exist for cardiovascular and brain applications, however, for other parts of the body (i.e. prostate,

thorax liver etc.) similar RF arrays are yet to be developed. Although the novel array was developed for the Siemens Biograph mMR- PET/MRI scanner, the concept is transferable to other vendor of PET/MRI scanners.

The TX-based AC technique should be applied to other hardware used with the PET/MRI scanners, supported with independent study of their impact on PET quantification, and statistical findings should be reported.

Complete patient table TX-based AC  $\mu$ -map still needs to be developed, which requires different techniques to include the full length of the table in one AC map.

Although hardware attenuation plays a role in inaccurate quantification of PET on a PET/MRI system, motion induced inaccurate quantification is also important. Heart and respiratory motion still require more elegant and fast solutions suitable for clinical settings, without the need for offline algorithms for reconstruction and correction.

## Appendices

### Appendix 1: Research ethic approval letter for human studies carried in chapter 2.



**Date:** 21 November 2019

**To:** Dr. Udunna Anazodo

**Project ID:** 113985

**Study Title:** A Comparison of PET/CT and PET/MR Imaging in Oncology and Neurology: Approaches for improving PET/MR workflow.

**Application Type:** HSREB Initial Application

**Review Type:** Delegated

**Full Board Reporting Date:** December 3, 2019

**Date Approval Issued:** 21/Nov/2019

**REB Approval Expiry Date:** 21/Nov/2020

---

Dear Dr. Udunna Anazodo

The Western University Health Science Research Ethics Board (HSREB) has reviewed and approved the above mentioned study as described in the WREM application form, as of the HSREB Initial Approval Date noted above. This research study is to be conducted by the investigator noted above. All other required institutional approvals must also be obtained prior to the conduct of the study.

**Documents Approved:**

Document Name	Document Type	Document Date	Document Version
Compare_2019_LOI_11-18-19_Clean	Written Consent/Assent	18/Nov/2019	2.0
Compare_2019_Study_Protocol	Protocol	20/Apr/2019	1.0
MRI-Screening_Form	Other Data Collection Instruments	10/Apr/2019	
PETMR_study_Sheet	Other Data Collection Instruments	10/Apr/2019	1
Telephone_Script	Telephone Script	20/Apr/2019	1.0

No deviations from, or changes to, the protocol or WREM application should be initiated without prior written approval of an appropriate amendment from Western HSREB, except when necessary to eliminate immediate hazard(s) to study participants or when the change(s) involves only administrative or logistical aspects of the trial.

REB members involved in the research project do not participate in the review, discussion or decision.

The Western University HSREB operates in compliance with, and is constituted in accordance with, the requirements of the TriCouncil Policy Statement: Ethical Conduct for Research Involving Humans (TCPS 2); the International Conference on Harmonisation Good Clinical Practice Consolidated Guideline (ICH GCP); Part C, Division 5 of the Food and Drug Regulations; Part 4 of the Natural Health Products Regulations; Part 3 of the Medical Devices Regulations and the provisions of the Ontario Personal Health Information Protection Act (PHIPA 2004) and its applicable regulations. The HSREB is registered with the U.S. Department of Health & Human Services under the IRB registration number IRB 00000940.

Please do not hesitate to contact us if you have any questions.

Sincerely,

Karen Gopaul, Ethics Officer on behalf of Dr. Joseph Gilbert, HSREB Chair

*Note: This correspondence includes an electronic signature (validation and approval via an online system that is compliant with all regulations).*

## Appendix 2: Research ethic approval letter for human studies carried in chapter 4.



**Date:** 28 July 2020

**To:** Terry Thompson

**Project ID:** 6319

**Study Title:** Improving Magnetic Resonance Imaging Hardware and Software at 1.5 and 3 Tesla

**Application Type:** Continuing Ethics Review (CER) Form

**Review Type:** Delegated

**REB Meeting Date:** 18Aug2020

**Date Approval Issued:** 28/Jul/2020 16:35

**REB Approval Expiry Date:** 28/Jul/2021

---

Dear Terry Thompson,

The Western University Research Ethics Board has reviewed the application. This study, including all currently approved documents, has been re-approved until the expiry date noted above.

REB members involved in the research project do not participate in the review, discussion or decision.

Western University REB operates in compliance with, and is constituted in accordance with, the requirements of the TriCouncil Policy Statement: Ethical Conduct for Research Involving Humans (TCPS 2); the International Conference on Harmonisation Good Clinical Practice Consolidated Guideline (ICH GCP); Part C, Division 5 of the Food and Drug Regulations; Part 4 of the Natural Health Products Regulations; Part 3 of the Medical Devices Regulations and the provisions of the Ontario Personal Health Information Protection Act (PHIPA 2004) and its applicable regulations. The REB is registered with the U.S. Department of Health & Human Services under the IRB registration number IRB 00000940.

Please do not hesitate to contact us if you have any questions.

Sincerely,

The Office of Human Research Ethics

*Note: This correspondence includes an electronic signature (validation and approval via an online system that is compliant with all regulations).*

# Curriculum Vitae

## Adam Farag, MSc.

### Degrees

2005/9 - 2006/12      Master's Thesis, MSc, Physics, University of Western Ontario

Supervisors:          Robert P. Lowe

1986/9 - 1990/5      Bachelor's Equivalent, Bachelor of Science and Education, Physics  
and Chemistry, Egypt.

### Credentials Certifications

2019/10                IDEA Sequence Programming-VE11 MR8SDE, Siemens  
Healthineers, NC, USA

2006/11 - 2006/11    Certificate in Project Management, Queen's University

2006/6 - 2006/6      Certificate in Business Development, Queen's University

### Areas of Research

Research and development of hardware, techniques and methodologies for medical imaging, X-nuclei imaging, hyperpolarized lung imaging, prostate cancer diagnosis and grading, cardiac imaging.

### Employment

2018/9                PhD candidate Medical Biophysics  
University of Western Ontario

2014/4 - 2017/7      Director of Research

2008/5 - 2013/10	Research Associate/ MRI specialist University of Western Ontario
2005/1 - 2007/9	Research-Assistant - VHF Wind Profiler Radar Network University of Western Ontario
2005/9 - 2006/12	Teaching Assistant /Graduate Student Physics and Astronomy, University of Western Ontario
2004/2 - 2004/7	Science Teacher Assistant Putney High, UK
1999/1 - 2003/12	Technical Adviser, Science Education (Seconded by the UN) Ministry of Education, Namibia
1998/1 - 1998/12	Branch Manager Felopater Ltd. Textile Mfg, South Africa
1990/6 - 1997/9	Quality Assurance Manager Stainless Steel cutlery division, EIG Manufacturing, Egypt

### **Teaching**

*Instructor-* Mathematics, Physics, Fluid Dynamics, Statistics,  
Project management.

*Fanshawe College*

*TA - Physics, 026, 028, 029*

*University of Western Ontario*

*TA - MATLAB computing 326G*

*University of Western Ontario*

### **Journal Review Activities**

2013/9 - 2013/9 Peer Reviewer, Journal of Magnetic Resonance Imaging.

2020/7 Peer Reviewer, Journal of Magnetic Resonance Imaging.

### **Presentations and Invited speaking**

- 2017                      Evaluating Phased Arrays from Experimental data. Sim4Life Workshop, Hawaii, United States
- 2015                      PET Compatible RF Coils. Siemens Erlangen, Erlangen, Germany
- 2013                      Hyperpolarized Pulmonary MRI at Robarts Research Institute. Coils for Research Discussions, GE Healthcare Systems, Aurora, United States.

### **Media appearances and Interviews**

- 2015/12/08              World first in imaging technology developed at Lawson, London Free Press
- 2015/11/19              Progress report, World Discovery Annual Report

### **Book Reviews**

- 2018/2019              Fundamentals of Mathematics, Ed. 4. VrettaInc. (2019), Canada

### **Thesis/Dissertation**

- 2020                      Improving Hybrid PET/MRI cardiovascular imaging with improved hardware design and attenuation correction coefficient.
- 2016                      Search for Seismically-Generated Infrasonic waves at the Hydroxyl Airglow using scanning radiometer. University of Western Ontario.

## Journal Articles

1. Adam Farag, R. Terry Thompson, Jonathan D. Thiessen, Heather Biernaski, Frank S. Prato and Jean Théberge. (2020). **Evaluation of 511 keV photon attenuation by a novel 32-channel phased array prospectively designed for cardiovascular hybrid PET/MRI imaging.** European Journal of Hybrid Imaging, <https://doi.org/10.1186/s41824-020-00076-w>. (2020- 4:7)
2. Adam Farag, R. Terry Thompson, Jonathan D. Thiessen, John Butler, Frank S. Prato and Jean Théberge. (2019). **Assessment of a novel 32-channel phased array for cardiovascular hybrid PET/MRI imaging: MRI performance.** European Journal of Hybrid Imaging. 3:13 <http://dx.doi.org/doi.org/10.1186/s41824-019-0061-7>
3. Nolan Broeke, Justin Peterson, Joseph Lee, Peter Martin, Adam Farag, Jose Gomez-Lemus, Madeleine Moussa, Mena Gaed, Joseph Chin, Stephen Pautler, Aaron Ward, Glenn Bauman, Robert Barth, and Timothy Scholl. (2018). **Characterization of Clinical Human Prostate Cancer Lesions Using 3.0- T Sodium MRI Registered to Gleason-Graded Whole-Mount Histopathology.** Journal of Magnetic Resonance Imaging DOI: 10.1002/jmri.26336.
4. Farag, A., Peterson, J. C., Szekeres, T., Bauman, G., Chin, J., Romagnoli, C., ... & Scholl, T. J. (2014). **Unshielded asymmetric transmit-only and endorectal receive-only radio frequency coil for  $^{23}\text{Na}$  MRI of the prostate at 3 Tesla.** JMRI-14-0668.
5. Ouriadov, A., Farag, A., Kirby, M., McCormack, D. G., Parraga, G., & Santyr, G. E. (2014). **Pulmonary hyperpolarized  $^{129}\text{Xe}$  morphometry for mapping xenon gas concentrations and alveolar oxygen partial pressure: Proof-of-concept demonstration in healthy and COPD subjects.** Magnetic Resonance Medicine-14-15322.
6. Shukla, Y., Wheatley, A., Kirby, M., Svenningsen, S., Farag, A., Santyr, G., ...& Parraga, G. (2013). **Hyperpolarized  $^{129}\text{Xe}$  magnetic resonance imaging: tolerability in healthy**



**volunteers and subjects with pulmonary disease.** Academic radiology, 19(8), 941-951, 2012.,

7. Ouriadov, A., Farag, A., Kirby, M., McCormack, D. G., Parraga, G., & Santyr, G. E. (2013). (2013). **Lung morphometry using hyperpolarized  $^{129}\text{Xe}$  apparent diffusion coefficient anisotropy in chronic obstructive pulmonary disease.** Magnetic Resonance in Medicine, 70(6), 1699-1706, DOI 10.1002/mrm.24595.

8. Kirby, M., Svenningsen, S., Owringi, A., Wheatley, A., Farag, A., Ouriadov, A., ... & Parraga, G. (2012). **Hyperpolarized  $^3\text{He}$  and  $^{129}\text{Xe}$  MR imaging in healthy volunteers and patients with chronic obstructive pulmonary disease.** Radiology, 265(2), 600-610, 2012.,

#### **Conference Publications**

1. P. Yazdanbakhsh and A. Farag. (2019). **SAR Evaluation for an 8-Channel Transmit/Receive Head Coil Array at 7T for a Five-Year-Old Child.** Preceding the ISMRM Workshop on Ultrahigh Field Magnetic Resonance, Dubrovnik, Croatia.

2. P. Yazdanbakhsh, T. Wade, L. Friesen-Waldner, A. Farag, and C.McKenzie. (2019).  **$^{13}\text{C}/^1\text{H}$  Dual-Resonance RF Coil for Guinea Peg imaging at 3T MRI – A Novel Approach.** Preceding the 7<sup>th</sup> International Congress for Magnetic Resonance Imaging (ICMRI), Seoul, Republic of Korea.

3. N. Broek, J. Peterson, A. Farag, T. Scholl. (2018). **Characterization of Human Prostate Cancer Using Tissue Sodium Concentration Measured from Sodium MRI.** International Society for Magnetic Resonance in Medicine (ISMRM), Paris.

4. Matthew S. Fox, Adam Farag, Alireza Akbari, Timothy J. Scholl, Terry Thompson, Jonathan D Thiessen. (2018). **Simultaneous X-Nuclei MRI and PET using  $^{23}\text{Na}$  and  $^{18}\text{F}$ -FDG.** The World Molecular Imaging Congress (WMIC).

5. Anazodo, U., Farag, A., Théberge, J., Teuho, J., Thompson, R.T., Teras, M., Taylor, R., Butler, J., Finger, E.C., Prato, F.S., & J.D. Thiessen. (2016). **Assessment of PET performance of a 32 Channel MR Brain Array Head Coil Compatible with PET for Integrated PET-MRI.** PSMR Cologne, Germany, May 23-25.
6. J. Peterson, A. Farag, T. Szekeres, E. Gibson, A. Ward, J. Chin, S. Pautler, G. Bauman, C. Romagnoli, R. Bartha, and T. Scholl. (2015). **In Vivo Sodium Imaging of Human Prostate Cancer.** International Society for Magnetic Resonance in Medicine (ISMRM), Toronto.
7. A. Farag, and J. Theberge. (2015). **Optimization of a 32-channel Resonator for Simultaneous PET/MRI of the Head at 3.0 Tesla: Material Selection and Performance Testing.** International Society for Magnetic Resonance in Medicine (ISMRM), Toronto.
8. A. Farag, J. Peterson, T. Wade, T. Szekeres, A. Ouriadove, E. Gibson, A. Ward, J. Chin, S. Pautler, G. Bauman, C. Romagnoli, R. Bartha, and T. Scholl. (2014). **Combined Transmit-Only Asymmetric Birdcage and Receive-Only Endorectal Surface RF Coils.** International Society for Magnetic Resonance in Medicine (ISMRM), Milan, 5236.
9. M. Kirby, A. Wheatley, A. Farag, A. Ouriadov, G.E. Santyr D.G. McCormack and G. Parraga. (2012). **Hyperpolarized Helium-3 and Xenon-129 Magnetic Resonance Functional Imaging in Healthy Volunteers and Subjects with Chronic Obstructive Pulmonary Disease.** International Conference of the American Thoracic Society Meeting, San Francisco, California, USA (05/12).
10. M. Kirby, A. Wheatley, A. Farag, A. Ouriadov, G.E. Santyr D.G. McCormack and G. Parraga. (2012). **Hyperpolarized Helium-3 and Xenon-129 Magnetic Resonance Imaging of Elderly Never-smokers and Ex-smokers with Chronic Obstructive Pulmonary Disease.** International Society for Magnetic Resonance in Medicine, (ISMRM) Australia, 678, 2012.

11. S. Svenningsen, A. Wheatley, M. Kirby, A. Farag, A. Ouriadov, G. Santyr, D. G. McCormack and G. Parraga. (2012). **Anatomical Distribution of Hyperpolarized  $^3\text{He}$  and  $^{129}\text{Xe}$  MRI Apparent Diffusion Coefficients in Asthma.** International Society for Magnetic Resonance in Medicine (ISMRM), 2012.
12. D.G. McCormack, S. Halko, S. McKay, A. Wheatley, A. Farag, G.E. Santyr and G. Parraga. (2012). **Hyperpolarized  $^{129}\text{Xe}$  MRI Feasibility, Subject Safety and Tolerability: At the doorstep of Clinical Translation.** International Conference of the American Thoracic Society Meeting, San Francisco, California, USA (05/12).
13. Ouriadov, A. Farag, M. Kirby, D. McCormack, G. Parraga and G. Santyr. (2012). **Hyperpolarized  $^{129}\text{Xe}$  Apparent Diffusion Coefficient Anisotropy in Chronic Obstructive Pulmonary Disease.** International Society for Magnetic Resonance in Medicine (ISMRM), Australia, 5545, 2012.
14. A. Farag, J. Wang, A. Ouriadov, G. Parraga, and G. Santyr. (2012). **Unshielded and Asymmetric RF Transmit Coil for Hyperpolarized  $^{129}\text{Xe}$  Human Lung Imaging at 3.0T.** International Society for Magnetic Resonance in Medicine (ISMRM), Australia, 1361, 2012.
15. A. Farag, W. Hocking. (2010). **Correlation Between Vertical and Horizontal Winds in The Troposphere As Seen By The O-Qnet.** Proceeding of twelfth International Workshop on Technical and Scientific Aspects of MST Radar, P139-142; CAP 2010.
16. A. Farag, S. Argall, and W. Hocking. (2009). **Validation of ADM-Aeolus Satellite using wind profiler measurements.** Proceeding of twelfth International Workshop on Technical and Scientific Aspects of MST Radar, 2009.
17. A. Farag, R. Lowe and L. Mansinha. (2006). **Detection of Seismically-Generated Infrasonic Signature in the Hydroxyl Airglow.** Canadian Association of Physicists Congress, St. Catherine, Ontario, Canada, 2006.

18. A. Farag, R. Lowe and L. Mansinha. (2005). **Search on Atmospheric Infrasound waves using The University of Western Ontario scanning radiometer**. 32<sup>nd</sup> Annual European Meeting on Atmospheric Studies by Optical Methods, London, Canada, 2005.